EUROPEAN ORGANISATION FOR NUCLEAR RESEARCH (CERN)

Submitted to: JHEP

CERN-EP-2022-166
26th August 2022

Evidence for the charge asymmetry in $pp \to t\bar{t}$ production at $\sqrt{s} = 13$ TeV with the ATLAS detector

The ATLAS Collaboration

Inclusive and differential measurements of the top–antitop ($t\bar{t}$) charge asymmetry $A_{\mathrm{C}}^{t\bar{t}}$ and the leptonic asymmetry $A_{\mathrm{C}}^{\ell\bar{\ell}}$ are presented in proton–proton collisions at $\sqrt{s} = 13$ TeV recorded by the ATLAS experiment at the CERN Large Hadron Collider. The measurement uses the complete Run 2 dataset, corresponding to an integrated luminosity of 139 fb^{-1}, combines data in the single-lepton and dilepton channels, and employs reconstruction techniques adapted to both the resolved and boosted topologies. A Bayesian unfolding procedure is performed to correct for detector resolution and acceptance effects. The combined inclusive $t\bar{t}$ charge asymmetry is measured to be $A_{\mathrm{C}}^{t\bar{t}} = 0.0068 \pm 0.0015$, which differs from zero by 4.7 standard deviations. Differential measurements are performed as a function of the invariant mass, transverse momentum and longitudinal boost of the $t\bar{t}$ system. Both the inclusive and differential measurements are found to be compatible with the Standard Model predictions, at next-to-next-to-leading order in quantum chromodynamics perturbation theory with next-to-leading-order electroweak corrections. The measurements are interpreted in the framework of the Standard Model effective field theory, placing competitive bounds on several Wilson coefficients.

Contents

1 Introduction

The large mass of the top quark, which is close to the electroweak symmetry breaking scale, indicates that this particle could play a special role in beyond the Standard Model (BSM) theories. Due to the large top-pair production ($t\bar{t}$) cross-section for $\sqrt{s}$ = 13 TeV proton–proton (pp) collisions [1, 2], the Large Hadron Collider (LHC) experiments collected an unprecedented number of events in which a top-pair is produced. The top quark has a very short lifetime ($\tau_t \approx 0.5 \times 10^{-24}$ s) and decays before hadronisation ($\tau^{\text{had}} \sim 10^{-23}$ s) [3]; therefore, several of its properties may be measured precisely from studies of the top quark's decay products. These measurements test predictions of quantum chromodynamics (QCD), which provides the largest contribution to $t\bar{t}$ production, and probe potential contributions from couplings between the top quark and BSM particles [4–6].

Production of top-quark pairs is symmetric at leading order (LO) under charge conjugation, and production via gluon fusion (the dominant mechanism at the LHC) is symmetric to all orders. An asymmetry between the t and $\bar{t}$ originates from interference of the higher-order amplitudes in the $q\bar{q}$ and qg initial states, with the $q\bar{q}$ annihilation contribution dominating [7, 8]. The $qg \to t\bar{t}g$ production process is also asymmetric, but its cross-section is much smaller than that of $q\bar{q}$. As a consequence of these asymmetries, the top quark (top antiquark) is preferentially produced in the direction of the incoming quark (antiquark).

At a $p\bar{p}$ collider the preferential direction of the incoming quark (antiquark) almost always coincides with that of the proton (antiproton). The forward–backward asymmetry A_{FB} is sizeable, $O(10\%)$, and can be measured directly [9–12]. The CDF and D0 collaborations initially reported measurements of A_{FB} that were in some tension with the next-to-leading-order (NLO) Standard Model (SM) prediction. However, the Tevatron legacy results are in good agreement with higher-order calculations [11–16].

The LHC is a pp collider. Since the colliding beams are symmetric, it is not possible to measure A_{FB} as there is no preferential direction for either the top quark or the top antiquark. However, due to the difference in the proton parton distribution functions, on average the valence quarks carry a larger fraction of the proton momentum than the sea antiquarks. This results in more forward-rapidity top quarks and more central-rapidity top antiquarks. A central–forward charge asymmetry for $t\bar{t}$ production, referred to as the charge asymmetry ($A_{\text{C}}^{t\bar{t}}$) [9, 17, 18] is defined as:

$$A_{\text{C}}^{t\bar{t}} = \frac{N(\Delta|y_{t\bar{t}}| > 0) - N(\Delta|y_{t\bar{t}}| < 0)}{N(\Delta|y_{t\bar{t}}| > 0) + N(\Delta|y_{t\bar{t}}| < 0)}, \tag{1}$$

where $\Delta|y_{t\bar{t}}| = |y_t| - |y_{\bar{t}}|$ is the difference between the absolute value of the top-quark rapidity $|y_t|$ and the absolute value of the top-antiquark rapidity $|y_{\bar{t}}|$. At the LHC, since the top-pair production contributions from $q\bar{q}$ and qg initial states are small, the dominant charge symmetric $gg \to t\bar{t}$ process dilutes the measurable asymmetry and the inclusive charge asymmetry is a subtle $O(1\%)$ effect.

A SM calculation at next-to-next-to-leading-order (NNLO) accuracy in the strong coupling and with NLO electroweak (EW) corrections predicts the inclusive charge asymmetry defined in Eq. (1) to be $0.0064^{+0.0005}_{-0.0006}$ [19], where the uncertainty includes renormalisation and factorisation scale variations and PDF uncertainties. The 'unexpanded' result of Ref. [19] is used, in which both the numerator and denominator are evaluated through the corresponding order in perturbation theory and then the ratio is taken. At the NLO, the contribution from EW corrections is about 13% for the inclusive asymmetry and almost 20% when the invariant mass of the $t\bar{t}$ system is above 1 TeV [20] in the differential case.

In events with two final-state leptons, an additional leptonic charge asymmetry is defined using the pseudorapidity of the charged leptons:

$$A_{\mathrm{C}}^{\ell\bar{\ell}} = \frac{N(\Delta|\eta_{\ell\bar{\ell}}| > 0) - N(\Delta|\eta_{\ell\bar{\ell}}| < 0)}{N(\Delta|\eta_{\ell\bar{\ell}}| > 0) + N(\Delta|\eta_{\ell\bar{\ell}}| < 0)}, \tag{2}$$

with $\Delta|\eta_{\ell\bar{\ell}}| = |\eta_{\bar{\ell}}| - |\eta_{\ell}|$, and where $N(\Delta|\eta_{\ell\bar{\ell}}| > 0)$ and $N(\Delta|\eta_{\ell\bar{\ell}}| < 0)$ represent the number of events with positive and negative $\Delta|\eta_{\ell\bar{\ell}}|$, respectively. The leptonic asymmetry is slightly diluted relative to the underlying top-quark asymmetry, but has the advantage that reconstruction of the top-quark pair is not required; only the directions and charges of the leptons are needed.

A SM calculation at NLO in QCD, including NLO EW corrections, predicts the inclusive $A_{\mathrm{C}}^{\ell\bar{\ell}}$ asymmetry defined in Eq. (2) to be $0.0040^{+0.0002}_{-0.0001}$ [20]. The uncertainty includes renormalisation and factorisation scale variations and PDF uncertainties.

Several BSM processes, such as anomalous vector or axial-vector couplings (e.g. axigluons), heavy Z' bosons, or processes which interfere with the SM, can alter $A_{\mathrm{C}}^{t\bar{t}}$ [4–6, 17, 21–28]. Some BSM models also predict charge asymmetries which vary as a function of the invariant mass $m_{t\bar{t}}$, the transverse momentum $p_{\mathrm{T},t\bar{t}}$ and the longitudinal boost of the $t\bar{t}$ system along the z-axis, $\beta_{\mathrm{z},t\bar{t}}$.[1] In particular, BSM effects are expected to be enhanced in specific kinematic regions, for example, when $\beta_{\mathrm{z},t\bar{t}}$ or $m_{t\bar{t}}$ is large [29].

The measurements performed so far by both the ATLAS and CMS collaborations at $\sqrt{s} = 7$, 8 and 13 TeV, in different decay channels and topologies, have demonstrated good agreement with SM predictions [30–40]. However, even for the combined ATLAS and CMS inclusive and differential measurements in the lepton+jet channel at $\sqrt{s} = 7$ and $\sqrt{s} = 8$ TeV [41], uncertainties in the inclusive regions and in kinematic regions such as those with high $m_{t\bar{t}}$ are statistically dominated and do not have sufficient sensitivity to exclude many BSM signals, nor to claim evidence for charge asymmetry at the LHC.

This paper reports the measurement of $A_{\mathrm{C}}^{t\bar{t}}$ and $A_{\mathrm{C}}^{\ell\bar{\ell}}$ with the full Run 2 data at $\sqrt{s} = 13$ TeV collected in 2015–2018 by the ATLAS experiment at the LHC. The $A_{\mathrm{C}}^{t\bar{t}}$ measurement is performed in $t\bar{t}$ events with a single isolated lepton in the final state (single-lepton), in both the resolved and boosted topologies of the top-quark decays, and in $t\bar{t}$ events with two isolated leptons in the final state (dilepton) in the resolved topology only. The $A_{\mathrm{C}}^{t\bar{t}}$ measurements in all topologies are combined inclusively, as well as differentially as a function of $m_{t\bar{t}}$, $\beta_{\mathrm{z},t\bar{t}}$ and $p_{\mathrm{T},t\bar{t}}$. The inclusive and differential $A_{\mathrm{C}}^{\ell\bar{\ell}}$ measurements (as a function of $m_{\ell\bar{\ell}}$, $p_{\mathrm{T},\ell\bar{\ell}}$ and $\beta_{\mathrm{z},\ell\bar{\ell}}$) are made in the dilepton final state in the resolved topology only. In the resolved topology, each of the top-quark decay products is reconstructed as an individual object, while in the boosted topology the products of hadronically decaying top (anti)quark are collimated into one object, a large-R jet. A Bayesian unfolding procedure [42] is applied to correct for acceptance and detector effects, resulting in parton-level A_{C} measurements for comparison with fixed-order theory predictions.

The combined results of the $A_{\mathrm{C}}^{t\bar{t}}$ inclusive measurement and the differential measurement versus $m_{t\bar{t}}$ are interpreted in the framework of the SM effective field theory (SMEFT) [43]. Bounds are placed on the Wilson coefficients of dimension-six operators that affect top-quark pair production at the LHC, including

[1] ATLAS uses a right-handed coordinate system with its origin at the nominal interaction point (IP) in the centre of the detector and the z-axis along the beam pipe. The x-axis points from the IP to the centre of the LHC ring, and the y-axis points upwards. Cylindrical coordinates (r, ϕ) are used in the transverse plane, ϕ being the azimuthal angle around the z-axis. The pseudorapidity is defined in terms of the polar angle θ as $\eta = -\ln\tan(\theta/2)$. Angular distance is measured in units of $\Delta R \equiv \sqrt{(\Delta\eta)^2 + (\Delta\phi)^2}$.

14 four-fermion operators and an operator that modifies the top–gluon interaction [44, 45]. The bounds are compared with the bounds obtained from the energy asymmetry measurement [46] in $t\bar{t}$+jet production.

The paper is organised as follows. The ATLAS detector is described in Section 2, while the object definitions and the signal and background modelling are detailed in Sections 3 and 4, respectively. The event selection is described in Section 5. The unfolding procedure is presented in Section 6. Section 7 discusses the systematic uncertainties. The results, including the EFT interpretation of $A_{\mathrm{C}}^{t\bar{t}}$ results, are shown in Section 8. The conclusions are given in Section 9.

2 ATLAS detector

The ATLAS detector [47] at the LHC covers nearly the entire solid angle around the collision point. It consists of an inner tracking detector surrounded by a thin superconducting solenoid, electromagnetic and hadron calorimeters, and a muon spectrometer incorporating three large superconducting air-core toroidal magnets.

The inner-detector system (ID) is immersed in a 2 T axial magnetic field and provides charged-particle tracking in the pseudorapidity range $|\eta| < 2.5$. The high-granularity silicon pixel detector covers the vertex region and typically provides four measurements per track, the first hit normally being in the insertable B-layer (IBL) installed before Run 2 [48, 49]. It is followed by the silicon microstrip tracker (SCT), which usually provides eight measurements per track. These silicon detectors are complemented by the transition radiation tracker (TRT), which enables radially extended track reconstruction up to $|\eta| = 2.0$. The TRT also provides electron identification information based on the fraction of hits (typically 30 in total) above a higher energy-deposit threshold corresponding to transition radiation.

The calorimeter system covers the pseudorapidity range $|\eta| < 4.9$. Within the region $|\eta| < 3.2$, electromagnetic calorimetry is provided by barrel and endcap high-granularity lead/liquid-argon (LAr) calorimeters, with an additional thin LAr presampler covering $|\eta| < 1.8$ to correct for energy loss in material upstream of the calorimeters. Hadron calorimetry is provided by the steel/scintillator-tile calorimeter, segmented into three barrel structures within $|\eta| < 1.7$, and two copper/LAr hadron endcap calorimeters. The solid angle coverage is completed with forward copper/LAr and tungsten/LAr calorimeter modules optimised for electromagnetic and hadronic energy measurements respectively.

The muon spectrometer (MS) comprises separate trigger and high-precision tracking chambers measuring the deflection of muons in a magnetic field generated by the superconducting air-core toroidal magnets. The field integral of the toroids ranges between 2.0 and 6.0 T m across most of the detector. A set of precision chambers covers the region $|\eta| < 2.7$ with three layers of monitored drift tubes, complemented by cathode-strip chambers in the forward region, where the background is highest. The muon trigger system covers the range $|\eta| < 2.4$ with resistive-plate chambers in the barrel, and thin-gap chambers in the endcap regions.

Interesting events are selected by the first-level trigger system implemented in custom hardware, followed by selections made by algorithms implemented in software in the high-level trigger [50]. The first-level trigger accepts events from the 40 MHz bunch crossings at a rate below 100 kHz, which the high-level trigger further reduces in order to record events to disk at about 1 kHz.

An extensive software suite [51] is used in data simulation, in the reconstruction and analysis of real and simulated data, in detector operations, and in the trigger and data acquisition systems of the experiment.

3 Object definition and reconstruction

This section defines the final-state objects at detector and parton level. The objects are used to characterise the event topologies and to define phase-space regions for the asymmetry measurements.

3.1 Detector-level objects

The primary vertex (PV) of an event is that which has the highest scalar sum of the squared transverse momenta, p_{T}^2, over all associated ID tracks [52] with $p_{\mathrm{T}} > 0.5$ GeV. At least two tracks are required.

Electron candidates are reconstructed from clusters of energy deposits in the EM calorimeter that are matched to tracks in the ID [53]. Candidates are required to have a transverse energy E_{T} greater than 28 GeV and $|\eta_{\mathrm{cluster}}| < 2.47$. If η_{cluster} is within the transition region between the barrel and the endcap of the LAr calorimeter ($1.37 < |\eta_{\mathrm{cluster}}| < 1.52$) the electron candidate is removed. A multivariate algorithm is used to select signal electrons, which have to satisfy a 'tight' likelihood-based quality criterion including shower shape and track selection requirements [54]. The transverse impact parameter d_0 of each electron candidate divided by its estimated uncertainty is required to be $|d_0|/\sigma(d_0) < 5$, while the longitudinal impact parameter z_0 must satisfy $|z_0 \sin\theta| < 0.5$ mm. The electron candidates have to pass p_{T}- and η-dependent isolation requirements based on their tracks and clusters.

Muon candidates are reconstructed from ID tracks combined with track segments or full tracks in the MS [55]. Candidates are required to fulfil the 'medium' identification quality criteria. Only muon candidates within $|\eta| < 2.5$, with $p_{\mathrm{T}} > 28$ GeV, and satisfying impact parameter criteria of $|d_0|/\sigma(d_0) < 3$ and $|z_0 \sin\theta| < 0.5$ mm, are selected. For muon candidates, the track isolation is defined similarly to electron candidates.

Jets are reconstructed from calibrated topological clusters of calorimeter-cell energies [56] by using the anti-k_t algorithm [57, 58] with a radius parameter $R = 0.4$ (small-R jets). The jet energy is corrected for pile-up effects using a jet-area method [59] and further corrected using a calibration based on both Monte Carlo (MC) simulations and data [60]. Only jets with $p_{\mathrm{T}} > 25$ GeV and $|\eta| < 2.5$ are selected. Additionally, for jets with $p_{\mathrm{T}} < 60$ GeV and $|\eta| < 2.4$, a 'jet vertex tagger' (JVT) [61] is used to discriminate between jets originating from the PV and those produced in pile-up collisions. The selected JVT working point provides an average efficiency of 92% for hard-scatter jets and a rejection factor of 99% for pile-up jets.

Small-R jets containing b-hadrons are identified ('b-tagged') using a multivariate algorithm, MV2c10 [62], which combines information about track impact parameters and secondary vertices reconstructed within the jet. In the simulated $t\bar{t}$ events, the operating point for this algorithm provides an efficiency of 77% to tag b-quark jets. The corresponding rejection factors for jets originating from a c-quark, light quark, or τ-lepton are 5, 115, and 20, respectively. To account for possible mismodelling causing differences between the predicted and observed selection efficiencies for the different quark-flavour jets and for jets originating from hadronically decaying τ-leptons, per-jet scale factors are obtained from $t\bar{t}$ events in data [62].

Large-R jets are reconstructed with the anti-k_t algorithm from the individually calibrated topological cell clusters, using a radius parameter $R = 1.0$, and then calibrated using simulation [63]. They are subsequently *trimmed* [64] to remove the effects of pile-up and underlying events. Trimming is a technique in which the original constituents of the jets are reclustered using the k_t algorithm [65] with a distance parameter R_{sub}, in order to produce a collection of sub-jets. Sub-jets with a fraction of the large-R jet p_{T} less than a calibrated threshold f_{cut} are removed. The trimming parameters used in this analysis are $R_{\mathrm{sub}} = 0.2$ and

$f_{\text{cut}} = 5\%$ based on previous studies [66]. The large-R jet moments (e.g. mass, τ_{32} [67]) are calculated using only the constituents of the selected sub-jets.

The missing transverse momentum [68], with magnitude $E_{\text{T}}^{\text{miss}}$, is calculated from a vectorial sum of all reconstructed objects. These include calibrated electrons, muons, photons, hadronically decaying τ-leptons, and reconstructed small-R jets. They are combined with soft hadronic activity measured as reconstructed charged-particle tracks associated with the PV but not with other objects.

In order to avoid double counting of the same energy clusters or tracks as different object types, an overlap removal procedure is applied. Firstly, electron candidates sharing a track with any muon candidates are removed. Secondly, if the distance between a small-R jet and an electron candidate is $\Delta R < 0.2$, the jet is removed. If multiple small-R jets are found with this requirement, only the closest small-R jet is removed. If the distance between a small-R jet and an electron candidate is $0.2 < \Delta R < 0.4$, then the electron candidate is removed. If the distance between a small-R jet and any muon candidate is $\Delta R < 0.4$, the muon candidate is removed if the small-R jet has more than two associated tracks, otherwise the small-R jet is removed. Finally, if the distance between a large-R jet and an electron candidate is $\Delta R < 1.0$, the large-R jet is removed.

3.2 Parton-level objects

Unfolding requires a definition of parton-level t and $\bar{t}$ quarks. For this measurement, a parton-based definition using generator-level information is used. The top-(anti)quark four-momentum is obtained from MC events, taking the last t ($\bar{t}$) in the decay chain, just after final-state radiation (FSR) but before it decays. The $A_{\text{C}}^{t\bar{t}}$ measurements are corrected for reconstruction and acceptance effects to parton level in the full phase-space.

In the measurement of the leptonic asymmetry, the leptons are defined as prompt particles from W-boson decays in the MC event record, where the W bosons originate from top-quark decays. The lepton momenta are taken prior to QED radiation. The unfolded $A_{\text{C}}^{\ell\bar{\ell}}$ is obtained in the reduced phase-space defined by the requirement $|\Delta|\eta_{\ell\bar{\ell}}|| < 2.5$.

4 Signal and background modelling

All signal and background processes are modelled using MC simulations, with the exception of non-prompt-lepton and fake-lepton backgrounds, which are estimated using data-driven methods (see Section 4.4). All simulated samples used EvtGen 1.6.0 [69] to model the decays of heavy hadrons, with the exception of some background samples generated with Sherpa [70]. Most of the MC samples were processed using a full simulation [71] of the detector response with the Geant4 toolkit [72]. Samples used to estimate systematic uncertainties in the modelling were obtained either by reweighting the default full-simulation samples or by using fast simulation software (ATLFAST-II [71]) to parameterise the showers in the calorimeter. To model additional pp interactions from the same or neighbouring bunch crossings, the hard-scattering events were overlaid with a set of minimum-bias interactions generated using Pythia 8 [73] and the MSTW2008lo [74] parton distribution function (PDF) set with the A3 [75] tuned parameter settings. Finally, the simulated MC events are reconstructed using the same software as the data. More details of the MC samples for the signal and for each background are provided in the following.

4.1 $t\bar{t}$ signal

All $t\bar{t}$ samples were generated with a top-quark mass of $m_{\text{top}} = 172.5\,\text{GeV}$ and are normalised to the inclusive production cross-section of $\sigma(t\bar{t}) = 832 \pm 51\,\text{pb}$. This cross-section is calculated at NNLO in QCD including the resummation of next-to-next-to-leading-logarithm (NNLL) soft-gluon terms using Top++ 2.0 [76–82]. The uncertainties in the cross-section due to the PDF and α_s are calculated using the PDF4LHC prescription [83] with the MSTW2008nnlo 68% CL [74, 84], CT10nnlo [85, 86] and NNPDF2.3 5f FFN [87] PDF sets, and are added in quadrature to the effect of the scale uncertainty.

The nominal $t\bar{t}$ events were generated with the Powheg Box v2 [88–94] generator, which provides matrix elements at NLO in the strong coupling constant α_s, with the NNPDF3.0nlo [95] PDF and the h_{damp} parameter[2] set to $1.5\,m_{\text{top}}$ [96]. The functional form of the renormalisation and factorisation scales (μ_r and μ_f) was set to the nominal scale of $\sqrt{m_{\text{top}}^2 + p_{\text{T,top}}^2}$. The events were interfaced with Pythia 8.230 [73] for the parton shower (PS) and hadronisation, using the A14 set of tuned parameters [97] and the NNPDF2.3lo [95] PDF set.

To study the $t\bar{t}$ modelling uncertainties, alternative MC samples are considered. Particular samples were simulated using a parameterised detector shower response in ATLFAST-II, and compared with a version of the nominal sample which was produced in the same way.

The impact of choosing a different PS and hadronisation model is evaluated by comparing the nominal $t\bar{t}$ signal sample with an alternative sample from the nominal matrix-element (ME) generator interfaced with Herwig 7.04 [98, 99] instead of Pythia 8.230, and using the H7UE set of tuned parameters [99, 100] and the MMHT2014lo PDF set [101].

The Protos generator [102] with the CTEQ6L1 PDF set [103] was used to generate $t\bar{t}$ samples predicting different asymmetry values due to the inclusion of a new heavy axigluon. The generated samples contain only parton-level information, which is later used to reweight the nominal $t\bar{t}$ Powheg+Pythia 8 sample.

4.2 Single top

Single-top tW associated production was modelled using the Powheg Box v2 generator, which provides MEs at NLO in α_s, using the five-flavour scheme with the NNPDF3.0nlo PDF set. The functional form of μ_r and μ_f was set to the nominal scale of $\sqrt{m_{\text{top}}^2 + p_{\text{T,top}}^2}$. The diagram removal (DR) scheme [104] was employed to treat the interference with $t\bar{t}$ production [96]. Dedicated samples using a diagram subtraction (DS) scheme [104] are considered when evaluating the uncertainty due to the treatment of the overlap with $t\bar{t}$ production.

Single-top t-channel (s-channel) production was modelled using the Powheg Box v2 generator, which provides MEs at NLO in α_s, using the four-flavour (five-flavour) scheme with the NNPDF3.0nlo PDF set. The functional form of μ_r and μ_f is not determined by the heavy top quark, but was set to $\sqrt{m_b^2 + p_{\text{T},b}^2}$ [93], following the arguments presented in Ref. [105]. For these processes, the events were interfaced with Pythia 8.230 using the A14 parameter tune and the NNPDF2.3lo PDF set.

[2] The h_{damp} parameter controls the p_T of the first additional emission beyond the LO Feynman diagram in the parton shower and therefore regulates the high-p_T emission against which the $t\bar{t}$ system recoils.

Similarly to the $t\bar{t}$ samples, the impact of choosing a different PS and hadronisation model is evaluated by comparing the nominal sample with an alternative sample from the nominal ME generator interfaced instead with Herwig 7.04, using the H7UE set of tuned parameters and the MMHT2014lo PDF set.

4.3 W and Z bosons with additional jets

QCD V+jets production ($V = W$ or Z boson) was simulated with the Sherpa 2.2.1 [70] PS MC generator. In this set-up, NLO MEs for up to two jets, and LO MEs for up to four jets, were calculated with the Comix [106] and OpenLoops [107, 108] libraries. The nominal Sherpa PS [109], based on Catani–Seymour dipoles and the cluster hadronisation model [110], was used. This employs a dedicated set of tuned parameters developed by the Sherpa authors and based on the NNPDF3.0nnlo PDF set [95]. The V+jets samples are normalised to a NNLO prediction [111].

4.3.1 Z calibration in the dilepton channel

Scaling factors are applied to the Z+jets background in the dilepton channel, to allow for the significant theoretical uncertainties in modelling the heavy-flavour contribution to this process. The modelling uncertainties mainly affect the same-flavour channels, for which the $Z \to \ell\ell$ contribution to the background is larger. A control region is created by applying a 10 GeV mass window around the Z-boson mass to the invariant mass of the opposite-sign lepton pair; this region is named 'OSZ'. The $E_{\mathrm{T}}^{\mathrm{miss}}$ requirements (see Section 5.3) are removed, in order to increase the number of Z+jets events and their purity in the control region. Using this control region, a scale factor, μ_Z, is defined as the ratio of the number of data events after the subtraction of other processes (based on MC predictions) to the predicted number of Z+jets events.

The scale factors are derived separately for the $1b$-tag-exclusive and $2b$-tag-inclusive regions because of their different heavy-flavour compositions. The validity of the derived scale factors is checked as a function of the kinematics of the $t\bar{t}$ system and as a function of the loosened $E_{\mathrm{T}}^{\mathrm{miss}}$ requirement in the OSZ control region. Each scale factor is assigned a 30% normalisation uncertainty, which fully covers the statistical and systematic errors, and all sources of kinematic or selection dependence. The measured scale factors are 1.21 ± 0.36 and 1.39 ± 0.42 for the $1b$-tag-exclusive and $2b$-tag-inclusive regions, respectively. These factors are applied to the Z+jets background events predicted by the MC simulation.

The contribution of the $Z \to \tau\tau$ process in the $e\mu$ channel is very small, and is estimated using MC simulation only. No scale factors are applied, but a 30% normalisation uncertainty is assigned for consistency with the same-flavour channels.

4.4 Non-prompt and fake leptons background

4.4.1 Single-lepton channel

Non-prompt- and fake-lepton events (fake events), can enter the selected data samples if a non-prompt or fake lepton is reconstructed. Several production mechanisms or mistakes in event reconstruction can produce such leptons. These include semileptonic decays of heavy-flavour hadrons, long-lived weakly decaying states (e.g. $\pi^{\pm}$, K mesons), π^0 mesons misreconstructed as electrons, electrons from photon conversions, or prompt photons. To estimate the total contribution of fake events a data-driven 'matrix-method' [112] is

used. Two categories of events are selected, satisfying 'loose' (identification only) and 'tight' (identification and isolation) lepton selection requirements, respectively. The real-lepton (fake-lepton) efficiency, ϵ_{real} (ϵ_{fake}), is defined as the ratio of the number of events with a real (non-prompt/fake) lepton satisfying the tight selection to the number of events with a real (non-prompt/fake) lepton satisfying the loose selection. The real-lepton efficiency is measured in data by applying a tag-and-probe method to Z decays with two leptons and jets in the final state, while the fake-lepton efficiency is measured in control regions enriched in fake/non-prompt leptons. The contribution of fake events is estimated from weighted data events passing loose lepton selection requirements, where the weight depends on the real- and fake-lepton efficiencies.

4.4.2 Dilepton channel

To allow for possible mismodelling of the non-prompt- and fake-lepton backgrounds in the dilepton channel, a scaling factor is extracted using a data-driven approach and is applied to the MC prediction. The MC contribution is evaluated from the generator's event record, using the history of the stable particles and summing over all MC samples.

A control region enriched in fake leptons is created by applying all the standard selection requirements, but requiring the two leptons to have same-sign charges; this region is denoted by 'SS'. The fake-lepton scale factor, μ_{fake}, is derived by comparing the number of simulated events in the SS region with those observed in data, after subtracting the MC-predicted number of events with two same-sign prompt leptons.

The scale factors are measured separately in $ee + e\mu$ events (where the fake electrons dominate) and in $\mu\mu$ events, and are applied to each event containing fake leptons in the corresponding opposite-sign signal region. In addition, the effect of charge misidentification is taken into consideration in the $ee + e\mu$ fake-lepton scale factors. A correction for charge misidentification is first derived by comparing events in the OSZ region with events in a same-sign version of the Z-mass window, denoted by 'SSZ', and between the MC prediction and data. Unlike the OSZ region, the SSZ region consists primarily of events (dilepton $t\bar{t}$, single top and Z+jets) for which the charge of one of the leptons has been misassigned. The Z+jets events have already been scaled by μ_Z, to reduce the effect of heavy-flavour mismodelling on the estimate of charge misidentification.

The final $ee + e\mu$ fake-lepton scale factors, accounting also for charge misidentification, are measured to be 0.96 ± 0.29 and 0.94 ± 0.28 in the $1b$-tag-exclusive and $2b$-tag-inclusive regions, respectively. A normalisation uncertainty of 30% accounts for the statistical uncertainty, charge misidentification and range of fake-lepton estimates across the $t\bar{t}$ and dilepton kinematic variables. The equivalent $\mu\mu$ fake-lepton scale factors are measured to be 2.3 ± 1.2 and 4.2 ± 2.1 in the $1b$-tag-exclusive and $2b$-tag-inclusive regions, respectively. These include a 50% normalisation uncertainty, due to the low number of events in the muonic SS region and high contamination from $t\bar{t}V$ events. Fake leptons from $\mu\mu$ events contribute less than 1% to the total number of events in the signal region.

4.5 Other backgrounds

Diboson (VV) samples were simulated with the Sherpa 2.2.1 and 2.2.2 [70] PS MC generator. Sherpa 2.2.2 was used for two- and three-lepton samples. Additional hard-parton emissions [106] were matched to a PS based on Catani–Seymour dipoles, using a dedicated set of tuned parton-shower parameters developed by the Sherpa authors, and the NNPDF3.0nnlo PDF set. Matrix element and PS matching [113] was employed for different jet multiplicities, which were then merged into an inclusive sample using an improved

CKKW matching procedure [114, 115]. The procedure was extended to NLO using the MEPS@NLO prescription [116]. These simulations are at NLO for up to one additional parton and at LO for up to three additional parton emissions using factorised on-shell decays. The virtual QCD corrections for matrix elements at NLO were provided by the OpenLoops library. The calculation was performed in the G_μ scheme, ensuring an optimal description of pure EW interactions at the EW scale.

The production of $t\bar{t}V$ and $t\bar{t}H$ events was modelled using the MadGraph5_aMC@NLO 2.3.3 [117] and Powheg Box v2 generators, respectively. The generators provide matrix elements at NLO in α_s, with the NNPDF3.0nlo PDF set. An exception is the simulation of $t\bar{t}H$ events corresponding to data collected in 2018, modelled using the MadGraph5_aMC@NLO 2.6.0 generator. For $t\bar{t}V$ and $t\bar{t}H$ production, the events were interfaced with Pythia 8.210 [73] and Pythia 8.230, respectively. Each used the A14 tune and the NNPDF2.3lo PDF set.

The rare SM processes leading to tWZ and tZ production are also considered in the dilepton channel. For both processes, the samples were simulated with the MadGraph5_aMC@NLO 2.3.3 generator at NLO with the NNPDF3.0nlo PDF set. The events were interfaced with Pythia 8.212 [73] using the A14 tune and the NNPDF2.3lo PDF set.

5 Event selection and reconstruction

5.1 Common event selection

The analysis uses data collected by the ATLAS detector between 2015 and 2018 from pp collisions at a centre-of-mass energy of $\sqrt{s} = 13$ TeV, corresponding to an integrated luminosity of 139 fb^{-1}. Only events recorded under stable beam conditions with all detector subsystems operational [118], with a primary vertex and passing a single-electron or single-muon trigger are considered. Multiple triggers are used to increase the selection efficiency. The lowest-threshold triggers utilise isolation requirements to reduce the trigger rate. These have p_T thresholds of 20 GeV for muons and 24 GeV for electrons in 2015 data, and 26 GeV for both lepton types in 2016, 2017 and 2018 data [119, 120]. They are complemented by other triggers with higher p_T thresholds and with no isolation requirements.

5.2 Event selection and reconstruction in the single-lepton topology

A common event selection is used for the resolved and boosted single-lepton topologies, requiring exactly one lepton candidate matched to the trigger lepton with a minimum p_T of 28 GeV and at least one of the small-R jets to be b-tagged. Events containing additional leptons with $p_T > 25$ GeV are rejected. To reduce the impact of fake-events background, requirements on E_T^{miss} and m_T^W are applied.[3] In the electron channel, both E_T^{miss} and m_T^W are required to be larger than 30 GeV because of the higher level of background with fake leptons (see Section 4.4), while in the muon channel a triangular requirement, $E_T^{miss} + m_T^W > 60$ GeV, is applied.

[3] $m_T^W = \sqrt{2p_T^\ell E_T^{miss}(1 - \cos\Delta\phi)}$ where $\Delta\phi$ is the angle between the lepton and $\vec{E}_T^{miss}$ in the transverse plane and p_T^ℓ is the transverse momentum of the lepton.

The selected events are divided into four regions, based on event topology (resolved, boosted) and on b-jet multiplicity ($1b$-tag-exclusive, $2b$-tag-inclusive). The events with an electron and those with a muon are summed.

5.2.1 Resolved topology

The single-lepton resolved topology requires at least four small-R jets with $p_{\mathrm{T}} > 25$ GeV. Events which also pass the boosted selection (see Section 5.2.2) are removed.

The challenge in reconstructing an event in the single-lepton resolved topology is to correctly assign individual selected jets to the corresponding partons from the decaying top quarks. For this purpose a boosted decision tree (BDT), implemented within the TMVA package [121] is designed. The BDT combines kinematic variables and b-tagging information with weight information from the Kinematic Likelihood Fitter (KLFitter) [122], into a single discriminant. Each permutation of jet-to-parton assignments is evaluated and the permutation with the highest BDT score is used for the $t\bar{t}$ kinematic reconstruction.

Since the number of possible permutations increases rapidly with the jet multiplicity, only permutations of up to five jets are considered. If more than five jets are present in an event, the two jets with the highest b-tagging scores are considered, together with the remaining three highest-p_{T} jets. The $t\bar{t}$ signal sample (see Section 4.1) is used for the BDT training, with each jet-to-parton permutation for an event labelled as either 'signal' or 'background'. Only permutations with four jets correctly assigned within $\Delta R = 0.3$ of the corresponding partons are labelled as signal; all other permutations are labelled as combinatorial background. No attempt is made to individually match the partons from the hadronically decaying W boson, as the twofold ambiguity does not affect the reconstruction. The BDT aims to discriminate the signal from the combinatorial background and is trained separately for the $1b$-tag-exclusive and $2b$-tag-inclusive regions, but inclusively in the lepton flavours (electron, muon). A large number of background permutations per event have a low likelihood calculated by the KLFitter, and these are easily distinguishable from the correct permutation. Including these permutations in the BDT training would reduce the overall performance. Therefore, the BDT is trained using only the background permutations for which the KLFitter calculates the highest likelihood.

Thirteen variables are used as input to the BDT:

- the reconstructed mass of the hadronically decaying top quark,
- the logarithm of the KLFitter likelihood,
- the reconstructed mass of the hadronically decaying W boson,
- a label depending on whether the b-jet candidate from the semileptonically decaying top quark is b-tagged or not,
- a label depending on whether the b-jet candidate from the hadronically decaying top quark is b-tagged or not,
- a label depending on whether a light-jet candidate from the W-boson decay is b-tagged or not,
- the reconstructed mass of the semileptonically decaying top quark,
- the ΔR between the b-jet candidate from the semileptonically decaying top quark and the lepton,
- the ΔR between the two light-jet candidates from the W-boson decay,

- the p_{T} of the system of the lepton and the b-jet candidate from the semileptonically decaying top quark,
- the number of jets in the event,
- the pseudorapidity of the hadronically decaying top quark,
- the ΔR between the two b-jet candidates from the $t\bar{t}$ decay.

The b-jet candidates in the variables above are those assigned by the best jet permutation, so a b-jet candidate is not necessarily b-tagged. The reconstructed mass of the semileptonically decaying top quark requires the reconstruction of the neutrino four-momentum. Experimentally, only the magnitude of the neutrino three-momentum in the transverse direction, represented by $E_{\mathrm{T}}^{\mathrm{miss}}$, and its angle in ϕ are accessible. Assuming no mass term for the neutrino, one parameter of the four-momentum must be determined. It is calculated using a W-boson mass constraint by exploiting the formula: $m_W^2 = (p^\ell + p^\nu)^2 = m_\ell^2 + 2(E^\ell E^\nu - \vec{p}^{\,\ell} \cdot \vec{p}^{\,\nu})$, where p^ℓ and p^ν are the four momenta of the charged lepton and the neutrino, respectively. This leads to a quadratic equation for the longitudinal component of the neutrino three-momentum, p_z^ν. If real solutions are found, the solution which produces a reconstructed top-quark mass closest to the expected top-quark mass is chosen. If imaginary solutions are found, the transverse components of the neutrino three-momentum are varied until a real solution for p_z^ν is found.

For the final selection, the best permutation in each event is required to have a BDT discriminant score > 0.3 in order to reject $t\bar{t}$ combinatorial backgrounds and to suppress non-$t\bar{t}$ background processes. For $t\bar{t}$ signal events where a jet-to-parton assignment is possible for all partons from the $t\bar{t}$ decay, the correct assignment is found for 75% of the events. This represents 50% of correctly assigned jets with respect to all $t\bar{t}$ signal events passing event selection. Non-$t\bar{t}$ background processes naturally populate lower regions of the BDT score, because the jet permutations are unable to satisfy the expected decay kinematics of a $t\bar{t}$ pair. Imposing a threshold on the BDT score increases the ratio of signal to non-$t\bar{t}$ background by a factor of ∼2. Table 1 shows the event yields after the event selection for the single-lepton resolved topology. Distributions of $m_{t\bar{t}}$ and $p_{\mathrm{T},t\bar{t}}$ for the single-lepton resolved 2b-inclusive region are shown in Figure 1. The total pre-marginalisation (see Section 6) uncertainty is presented.

Table 1: Event yields split by topology (resolved, boosted) and b-tag multiplicity (1b-excl., 2b-incl.) in the single-lepton channel. Statistical and systematic uncertainties are included in the presented total uncertainty.

Process:	Single-lepton resolved		Single-lepton boosted	
	1b-excl.	2b-incl.	1b-excl	2b-incl.
$t\bar{t}$	1 540 000 ± 140 000	1 870 000 ± 170 000	50 000 ± 12 000	74 000 ± 18 000
Single top	90 000 ± 11 000	51 000 ± 8 000	3 600 ± 1 100	3 000 ± 1 100
W+jets	180 000 ± 100 000	20 000 ± 9 000	8 900 ± 2 600	1 600 ± 500
$Z + VV + t\bar{t}X$	48 000 ± 25 000	14 000 ± 7 000	2 400 ± 1 200	1 400 ± 700
Fake	90 000 ± 50 000	47 000 ± 24 000	3 000 ± 1 500	2 300 ± 1 200
Total Prediction	1 940 000 ± 190 000	2 010 000 ± 180 000	68 000 ± 14 000	83 000 ± 18 000
Data	1 964 127	2 041 063	54 750	66 571

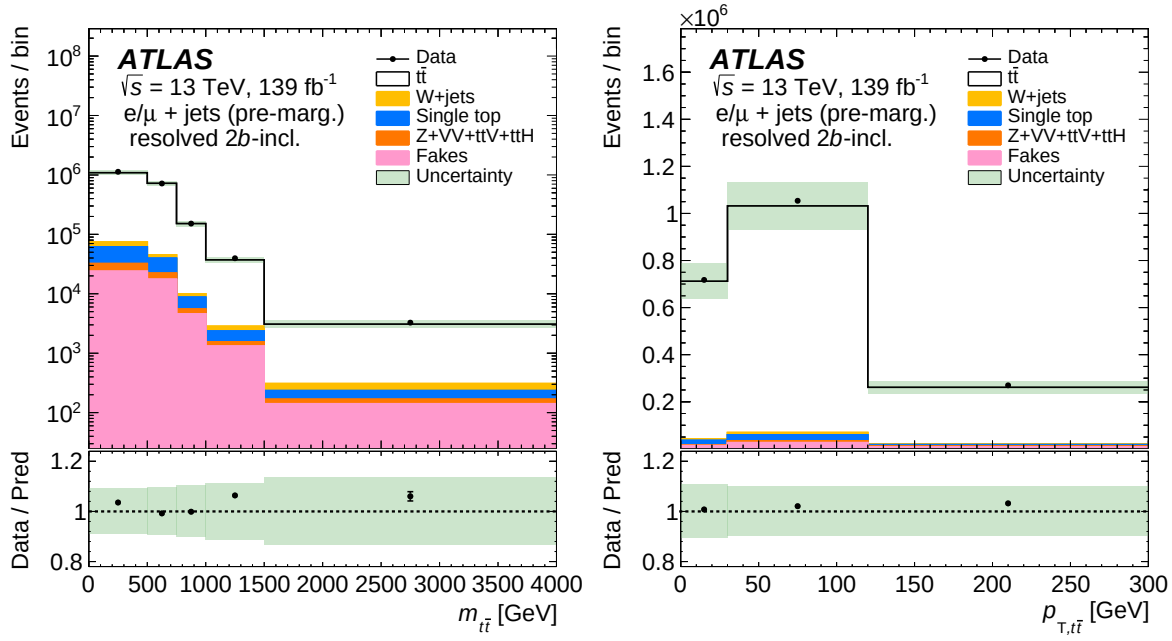

(a) (b)

Figure 1: Comparison between the data and the prediction for the reconstructed (a) $m_{t\bar{t}}$ and (b) $p_{\mathrm{T},t\bar{t}}$ in the single-lepton resolved $2b$-inclusive region. Statistical and systematic uncertainties are included in the presented total uncertainty.

5.2.2 Boosted topology

In the single-lepton boosted topology, the reconstruction aims to identify one high-p_{T} and collimated hadronic top-quark decay and at least one small-R jet with $p_{\mathrm{T}} > 25\,\mathrm{GeV}$ close to the selected lepton, with $\Delta R(\mathrm{jet}_{R=0.4}, \ell) < 1.5$. If multiple small-$R$ jets satisfy this condition, the one with highest p_{T} is considered for the subsequent semileptonically decaying top-quark reconstruction. In addition, at least one large-R top-tagged jet with $p_{\mathrm{T}} > 350\,\mathrm{GeV}$ and $|\eta| < 2$ is required as the hadronically decaying top-quark candidate. The large-R jet is evaluated by a top-tagging algorithm utilising jet mass and τ_{32} substructure [67] variables, where an operating point with an efficiency of 80% is chosen. The top tagger is optimised using the same approach as described in Ref. [123]. Since the two top quarks are expected to be back-to-back in the $t\bar{t}$ rest frame, additional requirements related to the large-R jet, the isolated lepton and the small-R jet close to the lepton are applied: $\Delta\phi(\mathrm{jet}_{R=1.0}, \ell) > 2.3$ and $\Delta R(\mathrm{jet}_{R=1.0}, \mathrm{jet}_{R=0.4}) > 1.5$. Finally, a requirement on the invariant mass of the reconstructed $t\bar{t}$ system of $m_{t\bar{t}} > 500\,\mathrm{GeV}$ is applied. This criterion is imposed to remove poorly reconstructed events passing selection in boosted regions, removing approximately 0.1% of events. Consequently, the $m_{t\bar{t}} < 500\,\mathrm{GeV}$ bin in the A_{C} vs $m_{t\bar{t}}$ measurement is removed in the boosted regions.

The four-momentum of the leading-p_{T} large-R jet satisfying the selection criteria is taken as the four-momentum estimate of the hadronically decaying top quark. The semileptonically decaying top quark's four-momentum is constructed from the isolated lepton, the selected small-R jet and the neutrino four-momentum. The neutrino four-momentum is calculated in the same way as in the single-lepton resolved topology. Table 1 shows the event yields after the event selection for the single-lepton boosted topology. The MC prediction's overestimation of the yield by about 20% in the single-lepton boosted regions is

confirmed by differential cross-sections measurements [124, 125].

5.3 Event selection and reconstruction in the dilepton topology

The dilepton topology requires at least two small-R jets with $p_{\mathrm{T}} > 25$ GeV and two opposite-charge leptons. Minimum p_{T} requirements of 28 and 25 GeV are applied for the leading and sub-leading leptons, respectively, and at least one of the leptons must be matched to the trigger lepton. At least one of the small-R jets is required to be b-tagged. For the same-flavour channel, the reconstructed invariant mass of the dilepton system is selected to be outside a Z-boson mass window ($|m_{\ell\bar{\ell}} - m_Z| > 10$ GeV) while a missing transverse momentum requirement of $E_{\mathrm{T}}^{\mathrm{miss}} > 60$ (30) GeV for the $1b$-tag-exclusive ($2b$-tag-inclusive) region is applied to further reduce the Z+jets contribution. In the $1b$-tag-exclusive region, the reconstructed invariant mass of the same-flavour dilepton system is required to be greater than 15 GeV to suppress backgrounds from low-mass resonances. The $t\bar{t}$ system is reconstructed using the Neutrino Weighting (NW) algorithm [126]. The NW event weight is required to be greater than zero, in order to remove events with poorly reconstructed kinematics; these amount to approximately 15% of signal events. The selected events are divided into four regions: by lepton flavour – events with exactly one electron and one muon ($e\mu$ channel), or two same-flavour leptons ($ee + \mu\mu$ channel) – and by b-jet multiplicity ($1b$-tag-exclusive, $2b$-tag-inclusive). Table 2 shows the event yields after the event selection for the dilepton channel.

Table 2: Event yields split by lepton flavour ($e\mu$, $ee + \mu\mu$) and b-tag multiplicity ($1b$-excl., $2b$-incl.) in the dilepton channel. Statistical and systematic uncertainties are included in the presented total uncertainty.

Process:	$e\mu$		$ee + \mu\mu$	
	$1b$-excl.	$2b$-incl.	$1b$-excl	$2b$-incl.
$t\bar{t}$	225 200 ± 3 300	262 000 ± 6 000	105 400 ± 1 900	192 000 ± 4 000
Single top (Wt)	13 800 ± 600	5 600 ± 500	6 100 ± 320	4 100 ± 400
Diboson	650 ± 40	45 ± 4	296 ± 19	55 ± 6
Z+jets	610 ± 170	77 ± 26	3 500 ± 900	3 800 ± 800
Rare SM ($t\bar{t}X$, tWZ, etc.)	690 ± 50	1 040 ± 70	389 ± 27	850 ± 60
Fake	2 500 ± 400	2 130 ± 340	1 190 ± 170	1 900 ± 260
Total Prediction	243 400 ± 3 400	271 000 ± 6 000	116 800 ± 2 100	203 000 ± 4 000
Data	244 258	273 856	116 096	202 967

6 Unfolding

The $\Delta|y_{t\bar{t}}|$ distributions, used to extract A_{C}, are smeared by acceptance and detector resolution effects. The true $\Delta|y_{t\bar{t}}|$, defined in MC simulation using the t-quark and $\bar{t}$-antiquark after final-state radiation but before decay, is estimated from data using an unfolding procedure. The fully Bayesian unfolding (FBU) [42] method is used to unfold the observed data. FBU is an application of Bayesian inference to the unfolding problem. Given the observed data $\boldsymbol{D} \in \mathcal{R}^{N_r}$ with N_r bins, the task is to determine the true distribution $\boldsymbol{T} \in \mathcal{R}^{N_t}$ with N_t bins. Assuming a response matrix $\mathcal{M} \in \mathcal{R}^{N_r} \times \mathcal{R}^{N_t}$, which models the detector response to the true distribution, and an estimate of the background distribution $\boldsymbol{B} \in \mathcal{R}^{N_r}$, the posterior probability of the true distribution follows the probability density:

$$p\left(\boldsymbol{T}|\boldsymbol{D}\right) \propto \mathcal{L}\left(\boldsymbol{D}|\boldsymbol{T}\right) \cdot \pi\left(\boldsymbol{T}\right),$$

where $p\left(\boldsymbol{T}|\boldsymbol{D}\right)$ is the posterior probability of the true distribution $\boldsymbol{T}$ under the condition of $\boldsymbol{D}$, $\mathcal{L}\left(\boldsymbol{D}|\boldsymbol{T}\right)$ is the likelihood function of $\boldsymbol{D}$ for a given $\boldsymbol{T}$, and $\pi\left(\boldsymbol{T}\right)$ is the prior probability density for the true distribution $\boldsymbol{T}$. The likelihood $\mathcal{L}\left(\boldsymbol{D}|\boldsymbol{T}\right)$ is defined as a product of Poissonian probabilities for each bin of the reconstructed spectrum:

$$\mathcal{L}\left(\boldsymbol{D}|\boldsymbol{T}\right) = \prod_{i}^{N_r} \frac{(r_i + b_i)^{d_i}}{d_i!} \mathrm{e}^{-(r_i+b_i)},$$

where r_i and b_i are the expected signal and background yields and d_i is the observed data yield in bin i. The expected signal yield r_i is given by the true distribution $\boldsymbol{T}$ and the response matrix $\mathcal{M}$ according to the following equation:

$$r_i = \sum_{j}^{N_t} m_{ij} t_j,$$

where m_{ij} are the elements of the response matrix and t_j is the true prediction in bin j.

For this measurement, in all bins a uniform prior probability density is chosen for $\pi\left(\boldsymbol{T}\right)$, such that equal probabilities are assigned to all $\boldsymbol{T}$ spectra within a wide range. The response matrix is estimated from the simulated sample of $t\bar{t}$ events, and the unfolded asymmetry A_{C} is computed from $p\left(\boldsymbol{T}|\boldsymbol{D},\mathcal{M}\right)$ as:

$$p\left(A_{\mathrm{C}}|\boldsymbol{D}\right) = \int \delta(A_{\mathrm{C}} - A_{\mathrm{C}}(\boldsymbol{T})) p\left(\boldsymbol{T}|\boldsymbol{D},\mathcal{M}\right) \mathrm{d}\boldsymbol{T}.$$

The treatment of systematic uncertainties is naturally included in the Bayesian inference approach by extending the likelihood $\mathcal{L}\left(\boldsymbol{D}|\boldsymbol{T}\right)$ to include nuisance parameters. The marginal likelihood is defined as:

$$\mathcal{L}\left(\boldsymbol{D}|\boldsymbol{T}\right) = \int \mathcal{L}\left(\boldsymbol{D}|\boldsymbol{T},\boldsymbol{\theta}\right) \cdot \mathcal{N}(\boldsymbol{\theta}) \, \mathrm{d}\boldsymbol{\theta},$$

where $\boldsymbol{\theta}$ are the nuisance parameters, and $\mathcal{N}(\boldsymbol{\theta})$ are their prior probability densities. These are assumed to be Gaussian distributions with $\mu = 0$ and $\sigma = 1$, with the exception of background normalisation distributions, which are represented by truncated Gaussian distributions to prevent unphysical negative yields. One nuisance parameter is associated with each of the uncertainty sources.

In FBU, the marginalisation approach provides a framework in which to perform the unfolding and the background estimations in multiple data regions simultaneously. Given the data distribution $\boldsymbol{D}_i$ measured in N_{reg} independent channels, the likelihood can be extended to combine the channels using a product of likelihoods as:

$$\mathcal{L}\left(\{\boldsymbol{D}_1 \cdots \boldsymbol{D}_{N_{\mathrm{reg}}}\}|\boldsymbol{T}\right) = \int \prod_{i=1}^{N_{\mathrm{reg}}} \mathcal{L}\left(\boldsymbol{D}_i|\boldsymbol{T};\boldsymbol{\theta}\right) \cdot \mathcal{N}(\boldsymbol{\theta}) \, \mathrm{d}\boldsymbol{\theta}, \tag{3}$$

where the nuisance parameters are common to all analysed regions. The likelihood is sampled around its minimum using an extended Markov-chain Monte Carlo method [127] in order to estimate the posterior probability of all the parameters of interest.

7 Systematic uncertainties

The inclusive and differential measurements are affected by several sources of systematic uncertainty, including experimental uncertainties, signal and background modelling uncertainties, uncertainties due to limited MC sample sizes and uncertainties due to unfolding bias. The individual systematic uncertainty sources are described in this section. The effect of the signal modelling uncertainties is estimated by varying the response matrix. The effects of all other systematic uncertainties are obtained by taking the difference between the relevant systematically varied reconstructed distribution and nominal reconstructed distribution. Two-sided systematic uncertainties are symmetrised by taking half of the difference between the upward and downward variations.

A Bootstrap [128] method is applied in order to estimate the effect of limited MC sample sizes on the systematic uncertainties. Only systematic variations which are found to be significant compared to their statistical precision are kept. When systematic effects are found not to be significant, their respective uncertainty is set to zero. Such method cannot fully remove the effects of the limited MC sample sizes, which are particularly important for the generator modelling uncertainties.

7.1 Experimental uncertainties

The uncertainty in the combined 2015–2018 integrated luminosity is 1.7% [129], obtained using the LUCID-2 detector [130] for the primary luminosity measurements. This systematic uncertainty affects all processes modelled using MC simulation.

The uncertainty in the reweighting of the MC pile-up distribution to match the distribution in data is evaluated by varying the pile-up correction factors used to perform the reweighting within their uncertainties.

Uncertainties associated with the lepton selection arise from the trigger, reconstruction, identification and isolation efficiencies, and the lepton momentum scale and resolution [53, 55]. The uncertainties are obtained from data by using either a tag-and-probe method on events with Z-boson, W-boson, or J/ψ decays [54, 55], or studies of reconstructed distributions of $Z \to \ell^+\ell^-$, $J/\psi \to \ell^+\ell^-$ and $W \to e\nu$ using methods similar to those in Refs. [55, 131].

Uncertainties associated with the small-R jet selection arise from the jet energy scale (JES), the JVT requirement and the jet energy resolution (JER). The uncertainty in the JES is assessed in data [60], using MC-based corrections and in situ techniques. It is broken down into a set of 29 decorrelated nuisance parameters, with contributions from pile-up, jet-flavour composition, single-particle response, and punch-through. Each parameter has different jet p_{T} and η dependencies [132]. The uncertainty in the JVT efficiency comes from the estimation of the residual contamination from pile-up jets after pile-up suppression, and a systematic uncertainty assessed by using different MC generators for simulation of $Z \to \mu\mu$ and $t\bar{t}$ events [61]. The uncertainty in the JER is determined by an eigenvector decomposition strategy similar to that for the JES systematic uncertainties. Eight nuisance parameters take into account various effects evaluated by comparing simulation with data. The overall effect of the JER uncertainty is parameterised in jet p_{T} and η [132].

The efficiency of the flavour-tagging algorithm is measured for each jet flavour using control samples in data and simulation. The uncertainties are related to the b-jet tagging calibration for b-jets, c-jets and light-jets, and comprise nine, four and four eigenvector variations to the tagging efficiencies, respectively [62]. The

uncertainties due to the high-p_{T} extrapolation of the b-jet and c-jet efficiencies are accounted for by two additional nuisance parameters.

The uncertainties of all the $E_{\mathrm{T}}^{\mathrm{miss}}$ components associated with reconstructed objects are propagated in a fully correlated way. Additional uncertainties in the scale and resolution of the soft-track components are considered [68].

The large-R jets in the single-lepton channel have uncertainties associated with their momentum and scale resolution. The scale of the detector response for all relevant jet momenta (p_{T}, m_{jet}, τ_{32}) is derived by comparing the calorimeter response with the tracker response for a matched reference track-jet [66]. To account for the resolution of the detector response, the jet p_{T} is smeared by an additional 2% uncertainty. The jet mass resolution uncertainty is estimated by smearing the jet mass response by an additional 20% (where the nominal response is parameterised in jet p_{T} and $m_{\mathrm{jet}}/p_{\mathrm{T}}$) [133]. A set of 14 nuisance parameters is used to estimate uncertainties due to these effects in the single-lepton boosted channel.

7.2 Signal modelling

During the unfolding procedure, the $t\bar{t}$ signal normalisation is a free parameter common to all bins of the true $\Delta|y_{t\bar{t}}|$ distribution, and its posterior probability is estimated. Therefore, the overall normalisation (affecting all $\Delta|y_{t\bar{t}}|$ bins simultaneously) of each signal modelling uncertainty that compares two specific generator configurations is removed. Only the shape difference affecting the $\Delta|y_{t\bar{t}}|$ bins separately is considered in the following nuisance parameters (NP):

- The $t\bar{t}$ PS+hadronisation NP takes into account the choice of PS, underlying event, and hadronisation models. The uncertainty is evaluated by comparing the $t\bar{t}$ Powheg+Pythia 8 (nominal) sample with the Powheg+Herwig 7 sample.
- The $t\bar{t}$ μ_{f} and $t\bar{t}$ μ_{r} NPs correspond to uncertainties arising from missing higher-order QCD corrections in the ME computation. They are estimated by varying one scale in the ME by factors of 0.5 and 2.0 in the nominal $t\bar{t}$ signal sample, while the other scale is kept at its nominal value, and vice versa.
- The $t\bar{t}$ Var3c NP represents the uncertainty due to variation of the strong coupling in the initial-state PS. The uncertainty is estimated by varying the Var3c parameter from the A14 tune [97] in the nominal $t\bar{t}$ signal sample.
- The $t\bar{t}$ h_{damp} NP characterises the uncertainty associated with the choice of h_{damp} parameter value, which determines the kinematics of the leading emission [134]. In this case, the nominal $t\bar{t}$ sample is compared with a dedicated alternative sample in which the value of the h_{damp} parameter is increased to $3.0\,m_{\mathrm{top}}$.
- The $t\bar{t}$ FSR NP corresponds to the uncertainty arising from FSR. It is obtained using PS weights in the nominal $t\bar{t}$ sample, which vary the renormalisation scale for QCD emission in the FSR by a factor of 2.0 or 0.5 for reduced or enhanced radiation, respectively.

The uncertainty due to the choice of parton distribution functions is obtained using the PDF4LHC15 prescription [135], which utilises a set of 30 separate NPs.

7.3 Background modelling

In the single-lepton channel, the W+jets process is the dominant background in the $1b$-exclusive region. It is a charge asymmetric process, to which a total cross-section uncertainty of 5% [136] is assigned. Variations of W+jets [137] production which alter both its predicted shape and acceptance are used to estimate a modelling uncertainty. By reweighting the nominal W+jets prediction using dedicated MC generator weights, variations are considered for the renormalisation and factorisation scales, matrix-element-to-parton-shower matching CKKW scale [114, 138], and the scale used for the resummation of soft gluon emission. In addition, to account for potential mismodelling of the various flavour contributions of W+jets, three flavour composition variations are considered. The W+b/c/light-jets events are filtered into separate samples and their individual normalisations are varied by ±30% [137].

Single-top production is the dominant background in the dilepton channel and is non-negligible especially in the $2b$-inclusive single-lepton regions. Since the main contribution comes from the tW channel, an uncertainty of 5.3% [139, 140] is assigned to the predicted cross-section. In addition, the MC samples used for $t\bar{t}$ and single-top tW production contain an overlap in the final state, which is removed using the DR scheme. To estimate the uncertainty, the difference between the predictions of the nominal tW sample and the alternative sample using the DS scheme is considered. Furthermore, uncertainties due to PS and hadronisation, ISR and FSR are taken into account for the tW channel as well as for the s- and t-channels. The PS and hadronisation uncertainty is evaluated by comparing the nominal sample with the sample produced with Powheg Box and interfaced with Herwig 7.04. The uncertainties due to ISR and FSR are estimated using varied weights in the ME and in the PS. To simulate higher (lower) ISR, μ_{r} and μ_{f} are varied by a factor of 0.5 (2.0) in the ME. The impact of increased or decreased FSR is evaluated using PS weights, which vary the renormalisation scale for QCD emission in the FSR by a factor of 0.5 or 2.0, respectively. In the dilepton channel, Wt production contributes to the single-top background, while events from s- and t-channel production contribute to the fake-lepton background. Therefore, in the single-lepton channel, the systematic variations associated with Wt production are separated from the systematic variations associated with s- and t-channel production.

In the dilepton channel, Z+jets production is the second most dominant background process in the same-flavour regions. By reweighting the nominal Z+jets prediction using dedicated MC generator weights, variations are considered for the renormalisation and factorisation scales. In addition, a 30% normalisation uncertainty is assigned. In the single-lepton channel, Z+jets production is considered together with other physics backgrounds, described below.

Diboson production is a non-negligible background in the dilepton channel. An uncertainty of 6% is assigned to the predicted diboson cross-section [141]. In the single-lepton channel, diboson production is considered together with other physics backgrounds, described below.

In the matrix method, the real- and fake-lepton efficiencies are parameterised. To estimate the shape uncertainty, an alternative parameterisation of real- and fake-lepton efficiencies is compared with the nominal parameterisation in each region. In addition, a 50% normalisation uncertainty is considered.

Other physics backgrounds making small contributions in the single-lepton channel include Z+jets, diboson, $t\bar{t}V$, and $t\bar{t}H$ production. They are treated as a single background process in the unfolding procedure, and a cross-section normalisation uncertainty of 50% is applied.

Rare SM processes such $t\bar{t}V$ and $t\bar{t}H$ are assigned a cross-section uncertainty of 13% [142].

7.4 Method uncertainties

Given the finite number of events in the $t\bar{t}$ signal sample, the response matrix is estimated with limited statistical precision. To estimate the resulting uncertainty in A_{C}, an Asimov dataset [143] unfolding is repeated 500 times with smeared response matrices (according to the MC statistics) to obtain a distribution of pseudo-experiment results for A_{C}. The width of this distribution is considered as the uncertainty, which is then summed in quadrature with the total uncertainty obtained from the unfolding. The Gaussian smearing is applied to each element of the response matrix.

To evaluate any source of bias from the unfolding procedure, the response of the unfolding is determined from eight pseudo-datasets generated with Protos. Each pseudo-dataset is composed of the nominal $t\bar{t}$ signal, reweighted to simulate a specific injected asymmetry. The injected A_{C} values range between -0.05 and 0.06, depending on the differential variable and bin. By unfolding the eight reweighted pseudo-datasets with the nominal response matrix, including all systematic uncertainties, the uncertainty associated with the unfolding response is calculated as $A_{\mathrm{C}}^{\mathrm{meas}} - (A_{\mathrm{C}}^{\mathrm{meas}} - b)/a$, where a and b are the slope and offset of a linear fit of the generator-level (intrinsic) A_{C} to the unfolded A_{C} of the eight reweighted pseudo-datasets, and $A_{\mathrm{C}}^{\mathrm{meas}}$ is the measured asymmetry value in data. The unfolding bias uncertainty has a negligible impact on the total uncertainty.

8 Results

8.1 $A_{\mathrm{C}}^{t\bar{t}}$ measurement

The measured value of $A_{\mathrm{C}}^{t\bar{t}}$ is inferred from the posterior distribution of $\Delta|y_{t\bar{t}}|$ according to Eq. (1), where the $\Delta|y_{t\bar{t}}|$ posterior is obtained by marginalising the extended likelihood in Eq. (3). The value of $A_{\mathrm{C}}^{t\bar{t}}$ is measured separately for the single-lepton and dilepton channels, combining the four regions of each channel in the unfolding procedure. In order to obtain the final result, all the single-lepton and dilepton regions are combined in the unfolding procedure.

To compute $A_{\mathrm{C}}^{t\bar{t}}$, at least two $\Delta|y_{t\bar{t}}|$ bins are necessary. The $\Delta|y_{t\bar{t}}|$ spectrum is divided into four-bin histograms for all channels/regions and for all differential measurements. While using fewer than four bins results in a smaller $A_{\mathrm{C}}^{t\bar{t}}$ statistical uncertainty, using a larger number of bins allows a more accurate mapping of migrations that change the sign of $\Delta|y_{t\bar{t}}|$ and allows an unbiased measurement of $A_{\mathrm{C}}^{t\bar{t}}$. The $\Delta|y_{t\bar{t}}|$ bin edges are hence chosen to minimise a possible bias in the measurement. As an example, Figure 2 shows the four regions for the two channels in the inclusive case. The optimisation of the $m_{t\bar{t}}$, $p_{\mathrm{T},t\bar{t}}$ and $\beta_{\mathrm{z},t\bar{t}}$ differential bins is based on the number of events they contain. The same $\Delta|y_{t\bar{t}}|$, $m_{t\bar{t}}$, $p_{\mathrm{T},t\bar{t}}$ and $\beta_{\mathrm{z},t\bar{t}}$ bin sizes are used in the single-lepton and dilepton channels as well as in the combination.

As mentioned in Section 7.2, the $t\bar{t}$ signal modelling uncertainties take into account only the shape differences affecting $\Delta|y_{t\bar{t}}|$ bins. However, when combining N_{reg} regions, the different $t\bar{t}$ signal models may have different acceptances for signal events to enter a particular region. To allow independent $t\bar{t}$ signal normalisation in each of the N_{reg} combined regions, $N_{\mathrm{reg}} - 1$ signal normalisation parameters[4]

[4] Since the overall $t\bar{t}$ signal normalisation is a free parameter because of the unfolding, only $N_{\mathrm{reg}} - 1$ additional degrees of freedom are necessary.

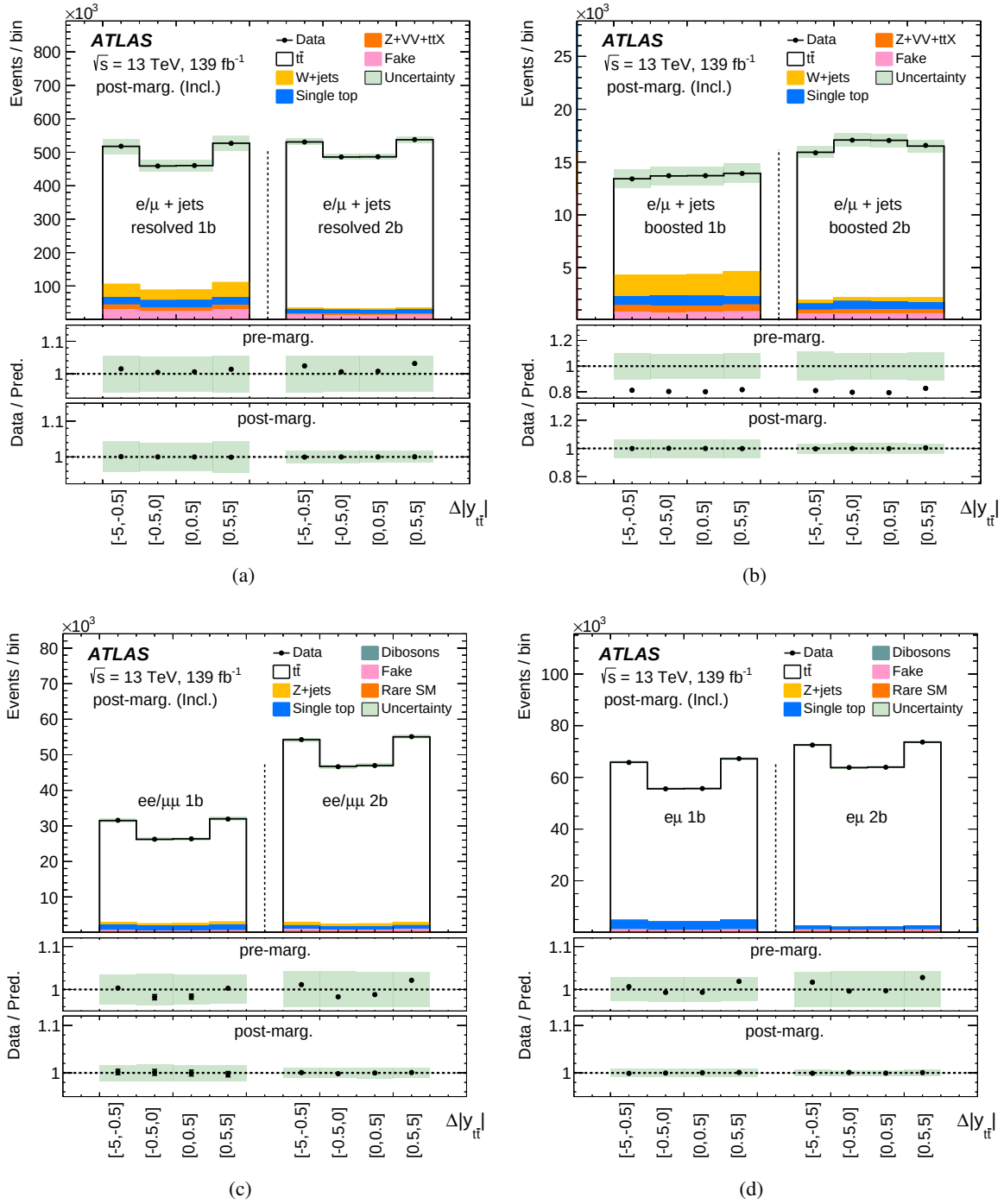

Figure 2: Comparison between the data and the prediction for the reconstructed $\Delta|y_{t\bar{t}}|$ in the inclusive $A_C^{t\bar{t}}$ measurement in the (a) single-lepton resolved, (b) single-lepton boosted, (c) dilepton $ee + \mu\mu$ and (d) dilepton $e\mu$ region. The ratio of data to prediction is shown before and after marginalisation within FBU. Shaded bands correspond to the total uncertainty of the prediction. The signal modelling uncertainties do not include normalisation effects because the overall acceptance difference cancels out in the $A_C^{t\bar{t}}$ observable. Before the marginalisation, a normalisation difference of the order of 20% between the data and predictions is observed in the single-lepton boosted channel. This overestimation by the MC simulation at large values of top p_T (>300 GeV), is confirmed by differential cross-sections measurements. In the unfolding, this overestimation is absorbed by the normalisation parameters in the boosted regions.

$\boldsymbol{K}_{\text{norm}}$ are inserted into the likelihood with a uniform prior $\pi(\boldsymbol{K}_{\text{norm}})$. The posterior probability density thus becomes:

$$p\left(\boldsymbol{T}|\{\boldsymbol{D}_1 \cdots \boldsymbol{D}_{N_{\text{reg}}}\}\right) = \int \prod_{i=1}^{N_{\text{reg}}} \mathcal{L}\left(\boldsymbol{D}_i|\boldsymbol{R}_i(\boldsymbol{T}, \boldsymbol{K}_{\text{norm}}; \boldsymbol{\theta}_{\text{r}}), \boldsymbol{B}_i(\boldsymbol{\theta}_{\text{r}}, \boldsymbol{\theta}_{\text{b}}, \boldsymbol{\gamma})\right) \mathcal{N}(\boldsymbol{\theta}_{\text{r}})\, \mathcal{N}(\boldsymbol{\theta}_{\text{b}})\, \pi(\boldsymbol{T})\, \pi(\boldsymbol{K}_{\text{norm}})\, \mathrm{d}\boldsymbol{\theta}_{\text{r}}\, \mathrm{d}\boldsymbol{\theta}_{\text{b}}, \tag{4}$$

where $\boldsymbol{B} = \boldsymbol{B}(\boldsymbol{\theta}_{\text{r}}, \boldsymbol{\theta}_{\text{b}}, \boldsymbol{\gamma})$ is the total background prediction, the probability densities π are uniform priors and $\boldsymbol{R}$ is the reconstructed signal prediction. Three categories of nuisance parameters are considered: the normalisation of the background processes ($\boldsymbol{\theta}_{\text{b}}$), the uncertainties in the background prediction due to limited MC sample sizes ($\boldsymbol{\gamma}$), and the uncertainties associated with signal and background modelling, object identification, reconstruction and calibrations ($\boldsymbol{\theta}_{\text{r}}$). Uncertainties belonging to the last category affect both the reconstructed distribution of the $t\bar{t}$ signal and the background prediction. The $\boldsymbol{\gamma}$ nuisance parameters are per-bin variables, allowing the total background prediction to fluctuate within its statistical uncertainty [144]. In each region, four $\boldsymbol{\gamma}$ nuisance parameters correspond to four $\Delta|y_{t\bar{t}}|$ bins. In the differential measurements, four $\boldsymbol{\gamma}$ nuisance parameters are considered in each differential bin, in each region.

When combining multiple regions in the unfolding procedure, assumptions have to be made about the correlations of systematic uncertainties. The experimental uncertainties are treated as fully correlated across all combined regions in all $A_{\text{C}}^{t\bar{t}}$ measurements. For the $t\bar{t}$ signal and background modelling uncertainties, several decorrelation schemes are studied. For these uncertainties, constraints may lead to an unjustified reduction of the uncertainty. This is because model comparisons include multiple effects, where implicit assumptions are made about their correlation structure. To limit the number of NPs, the modelling uncertainties are correlated among regions unless they are significantly constrained (by more than about 30%). For a small number of cases in which decorrelating across the regions is found to increase the total uncertainty by 5%–20%, the more conservative scheme is chosen. Decorrelating more uncertainties increases the complexity of the FBU marginalisation but does not lead to a sizeable increase in the total uncertainty. The impact of the decorrelation scheme on the unfolded $A_{\text{C}}^{t\bar{t}}$ mean value is found to be negligible. Overall, the changes to the asymmetry value and uncertainty due to the decorrelation scheme choice are much smaller than the statistical uncertainty in all measurement regions.

In the single-lepton channel measurement, the following decorrelation scheme is used:

- With the exception of the $t\bar{t}$ Var3c and PDF uncertainties, all of the signal modelling uncertainties are decorrelated between the resolved and boosted regions, to reduce the constraints, given the significantly different kinematics in these regions. The aforementioned exceptions are kept correlated.
- In order to reduce constraints on the systematic uncertainties, the $t\bar{t}$ PS+hadronisation uncertainty is decorrelated between all of the combined regions.
- In addition, to mitigate stronger constraints in the differential $A_{\text{C}}^{t\bar{t}}$ measurements, the $t\bar{t}$ h_{damp}, $t\bar{t}$ FSR and $t\bar{t}$ PS+hadronisation systematic uncertainties are decorrelated between differential bins, but the $\Delta|y_{t\bar{t}}|$ bins of the systematic variation are kept correlated within a given differential bin.
- For the background modelling uncertainties, only the single-top PS+hadronisation, single-top FSR and W+jets μ_{r} and μ_{f} scales are decorrelated between the resolved and boosted regions. In the

differential measurements, single-top Wt-channel FSR systematic uncertainties are decorrelated between differential bins as well.

- The fake-lepton shape and normalisation uncertainties are decorrelated among all combined regions, given that the fake-events composition in each region is expected to be different.

In the dilepton channel measurement, a different decorrelation scheme was used:

- All of the $t\bar{t}$ signal and background modelling uncertainties are fully correlated across all combined regions, with the exception of the Z+jets and fake-lepton normalisation uncertainties. This differs from the single-lepton channel (where the resolved and boosted regions have very different kinematics) because the dilepton channel includes only the resolved topology.
- The Z+jets and fake-lepton normalisation uncertainties are decorrelated between individual regions as they have either very different contributions or compositions in the respective regions.
- To reduce the constraints on the systematic uncertainties in the differential measurements, the $t\bar{t}$ h_{damp} and $t\bar{t}$ PS+hadronisation systematic uncertainties are decorrelated between differential bins, but the $\Delta|y_{t\bar{t}}|$ bins of the systematic variation are kept correlated within a given differential bin.

Finally, in the combination, the following decorrelation scheme is adopted:

- In the inclusive measurement, the systematic uncertainties for $t\bar{t}$ h_{damp}, $t\bar{t}$ μ_{r} and μ_{f} scales, $t\bar{t}$ FSR and single-top Wt channel FSR are correlated across single-lepton resolved and dilepton regions, while they are decorrelated from the single-lepton boosted regions, given the significantly different kinematics in these regions. In order to reduce the number of constraints, the $t\bar{t}$ PS+hadronisation is decorrelated among single-lepton and dilepton channels. A single NP is used for all dilepton regions, while the uncertainty is decorrelated among the individual single-lepton regions. The $t\bar{t}$ Var3c and PDF uncertainties are kept correlated across all combined regions.
- In the differential measurements, the $t\bar{t}$ μ_{r} and μ_{f} scales are correlated among the single-lepton resolved and dilepton regions, while they are uncorrelated with the single-lepton boosted regions. The $t\bar{t}$ PS+hadronisation, $t\bar{t}$ h_{damp}, $t\bar{t}$ FSR as well as single-top PS+hadronisation and single-top FSR are decorrelated between single-lepton resolved, single-lepton boosted and dilepton regions. In addition, $t\bar{t}$ PS+hadronisation, $t\bar{t}$ h_{damp} and single-top FSR are decorrelated between differential bins, with $t\bar{t}$ PS+hadronisation also decorrelated between 1-b-tag exclusive and 2-b-tag inclusive regions. The $t\bar{t}$ FSR is also decorrelated between differential bins, but only in single-lepton regions, where sizeable constraints are observed otherwise.
- Similarly to the single-lepton channel measurement, the W+jets μ_{r} and μ_{f} scales are decorrelated between single-lepton resolved and single-lepton boosted regions.
- The single-top Wt normalisation is correlated across all regions.
- The fake-lepton shape uncertainty in the single-lepton regions and fake-lepton normalisation uncertainties are decorrelated among all combined regions.
- For the other background processes, usually their yields are small in one of the combined channels, and therefore the background contributions are combined into a single contribution. The normalisation uncertainties of the other background processes are then uncorrelated between single-lepton and dilepton regions. In addition, the Z+jets normalisation uncertainty is decorrelated among dilepton regions.

As shown in the bottom panels of Figure 2, the marginalisation procedure significantly reduces the total uncertainty and results in better overall agreement between data and predictions.

8.1.1 Comparison with the Standard Model prediction

The SM prediction of $A_{\mathrm{C}}^{t\bar{t}}$ is obtained by performing fixed-order calculations at NNLO in the perturbative expansion in the strong coupling constant of QCD, with NLO EW corrections [19]. Fully differential predictions are available, including a detailed analysis of the charge asymmetry at the LHC [145, 146]. The same calculation is compared with Tevatron results for the forward–backward asymmetry [10, 147].

The $A_{\mathrm{C}}^{t\bar{t}}$ predictions are calculated using $m_{\mathrm{top}} = 172.5$ GeV [19]. The PDF of the proton is taken from the LUXqed17 NNLO PDF set (LUXqed17_plus_PDF4LHC15_nnlo_100) [19]. The central value and uncertainties are based on the PDF4LHC 2015 recommendation. The photon content of the proton is determined following Refs. [148, 149]. A dynamical renormalisation and factorisation scale [150] is used, with the nominal value μ_0 chosen as $H_{\mathrm{T}}/4$, where $H_{\mathrm{T}} = \sqrt{m_t^2 + p_{\mathrm{T},t}^2} + \sqrt{m_{\bar{t}}^2 + p_{\mathrm{T},\bar{t}}^2}$. The scale uncertainty band indicates the maximum and the minimum value of the asymmetry obtained from an independent variation of the renormalisation and factorisation scales by factors of 2 or 0.5 around μ_0. The variations in which one scale is multiplied by 2 while the other scale is divided by 2 are excluded. The MC integration uncertainty is typically smaller than the scale uncertainty. Finally, the scale and MC integration uncertainties are added in quadrature.

Tables 3–4 and Figures 3–4 show a comparison of the measured $A_{\mathrm{C}}^{t\bar{t}}$ asymmetry with the SM prediction. The measured asymmetry is consistent with the NNLO prediction in Ref. [19] within the uncertainty. In addition, the impact of the linear term of the C_{tu}^8 Wilson coefficient on the $A_{\mathrm{C}}^{t\bar{t}}$ prediction (see Section 8.3) is shown for the inclusive and $m_{t\bar{t}}$ differential measurements.

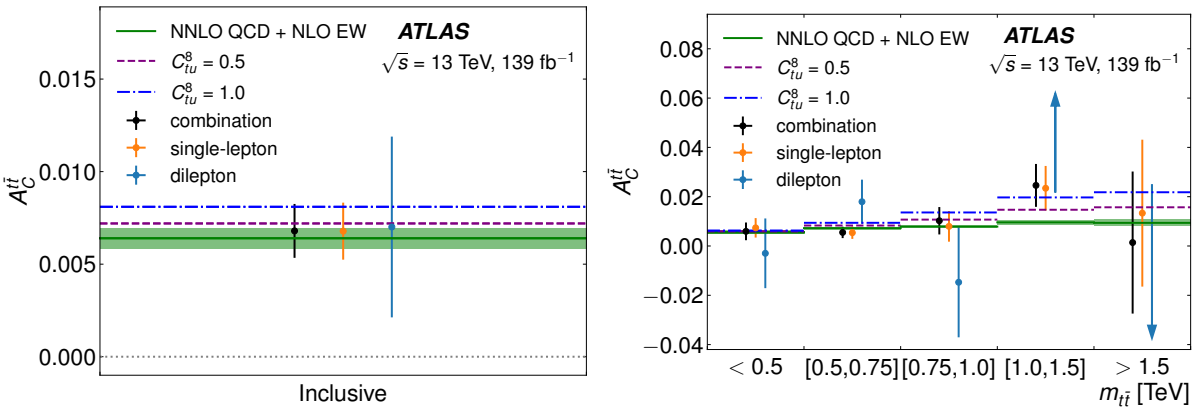

(a) (b)

Figure 3: The unfolded inclusive (a) and differential charge asymmetries as a function of the invariant mass (b) of the reconstructed top-quark pair in data. Vertical bars correspond to the total uncertainties. Shaded regions show SM theory predictions calculated at NNLO in QCD and NLO in EW theory. The impact of the linear term of the C_{tu}^8 Wilson coefficient on the $A_{\mathrm{C}}^{t\bar{t}}$ prediction for two different values is shown as dashed lines. In the dilepton channel, the two points corresponding to the higher invariant masses have large statistical uncertainty. A partial vertical uncertainty bar is shown, while the central point is in the direction of the associated arrow, with a value given in Table 3.

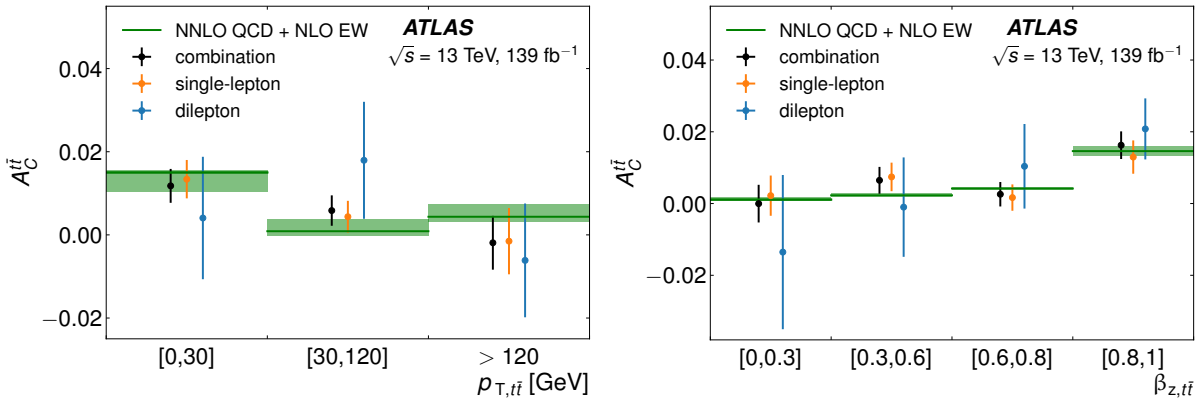

(a) (b)

Figure 4: The unfolded differential charge asymmetries as a function of the transverse momentum (a) and the longitudinal boost (b) of the reconstructed top-quark pair in data. Vertical bars correspond to the total uncertainties. Shaded regions show SM theory predictions calculated at NNLO in QCD and NLO in EW theory.

Table 3: Results with statistical, systematic and the total uncertainties for the inclusive and $m_{t\bar{t}}$ differential $A_{\mathrm{C}}^{t\bar{t}}$ measurements. The statistical uncertainty is obtained by unfolding the data, but excluding all the nuisance parameters. The squared systematic uncertainty is evaluated as the difference between the squares of the total uncertainty and the statistical uncertainty. The SM predictions are calculated at NNLO in QCD and NLO in EW theory.

			Data 139 fb^{-1}				SM prediction
		Channel	$A_{\mathrm{C}}^{t\bar{t}}$	Stat.	Syst.	Total unc.	
Inclusive		Single-lepton	0.0068	0.0011	0.0011	0.0015	$0.0064^{+0.0005}_{-0.0006}$
		Dilepton	0.0070	0.0034	0.0035	0.0049	
		Combination	0.0068	0.0010	0.0010	0.0015	
$m_{t\bar{t}}$	< 500 GeV	Single-lepton	0.0074	0.0028	0.0028	0.0039	$0.0056^{+0.0006}_{-0.0006}$
		Dilepton	−0.0030	0.0114	0.0084	0.0141	
		Combination	0.0059	0.0027	0.0024	0.0036	
	500–750 GeV	Single-lepton	0.0054	0.0020	0.0015	0.0025	$0.0072^{+0.0006}_{-0.0006}$
		Dilepton	0.0180	0.0061	0.0066	0.0089	
		Combination	0.0055	0.0019	0.0013	0.0023	
	750–1000 GeV	Single-lepton	0.0080	0.0048	0.0040	0.0062	$0.0079^{+0.0004}_{-0.0006}$
		Dilepton	−0.0147	0.0188	0.0120	0.0223	
		Combination	0.0102	0.0046	0.0030	0.0056	
	1000–1500 GeV	Single-lepton	0.0234	0.0075	0.0050	0.0090	$0.0096^{+0.0009}_{-0.0009}$
		Dilepton	0.0663	0.0371	0.0244	0.0444	
		Combination	0.0246	0.0074	0.0045	0.0087	
	> 1500 GeV	Single-lepton	0.0133	0.0288	0.0076	0.0298	$0.0094^{+0.0015}_{-0.0011}$
		Dilepton	−0.1313	0.1444	0.0590	0.1560	
		Combination	0.0014	0.0280	0.0068	0.0288	

Table 4: Results with statistical, systematic and the total uncertainties for the $p_{\mathrm{T},t\bar{t}}$ and $\beta_{\mathrm{z},t\bar{t}}$ differential $A_{\mathrm{C}}^{t\bar{t}}$ measurements. The statistical uncertainty is obtained by unfolding the data, but excluding all the nuisance parameters. The squared systematic uncertainty is evaluated as the difference between the squares of the total uncertainty and the statistical uncertainty. The SM predictions are calculated at NNLO in QCD and NLO in EW theory.

			Data 139 fb^{-1}				SM prediction
		Channel	$A_{\mathrm{C}}^{t\bar{t}}$	Stat.	Syst.	Total unc.	
$p_{\mathrm{T},t\bar{t}}$	< 30 GeV	Single-lepton	0.0134	0.0034	0.0031	0.0046	$0.0150^{+0.0006}_{-0.0046}$
		Dilepton	0.0041	0.0105	0.0103	0.0147	
		Combination	0.0118	0.0032	0.0025	0.0041	
	30–120 GeV	Single-lepton	0.0044	0.0027	0.0027	0.0038	$0.0009^{+0.0028}_{-0.0012}$
		Dilepton	0.0179	0.0096	0.0103	0.0141	
		Combination	0.0058	0.0026	0.0026	0.0037	
	> 120 GeV	Single-lepton	−0.0015	0.0047	0.0064	0.0080	$0.0044^{+0.0030}_{-0.0014}$
		Dilepton	−0.0061	0.0122	0.0062	0.0137	
		Combination	−0.0019	0.0044	0.0048	0.0065	
$\beta_{\mathrm{z},t\bar{t}}$	0–0.3	Single-lepton	0.0022	0.0040	0.0039	0.0056	$0.0011^{+0.0005}_{-0.0004}$
		Dilepton	−0.0135	0.0179	0.0119	0.0215	
		Combination	<0.0001	0.0039	0.0035	0.0052	
	0.3–0.6	Single-lepton	0.0074	0.0031	0.0025	0.0040	$0.0023^{+0.0006}_{-0.0004}$
		Dilepton	−0.0010	0.0116	0.0076	0.0139	
		Combination	0.0065	0.0029	0.0023	0.0037	
	0.6–0.8	Single-lepton	0.0017	0.0028	0.0023	0.0037	$0.0042^{+0.0003}_{-0.0003}$
		Dilepton	0.0104	0.0090	0.0076	0.0118	
		Combination	0.0026	0.0027	0.0021	0.0034	
	0.8–1.0	Single-lepton	0.0130	0.0026	0.0038	0.0046	$0.0146^{+0.0012}_{-0.0014}$
		Dilepton	0.0208	0.0069	0.0050	0.0085	
		Combination	0.0163	0.0024	0.0030	0.0039	

8.1.2 Uncertainties

In order to determine the relative importance of systematic uncertainties, a ranking of individual nuisance parameters is performed. For each uncertainty, the unfolding is repeated with the corresponding NP fixed to $+/-1\sigma$ around the NP post-marginalisation mean value. The difference between the nominal unfolded A_{C} result and the result with the shifted NP is considered as the pre-marginalisation ranking estimate of the uncertainty. Similarly, a ranking where the NP is varied by $+/-c$, where c is the post-marginalisation constraint, is performed and the post-marginalisation uncertainty ranking is obtained. This approach hence takes into account post-marginalisation correlations between the ranked systematic uncertainty and other uncertainties. The rankings of the leading systematic uncertainties are summarised in Tables 5 and 6 for the inclusive and $m_{t\bar{t}}$ differential $A_{\mathrm{C}}^{t\bar{t}}$ combined measurements, respectively. Tables for the $p_{\mathrm{T},t\bar{t}}$ and $\beta_{z,t\bar{t}}$ differential measurements can be found in Appendix A.1. In the tables, the information about constraints can be obtained by comparing the pre-marginalisation and post-marginalisation impacts. The strongest constraints reduce the uncertainties to about 60%–70% of the pre-marginalisation value, with the exception of the third $m_{t\bar{t}}$ bin. In this bin, the constraint related to the $t\bar{t}$ modelling impact reduces the pre-marginalisation uncertainty by 50%. A larger reduction in the uncertainty can be seen in Figure 2, due to the inclusion of systematic uncertainties with mostly normalisation effect on $\Delta|y_{t\bar{t}}|$ distribution, but with negligible effect on $A_{\mathrm{C}}^{t\bar{t}}$.

Table 5: Impact of systematic uncertainties on the measurement of inclusive $A_{\mathrm{C}}^{t\bar{t}}$, grouped into categories. The impact of each category is obtained by summing the symmetrised ranking impact of the respective individual uncertainties in quadrature. The total uncertainty differs from the sum-in-quadrature of the groups due to post-marginalisation nuisance parameter correlations in the unfolding.

	Post-marg. (pre-marg.) impact ×100
$t\bar{t}$ modelling	0.06 (0.08)
$t\bar{t}$ normalisation (flat prior)	0.02
Background modelling	0.04 (0.05)
Monte Carlo statistics	0.05
Small-R JES	0.03 (0.03)
Small-R JER	0.03 (0.03)
Large-R JES, JER	0.01 (0.01)
Leptons, $E_{\mathrm{T}}^{\mathrm{miss}}$	0.02 (0.03)
b-tagging eff.	0.01 (0.01)
Pile-up, JVT, luminosity	0.01 (0.01)
Statistical uncertainty	0.10
Total uncertainty	0.15

Table 6: Impact of systematic uncertainties on the measurement of $A_{\mathrm{C}}^{t\bar{t}}$ vs $m_{t\bar{t}}$, grouped into categories. The impact of each category is obtained by summing the symmetrised ranking impact of the respective individual uncertainties in quadrature. The total uncertainty differs from the sum-in-quadrature of the groups due to post-marginalisation nuisance parameter correlations in the unfolding.

	Post-marg. (pre-marg.) impact ×100				
$m_{t\bar{t}}$ bin [GeV]	< 500	500–750	750–1000	1000–1500	> 1500
$t\bar{t}$ modelling	0.15 (0.22)	0.07 (0.10)	0.14 (0.27)	0.31 (0.45)	0.64 (0.80)
$t\bar{t}$ normalisation (flat prior)	0.06	0.02	0.08	0.06	0.18
Background modelling	0.09 (0.11)	0.06 (0.08)	0.13 (0.15)	0.22 (0.28)	0.84 (1.02)
Monte Carlo statistics	0.13	0.08	0.20	0.30	1.02
Small-R JES	0.09 (0.10)	0.05 (0.06)	0.13 (0.15)	0.15 (0.17)	0.43 (0.52)
Small-R JER	0.11 (0.16)	0.03 (0.05)	0.09 (0.15)	0.21 (0.29)	0.42 (0.65)
Large-R JES, JER	0.02 (0.02)	0.02 (0.02)	0.02 (0.03)	0.05 (0.05)	0.19 (0.28)
Leptons, $E_{\mathrm{T}}^{\mathrm{miss}}$	0.04 (0.06)	0.03 (0.04)	0.08 (0.10)	0.06 (0.08)	0.26 (0.39)
b-tagging eff.	0.02 (0.02)	0.01 (0.01)	0.03 (0.03)	0.03 (0.04)	0.27 (0.30)
Pile-up, JVT, luminosity	0.01 (0.01)	0.01 (0.01)	0.01 (0.01)	0.04 (0.04)	0.02 (0.02)
Statistical uncertainty	0.27	0.19	0.46	0.74	2.80
Total uncertainty	0.36	0.23	0.56	0.87	2.88

8.2 $A_{\mathrm{C}}^{\ell\bar{\ell}}$ measurement

Similarly to $A_{\mathrm{C}}^{t\bar{t}}$ measurements, the measured $A_{\mathrm{C}}^{\ell\bar{\ell}}$ is inferred from the posterior distribution of $\Delta|\eta_{\ell\bar{\ell}}|$ according to Eq. (2), where the $\Delta|\eta_{\ell\bar{\ell}}|$ posterior is obtained by marginalising the extended likelihood in Eq. (4). The $A_{\mathrm{C}}^{\ell\bar{\ell}}$ value is measured in the dilepton channel only, combining four dilepton regions. The $\Delta|\eta_{\ell\bar{\ell}}|$ distribution is split into four bins in all regions and in each differential bin of all differential measurements. The $m_{\ell\bar{\ell}}$, $p_{\mathrm{T},\ell\bar{\ell}}$ and $\beta_{\mathrm{z},\ell\bar{\ell}}$ differential bins are chosen in a way that compromises between data-event counts and event migration due to poor reconstruction. For the systematic uncertainties, the same correlation scheme as in the dilepton channel $A_{\mathrm{C}}^{t\bar{t}}$ measurement is used.

As shown in Figure 5, the marginalisation procedure reduces the total uncertainty significantly and results in better agreement between the data and the predictions.

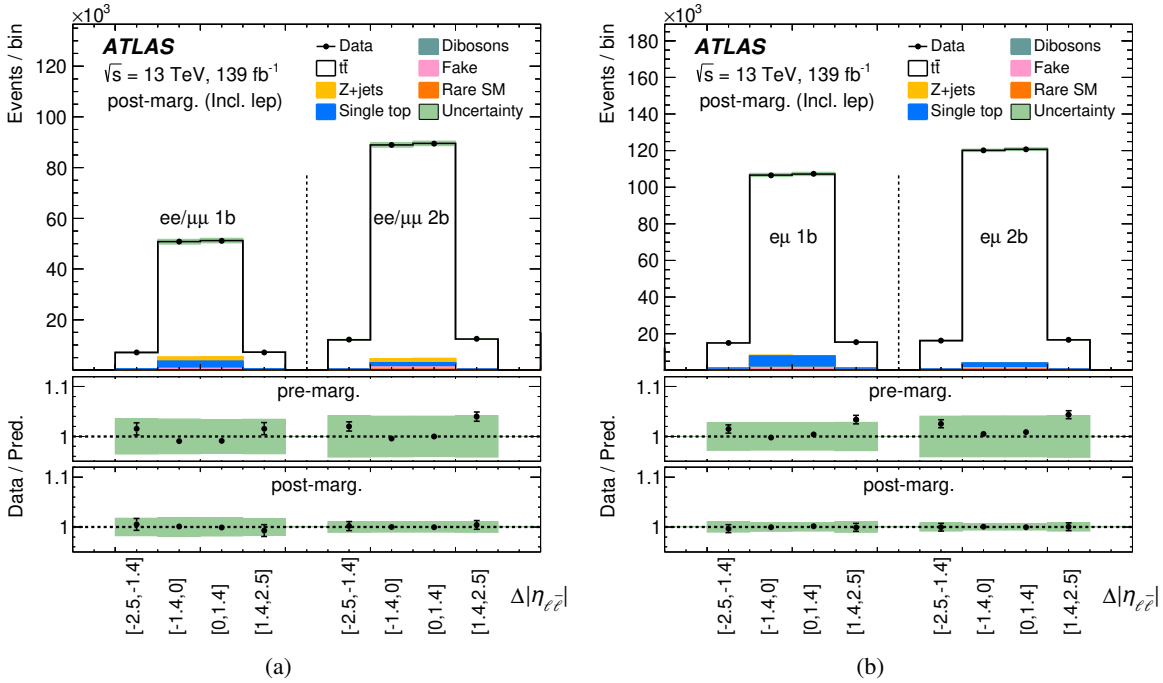

(a) (b)

Figure 5: Comparison between the data and the prediction for the reconstructed $\Delta|\eta_{\ell\bar{\ell}}|$ in the inclusive $A_{\mathrm{C}}^{\ell\bar{\ell}}$ measurement in the (a) dilepton $ee + \mu\mu$ and (b) dilepton $e\mu$ region. The ratio of data to prediction is shown before and after marginalisation within FBU. Shaded bands correspond to the total uncertainty of the prediction. The signal modelling uncertainties do not include normalisation effects because the overall acceptance difference cancels out in the $A_{\mathrm{C}}^{\ell\bar{\ell}}$ observable.

8.2.1 Comparison with the Standard Model prediction

The SM prediction of $A_{\mathrm{C}}^{\ell\bar{\ell}}$ has been calculated at NLO in SM gauge couplings, including corrections up to order α_{s}^3 in the QCD coupling and the mixed QCD–QED and mixed QCD–weak-interaction corrections [20]. Fully differential predictions are available, including a detailed analysis of the charge asymmetry at the LHC [20].

The $A_{\mathrm{C}}^{\ell\bar{\ell}}$ predictions are calculated using $m_{\mathrm{top}} = 173.34$ GeV, $\alpha_{\mathrm{QED}}(m_Z) = 0.008$ and the weak mixing angle $\sin^2\theta_{\mathrm{W}} = 0.23$ [20]. The PDF of the proton is taken from the CT10 set [85]. The same value of $\mu = m_{\mathrm{top}}$ is used for both the renormalisation scale and factorisation scale. The scale uncertainty band indicates the minimum and the maximum value of the asymmetry obtained by varying both scales by a factor of 0.5 or 2.0 respectively.

Figure 6 and Table 7 show a comparison of the measured $A_{\mathrm{C}}^{\ell\bar{\ell}}$ asymmetry with the SM prediction. The measured asymmetry is consistent with NLO calculations [20].

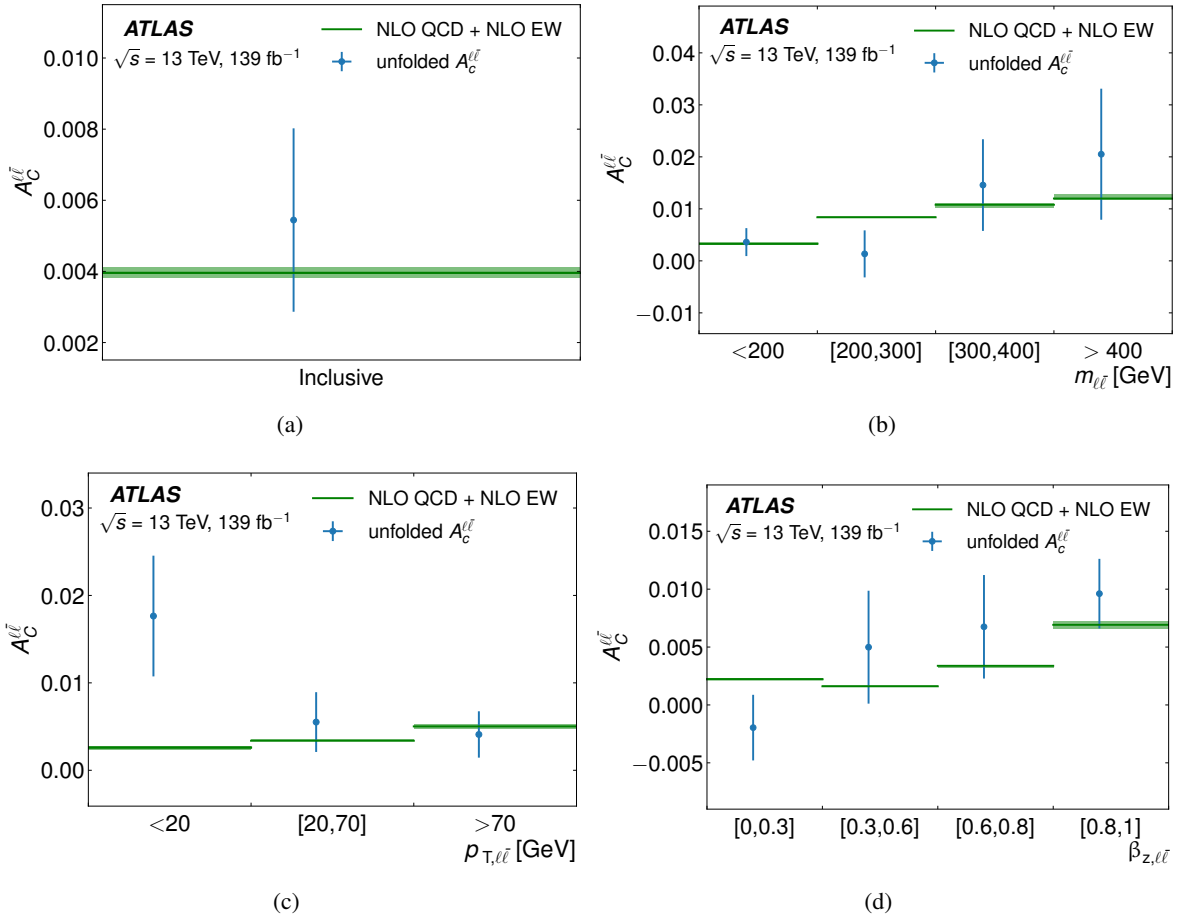

Figure 6: The unfolded inclusive (a) and differential leptonic asymmetries as a function of the invariant mass (b), transverse momentum (c), and the longitudinal boost (d) of the reconstructed lepton pair in dilepton channel data. Shaded regions show SM theory predictions calculated at NLO in QCD and NLO in EW theory. Vertical bars correspond to the total uncertainties.

Table 7: Results of the inclusive and differential $A_{\mathrm{C}}^{\ell\bar{\ell}}$ measurements, including statistical, systematic and total uncertainties. The statistical uncertainty is obtained by unfolding the data, excluding all the nuisance parameters. The squared systematic uncertainty is evaluated as the difference between the squares of the total uncertainty and the statistical uncertainty. The SM predictions are calculated at NLO in QCD and NLO in EW theory.

		Data 139 fb^{-1}				SM prediction
		$A_{\mathrm{C}}^{\ell\bar{\ell}}$	Stat.	Syst.	Total unc.	
Inclusive		0.0054	0.0012	0.0023	0.0026	$0.0040^{+0.0002}_{-0.0001}$
$m_{\ell\bar{\ell}}$	< 200 GeV	0.0036	0.0014	0.0023	0.0027	$0.0033^{+0.0001}_{-0.0001}$
	200–300 GeV	0.0013	0.0041	0.0020	0.0046	$0.0084^{+0.0002}_{-0.0001}$
	300–400 GeV	0.0146	0.0085	0.0030	0.0090	$0.0108^{+0.0003}_{-0.0006}$
	> 400 GeV	0.0205	0.0123	0.0036	0.0128	$0.0120^{+0.0009}_{-0.0002}$
$p_{\mathrm{T},\ell\bar{\ell}}$	< 20 GeV	0.0176	0.0063	0.0031	0.0070	$0.0026^{+0.0002}_{-0.0002}$
	20–70 GeV	0.0055	0.0020	0.0028	0.0034	$0.0034^{+0.0001}_{<0.0001}$
	> 70 GeV	0.0041	0.0018	0.0020	0.0027	$0.0050^{+0.0002}_{-0.0003}$
$\beta_{\mathrm{z},\ell\bar{\ell}}$	0–0.3	−0.0020	0.0028	0.0008	0.0029	$0.0022^{+0.0001}_{-0.0001}$
	0.3–0.6	0.0050	0.0024	0.0043	0.0049	$0.0016^{+0.0001}_{-0.0001}$
	0.6–0.8	0.0068	0.0026	0.0037	0.0045	$0.0034^{<0.0001}_{-0.0001}$
	0.8–1.0	0.0096	0.0028	0.0014	0.0031	$0.0069^{+0.0003}_{-0.0003}$

8.2.2 Uncertainties

The rankings of the leading systematic uncertainties are summarised in Tables 8 and 9 for the inclusive and $m_{\ell\bar{\ell}}$ differential $A_{\mathrm{C}}^{\ell\bar{\ell}}$ measurements, respectively. Tables for the $p_{\mathrm{T},\ell\bar{\ell}}$ and $\beta_{\mathrm{z},\ell\bar{\ell}}$ differential measurements can be found in Appendix A.2. In the tables, the information about constraints can be obtained by comparing the pre-marginalisation and post-marginalisation impacts. The strongest constraints reduce the uncertainties to about 80%–90% of the pre-marginalisation value (e.g. for $t\bar{t}$ signal modelling). For some systematic uncertainties with smaller impacts (e.g. b-tagging efficiency in the $m_{\ell\bar{\ell}}$ differential measurement), constraints reducing the uncertainties to 65% of the pre-marginalisation values can be found. A larger reduction in the uncertainty can be seen in Figure 5, due to the inclusion of systematic uncertainties with mostly normalisation effect on $\Delta|\eta_{\ell\bar{\ell}}|$ distribution, but with negligible effect on $A_{\mathrm{C}}^{\ell\bar{\ell}}$.

Table 8: Impact of systematic uncertainties on the measurement of inclusive $A_{\mathrm{C}}^{\ell\bar{\ell}}$, grouped into categories. The impact of each category is obtained by summing the symmetrised ranking impact of the respective individual uncertainties in quadrature. The total uncertainty differs from the sum-in-quadrature of the groups due to post-marginalisation nuisance parameter correlations in the unfolding.

	Post-marg. (pre-marg.) impact ×100
$t\bar{t}$ modelling	0.20 (0.22)
$t\bar{t}$ normalisation (flat prior)	0.06
Background modelling	0.02 (0.02)
Monte Carlo statistics	0.04
Small-R JES	0.03 (0.03)
Small-R JER	0.06 (0.06)
Leptons, $E_{\mathrm{T}}^{\mathrm{miss}}$	0.01 (0.01)
b-tagging eff.	<0.01 (<0.01)
Pile-up, JVT, luminosity	0.01 (0.01)
Statistical uncertainty	0.12
Total uncertainty	0.26

Table 9: Impact of systematic uncertainties on the measurement of $A_{\mathrm{C}}^{\ell\bar{\ell}}$ vs $m_{\ell\bar{\ell}}$, grouped into categories. The impact of each category is obtained by summing the symmetrised ranking impact of the respective individual uncertainties in quadrature. The total uncertainty differs from the sum-in-quadrature of the groups due to post-marginalisation nuisance parameter correlations in the unfolding.

	Post-marg. (pre-marg.) impact ×100			
$m_{\ell\bar{\ell}}$ bin [GeV]	< 200	200–300	300–400	> 400
$t\bar{t}$ modelling	0.18 (0.21)	0.17 (0.21)	0.20 (0.23)	0.15 (0.15)
$t\bar{t}$ normalisation (flat prior)	0.03	0.03	0.03	0.01
Background modelling	0.02 (0.02)	0.05 (0.06)	0.06 (0.07)	0.06 (0.06)
Monte Carlo statistics	0.05	0.09	0.19	0.26
Small-R JES	0.04 (0.05)	0.02 (0.02)	0.03 (0.03)	0.08 (0.09)
Small-R JER	0.03 (0.03)	0.05 (0.05)	0.07 (0.07)	0.07 (0.06)
Leptons, $E_{\mathrm{T}}^{\mathrm{miss}}$	0.02 (0.02)	0.03 (0.02)	0.06 (0.06)	0.09 (0.08)
b-tagging eff.	0.01 (0.01)	0.02 (0.02)	0.02 (0.02)	0.02 (0.03)
Pile-up, JVT, luminosity	0.01 (0.01)	0.01 (0.01)	0.02 (0.01)	0.01 (0.02)
Statistical uncertainty	0.14	0.41	0.85	1.23
Total uncertainty	0.27	0.46	0.90	1.28

8.3 SMEFT interpretation of the $A_{\mathrm{C}}^{t\bar{t}}$ results

The combined results of the $A_{\mathrm{C}}^{t\bar{t}}$ measurement are interpreted in the SMEFT. In this formalism the SM Lagrangian is extended with higher-dimensional operators that encode the effect of new-physics phenomena

at a scale beyond the direct reach of the experiment. A general effective Lagrangian is written as follows:

$$\mathcal{L}_{\text{eff}} = \mathcal{L}_{\text{SM}} + \frac{1}{\Lambda^2}\sum_i C_i O_i + O\left(\Lambda^{-4}\right),$$

where $\mathcal{L}_{\text{SM}}$ represents the SM Lagrangian, Λ represents the characteristic new-physics scale and C_i are the Wilson coefficients of the dimension-six operators O_i. Any observable receives contributions proportional to Λ^{-2}, from the interference of dimension-six operators with SM amplitudes. The squares of dimension-six operators are also computed, and these give rise to contributions of order Λ^{-4}. However, further terms of the same order, from the interference of dimension-eight operators with the SM, are ignored. For this expansion to provide meaningful results, C_i/Λ^2 must be small. For typical values of the coupling strength C_i of the dimension-six operators, that implies that Λ must exceed several TeV. An indication of the validity of the expansion is provided by comparing the results obtained from a *linear* parameterisation that includes only Λ^{-2} terms with the results of a *quadratic* fit that also takes into account the known Λ^{-4} terms from dimension-six operators squared.

In the following, the left-handed (L) quark doublets of the first two generations are represented by $q_i = (u_\text{L}, d_\text{L}), (c_\text{L}, s_\text{L})$, and the doublet of the third generation is given by $Q = (t_\text{L}, b_\text{L})$. Right-handed (R) quarks of the first two generations are denoted by u_i, d_i and the right-handed top quark by t.

Using this notation, our interpretation considers 15 dimension-six operators in the Warsaw basis [44, 45]:

- There are eight $q\bar{q}t\bar{t}$ operators with LL and RR chiral structures:

$$\begin{aligned}
O_{Qq}^{1,8} &= (\bar{Q}\gamma_\mu T^A Q)(\bar{q}_i\gamma^\mu T^A q_i), & O_{Qq}^{1,1} &= (\bar{Q}\gamma_\mu Q)(\bar{q}_i\gamma^\mu q_i),\\
O_{Qq}^{3,8} &= (\bar{Q}\gamma_\mu T^A \tau^I Q)(\bar{q}_i\gamma^\mu T^A \tau^I q_i), & O_{Qq}^{3,1} &= (\bar{Q}\gamma_\mu \tau^I Q)(\bar{q}_i\gamma^\mu \tau^I q_i),\\
O_{tu}^{8} &= (\bar{t}\gamma_\mu T^A t)(\bar{u}_i\gamma^\mu T^A u_i) & O_{tu}^{1} &= (\bar{t}\gamma_\mu t)(\bar{u}_i\gamma^\mu u_i)\\
O_{td}^{8} &= (\bar{t}\gamma^\mu T^A t)(\bar{d}_i\gamma_\mu T^A d_i) & O_{td}^{1} &= (\bar{t}\gamma_\mu t)(\bar{d}_i\gamma^\mu d_i)\,.
\end{aligned}$$

- There are six further $q\bar{q}t\bar{t}$ operators with LR structures:

$$\begin{aligned}
O_{Qu}^{8} &= (\bar{Q}\gamma_\mu T^A Q)(\bar{u}_i\gamma^\mu T^A u_i) & O_{Qu}^{1} &= (\bar{Q}\gamma_\mu Q)(\bar{u}_i\gamma^\mu u_i)\\
O_{Qd}^{8} &= (\bar{Q}\gamma_\mu T^A Q)(\bar{d}_i\gamma^\mu T^A d_i) & O_{Qd}^{1} &= (\bar{Q}\gamma_\mu Q)(\bar{d}_i\gamma^\mu d_i)\\
O_{tq}^{8} &= (\bar{t}\gamma^\mu T^A t)(\bar{q}_i\gamma_\mu T^A q_i) & O_{tq}^{1} &= (\bar{t}\gamma^\mu t)(\bar{q}_i\gamma_\mu q_i)\,.
\end{aligned}$$

- There is one tensor operator that modifies the top–gluon interaction:

$$O_{tG} = (\bar{t}\sigma^{\mu\nu}T^A t)\tilde{\varphi}G^A_{\mu\nu}.$$

The indices indicate the strong and weak structures: colour-singlet operators are indicated with (1) and colour-octet operators with (8), weak-singlet operators with (1) and weak-triplet operators with (3). Also, $T^A \equiv \lambda^A/2$ where λ^A are Gell-Mann matrices; τ^I represents Pauli matrices, $\tilde{\varphi}$ represents the Higgs doublet φ with the antisymmetric SU(2) tensor by $\epsilon = i\tau^2$ and $\tilde{\varphi} = \epsilon\varphi^*$. The CP-violating imaginary parts of operator coefficients are not considered.

The charge asymmetry is affected by a particular linear combination of operator coefficients [151–153]. This measurement is therefore complementary to cross-section measurements and very valuable in disentangling blind directions in global SMEFT fits [151].

The operators are implemented in the SMEFT@NLO UFO model [154] in the MadGraph5_aMC@NLO package [117]. The relation between the operator coefficients and the charge asymmetry is determined at NLO accuracy in the strong coupling constant and is parameterised with an analytic function [155]. If the 'positive' and 'negative' cross-sections are defined as $\sigma^+ = \sigma(\Delta|y_{t\bar{t}}| > 0)$ and $\sigma^- = \sigma(\Delta|y_{t\bar{t}}| < 0)$, respectively, they can be expressed as a function of the relevant operator coefficients:

$$\sigma^{\pm} = \sigma^{\pm}_{\text{SM}} + \sum_i \sigma^{\pm}_{1,i} \times C_i/\Lambda^2 + \sum_i \sigma^{\pm}_{2,i} \times C_i^2/\Lambda^4 + \sum_{i,j} \sigma^{\pm}_{3,i,j} \times C_i C_j/\Lambda^4$$

Fits with two different parameterisations are performed: one that retains only the *linear* terms proportional to Λ^{-2} due to the interference of the dimension-six operators with the SM, and a second *quadratic* parameterisation that also retains the dimension-six-squared terms proportional to Λ^{-4}. In the quadratic fit the cross-terms $C_i C_j$ involving two different operator coefficients are taken into account. The $\sigma^{\pm}_{\text{SM}}$ term in the parameterisation – determined at NLO accuracy with SMEFT@NLO [154] – is replaced by the NNLO prediction from Ref. [19].

Limits on individual Wilson coefficients are derived by χ^2 minimisation. Just one Wilson coefficient is varied, while the others are fixed to the SM prediction, i.e. zero. As an example, the 68% and 95% CL bounds on C^8_{tu}/Λ^2 from the $A_{\text{C}}^{t\bar{t}}$ measurement are shown in Figure 7. The different points correspond to the inclusive $A_{\text{C}}^{t\bar{t}}$ measurement, the individual bins of the differential $A_{\text{C}}^{t\bar{t}}$ measurement as a function of $m_{t\bar{t}}$, and the combined fit of the bins of the $A_{\text{C}}^{t\bar{t}}$ vs $m_{t\bar{t}}$ measurement. Limits derived from the LHC combination of charge asymmetry measurements at $\sqrt{s} = 8$ TeV and from the Tevatron combination of forward–backward asymmetry measurements in 1.96 TeV $p\bar{p}$ collisions are shown in the lower panel, for reference.

The nominal result, obtained with a linear parameterisation of the C^8_{tu}/Λ^2 dependence, is shown in blue. The result of the fit that also takes into account the Λ^{-4} term is shown in red. The central values returned by the fits are quite similar, but in many cases the 95% CL intervals differ considerably and Λ^{-4} terms are not negligible. The inclusive measurement, with an uncertainty of 0.15%, yields tight bounds: $-1.44 < C^8_{tu}/\Lambda^2 < 2.05$ TeV^{-2} at 95% CL in the linear fit. Despite the large dilution by gluon-initiated $t\bar{t}$ production at the LHC at $\sqrt{s} = 13$ TeV, these bounds based on a single measurement improve considerably on the limits derived from the LHC 8 TeV combination [41] and from the Tevatron combination [156].

The bounds from the differential measurements reflect the interplay between the sensitivity, which increases rapidly at higher $m_{t\bar{t}}$, and the uncertainty, which grows from 0.2%–0.3% in the lowest mass bin to 2.9% in the highest bin. For the linear fit, the tightest limit is obtained in the mass bin from 1 to 1.5 TeV.

The result labelled 'differential' combines all results of the differential measurement versus $m_{t\bar{t}}$ in a χ^2 minimisation. The covariance matrix that keeps track of bin-to-bin correlations in the differential result includes experimental uncertainties from the measurement and the uncertainties from the fixed-order prediction. The experimental covariance matrix includes the uncertainties from experimental and modelling uncertainties in the measurement, as returned by the unfolding procedure. The covariance matrix for the SM prediction includes the effect of different choices for the renormalisation and factorisation scales and of the difference between the LUXqed and NNPDF3.1 PDF sets. The covariance matrices due to experimental and theoretical uncertainties are added together. The differential analysis yields a tight set of 95% CL bounds. For example, the linear 95% CL bound on C^8_{tu}/Λ^2 improves from $[-1.44, 2.05]$ TeV^{-2} in the inclusive measurement to $[-0.28, 1.38]$ TeV^{-2}.

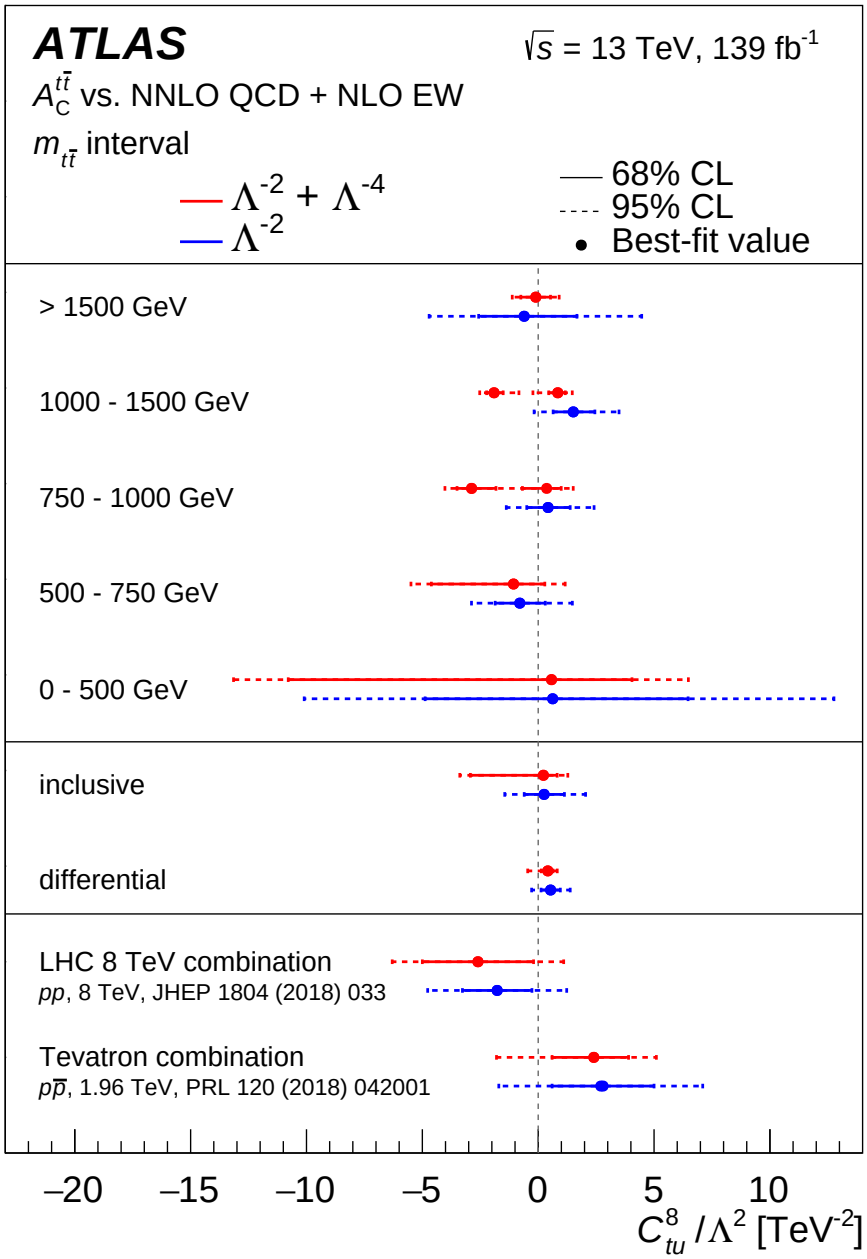

Figure 7: Individual 68% (solid line) and 95% (dashed line) CL limits on the Wilson coefficient C_{tu}^{8}/Λ^2 in the SMEFT. The bounds are derived from the charge asymmetry measurement presented in this paper, combining the single-lepton and dilepton channels. For the quadratic fit, two solutions were found by the χ^2 minimisation in some cases. The theory uncertainty corresponds to the NNLO QCD + NLO EW calculation. The impact of dimension-six operators is parameterised at NLO accuracy in QCD using the SMEFT@NLO package in MadGraph5_aMC@NLO. Bounds are also shown from the forward–backward asymmetry measurements in $\sqrt{s} = 1.96$ TeV $p\bar{p}$ collisions at the Tevatron and the charge asymmetry measurements in 8 TeV pp collisions in LHC Run 1.

The individual 68% CL and 95% CL bounds on the Wilson coefficients of all relevant $q\bar{q}t\bar{t}$ operators and C_{tG} obtained from the combination of $m_{t\bar{t}}$ differential results are presented in Figure 8. All intervals are also given in Table 10. The 95% CL bounds typically range from $\mathcal{O}(1\ \text{TeV}^{-2})$ to over $\mathcal{O}(10\ \text{TeV}^{-2})$. For the inclusive measurement, the linear fit yields tighter bounds on the Wilson coefficients for octet operators, which enter at tree level, than for the coefficients of singlet operators that only affect $t\bar{t}$ production at NLO [151]. The quadratic fit, however, provides tighter constraints for most of the singlet operators. The 95% CL bounds from the differential measurement are generally about a factor of two stronger than the bounds derived from the inclusive measurement, thanks to the rapidly increasing sensitivity at high $m_{t\bar{t}}$.

Compared to global fits of the top-quark sector [45, 151, 157] and fits including top, Higgs and EW data [155, 158] the bounds found in this analysis are of the same order of magnitude. Often, the bounds from the differential analysis are significantly tighter than the global bounds, indicating that inclusion of these results in future global fits can improve the global result, by disentangling some of the poorly constrained combinations of operator coefficients.

A further asymmetry measurement was proposed in Ref. [159]. The energy asymmetry in boosted $t\bar{t}$ production in association with an energetic jet provides complementary information that can eliminate a blind direction of the charge asymmetry measurement. Such a measurement was performed in $t\bar{t}j$ production by the ATLAS Collaboration [46].

For the energy asymmetry, the SM prediction was obtained from simulations of $t\bar{t}j$ production at NLO with MadGraph5_aMC@NLO+Pythia 8, while the impact of dimension-six operators is parameterised at LO accuracy in QCD using the SMEFT@NLO package in MadGraph5_aMC@NLO. The covariance matrix used in the χ^2 fit contains the experimental uncertainties as well as the statistical uncertainty of the Monte Carlo prediction and the theory uncertainty due to its scale dependence. The renormalisation and factorisation scales μ_r and μ_f are varied from their nominal values by factors of 2 and 0.5, yielding nine different pairs of scale values, and the effect of the scale uncertainty is assessed from the envelope of the resulting asymmetries.

Due to the extra jet in $t\bar{t}j$ production, the QCD structure of the energy asymmetry is not the same as for the charge asymmetry in $t\bar{t}$ production, so the two asymmetries probe different directions in chiral and colour space. This complementarity is illustrated in Figure 9, which shows the bounds from $m_{t\bar{t}}$ differential charge asymmetry measurements compared with the bounds from the energy asymmetry measurement. For colour-singlet operators with different quark chiralities (top row), the two asymmetries probe similar areas in the parameter space. For colour-octet operators with the same chirality scenarios (middle row), however, the shapes of the bounds look very different. In particular, the charge asymmetry leaves a blind direction in the $(C_{Qq}^{1,8}, C_{tq}^{8})$ plane (left panel), which is broken by the energy asymmetry due to operator interference with the QCD amplitude. The bottom row shows colour-singlet versus colour-octet operators with the same quark chiralities. Here, the different shapes of the bounds are due to the different colour-singlet and colour-octet contributions to $t\bar{t}$ and $t\bar{t}j$ production, which is probed with high sensitivity by the asymmetries. The EFT contributions include dimension-six-squared terms proportional to Λ^{-4} for both the charge asymmetry and energy asymmetry. A comparison for C_{tu}^{1} versus C_{tu}^{8} is not included, because the different sensitivity to colour-singlet and colour-octet operators has already been illustrated with C_{tq}^{1} versus C_{tq}^{8}, and the difference between L and R light quarks has been illustrated with $C_{Qq}^{1,1}$ versus C_{tu}^{1}.

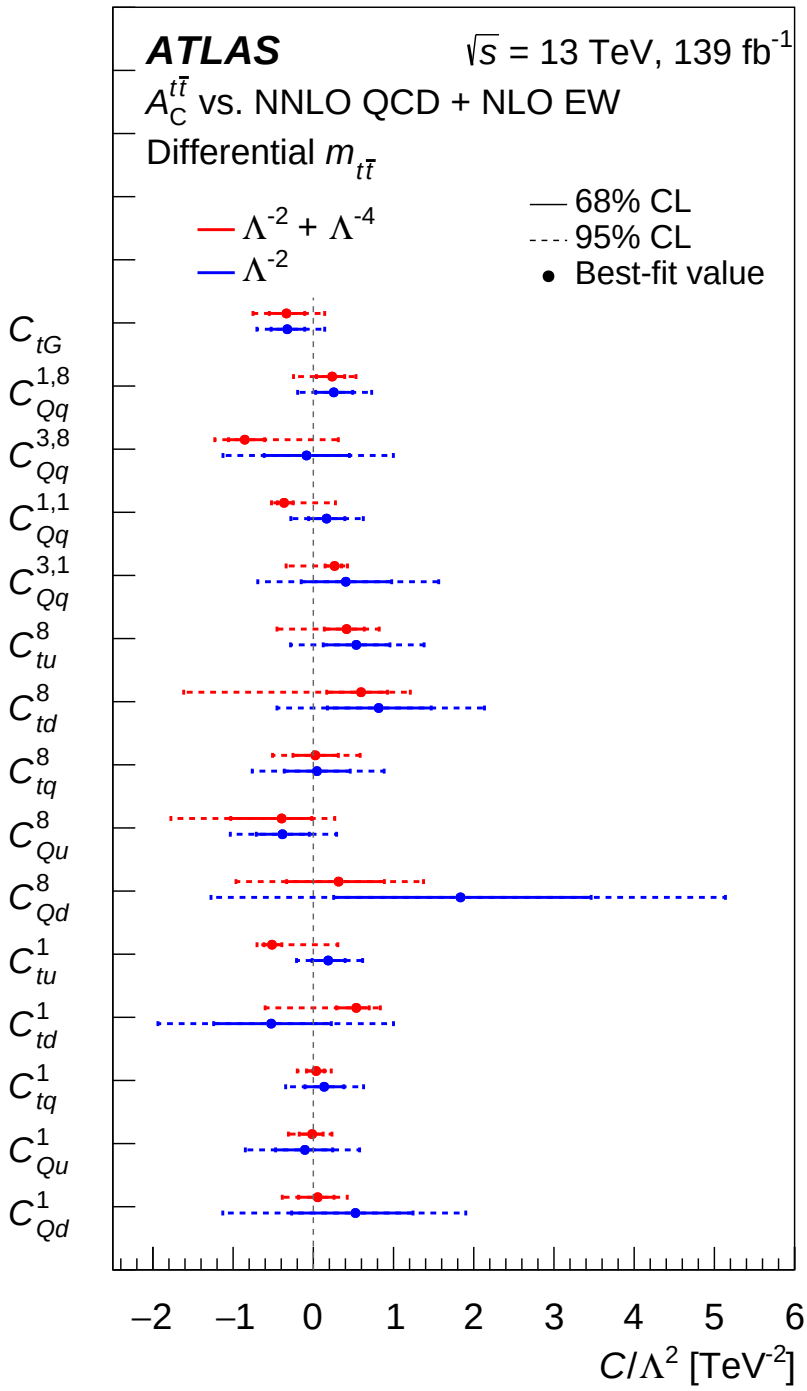

Figure 8: Individual 68% (solid line) and 95% (dashed line) CL limits on the Wilson coefficients C_i/Λ^2 in the SMEFT from the differential charge asymmetry measurements versus $m_{t\bar{t}}$. Only one Wilson coefficient is varied at a time while the others are kept at 0. The bounds are derived from the charge asymmetry measurement presented in this paper, combining the single-lepton and dilepton channels. The theory uncertainty corresponds to the NNLO QCD + NLO EW calculation. The impact of dimension-six operators is parameterised at NLO accuracy in QCD using the SMEFT@NLO package in MadGraph5_aMC@NLO.

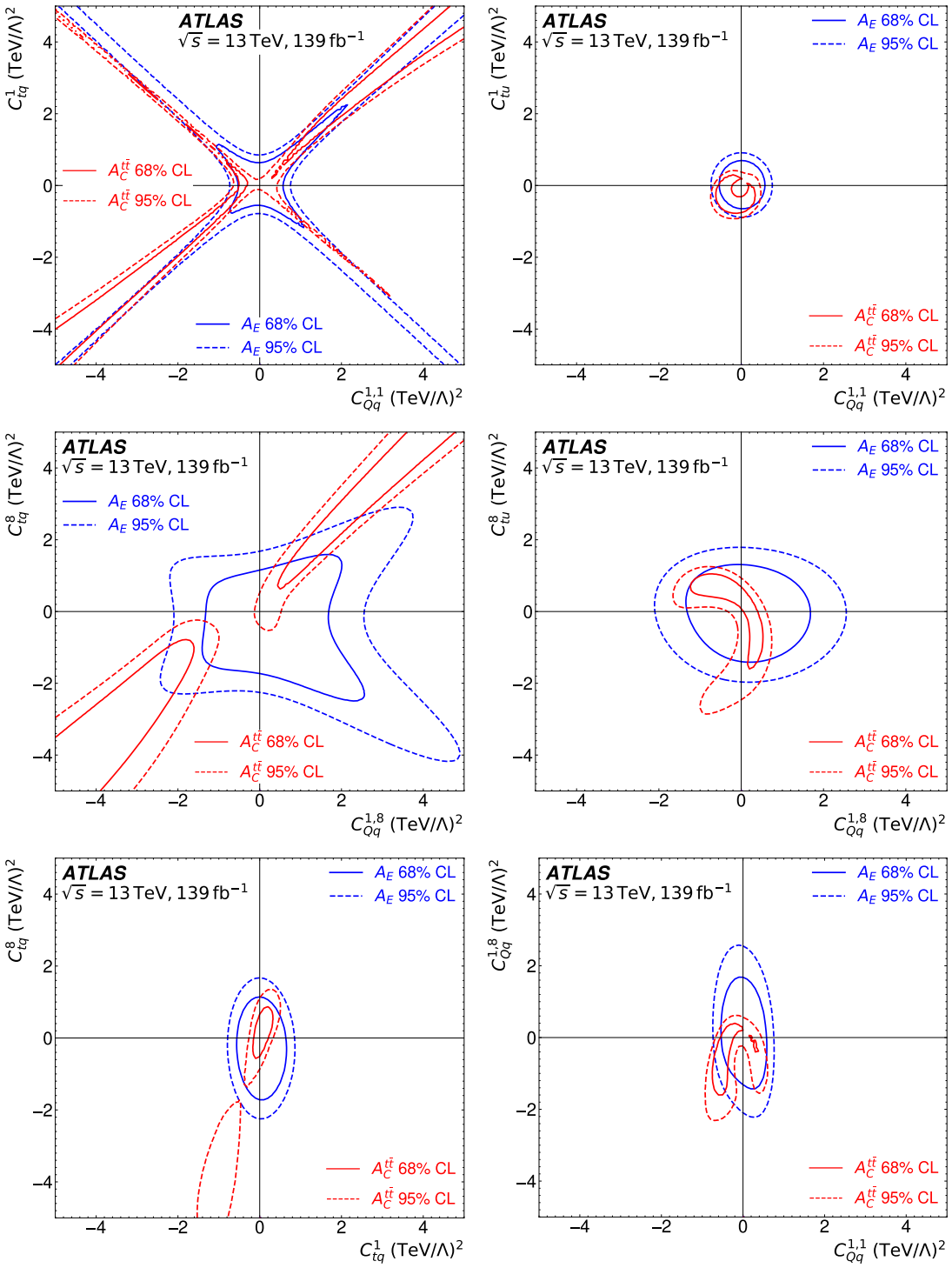

Figure 9: Bounds on Wilson coefficients from two-parameter fits of the energy asymmetry A_E (blue) and $A_C^{t\bar{t}}$ vs $m_{t\bar{t}}$ (red) measurements. The full and dashed lines show the 68% and 95% CL limits, respectively. The bounds are derived from a comparison of the measured asymmetries with the SMEFT predictions using the quadratic parameterisation. The SM prediction of A_E is obtained from simulations of $t\bar{t}j$ production at NLO with MadGraph5_aMC@NLO+Pythia 8, while the impact of dimension-six operators is parameterised at LO accuracy in QCD using the SMEFT@NLO package in MadGraph5_aMC@NLO. For $A_C^{t\bar{t}}$ the SM prediction is calculated up to NNLO QCD and NLO EW accuracy and the impact of the dimension-six operators is parameterised at NLO accuracy in QCD using the SMEFT@NLO package in MadGraph5_aMC@NLO.

Table 10: Individual 68% and 95% CL bounds on the relevant Wilson coefficients of the SM Effective Field Theory in units of TeV^{-2}. The bounds are derived from the charge asymmetry measurement presented in this paper, combining the single-lepton and dilepton channels. The upper block corresponds to the bounds derived from the inclusive measurement, the second block to the bounds from the differential charge asymmetry measurements versus $m_{t\bar{t}}$. In both cases, the experimental uncertainties are accounted for, in the form of the complete covariance matrix that keeps track of correlations between bins for the differential measurement. The theory uncertainty from the NNLO QCD + NLO EW calculation is included by explicitly varying the renormalisation and factorisation scales, or the parton distribution functions, in the calculation and registering the variations in the intervals.

Individual bounds (in units of TeV^{-2}) from the inclusive $A_C^{t\bar{t}}$ measurement.				
	Linear fit including terms $\propto \Lambda^{-2}$		*Quadratic* fit adding $(D6)^2$ terms $\propto \Lambda^{-4}$	
Operator coefficient	68% CL	95% CL	68% CL	95% CL
C_{tG}/Λ^2	$[-0.54, 0.37]$	$[-0.89, 1.03]$	$[-0.56, 0.37]$	$[-0.97, 0.99]$
$C_{Qq}^{1,8}/\Lambda^2$	$[-0.32, 0.61]$	$[-0.78, 1.10]$	$[-0.37, 0.51]$	$[-3.47, 0.84]$
$C_{Qq}^{3,8}/\Lambda^2$	$[-0.88, 1.63]$	$[-2.10, 2.94]$	$[-1.97, 0.90]$	$[-2.41, 1.33]$
$C_{Qq}^{1,1}/\Lambda^2$	$[-1.24, 2.29]$	$[-2.97, 4.13]$	$[-0.60, 0.48]$	$[-0.79, 0.67]$
$C_{Qq}^{3,1}/\Lambda^2$	$[-6.74, 3.73]$	$[-12.1, 8.99]$	$[-0.51, 0.57]$	$[-0.70, 0.75]$
C_{tu}^{8}/Λ^2	$[-0.60, 1.13]$	$[-1.44, 2.05]$	$[-2.93, 0.82]$	$[-3.38, 1.28]$
C_{td}^{8}/Λ^2	$[-0.97, 1.80]$	$[-2.30, 3.26]$	$[-4.34, 1.28]$	$[-5.05, 1.99]$
C_{tq}^{8}/Λ^2	$[-0.96, 0.54]$	$[-1.73, 1.29]$	$[-2.77, 0.45]$	$[-3.23, 0.93]$
C_{Qu}^{8}/Λ^2	$[-1.06, 0.59]$	$[-1.90, 1.41]$	$[-3.63, 0.51]$	$[-4.17, 1.06]$
C_{Qd}^{8}/Λ^2	$[-3.71, 2.08]$	$[-6.61, 5.02]$	$[-3.36, 1.29]$	$[-4.41, 2.35]$
C_{tu}^{1}/Λ^2	$[-0.81, 1.49]$	$[-1.93, 2.69]$	$[-0.80, 0.53]$	$[-1.02, 0.75]$
C_{td}^{1}/Λ^2	$[-17.6, 32.7]$	$[-41.8, 59.4]$	$[-0.98, 0.96]$	$[-1.32, 1.30]$
C_{tq}^{1}/Λ^2	$[-1.25, 2.31]$	$[-3.00, 4.16]$	$[-0.34, 0.47]$	$[-0.55, 0.68]$
C_{Qu}^{1}/Λ^2	$[-2.40, 4.40]$	$[-5.76, 7.92]$	$[-0.43, 0.53]$	$[-0.68, 0.78]$
C_{Qd}^{1}/Λ^2	$[-53.0, 88.0]$	$[-134, 152]$	$[-0.72, 0.74]$	$[-1.10, 1.12]$
Individual bounds (in units of TeV^{-2}) from the differential $A_C^{t\bar{t}}$ measurement versus $m_{t\bar{t}}$.				
	Linear fit including terms $\propto \Lambda^{-2}$		*Quadratic* fit adding $(D6)^2$ terms $\propto \Lambda^{-4}$	
Operator coefficient	68% CL	95% CL	68% CL	95% CL
C_{tG}/Λ^2	$[-0.53, -0.11]$	$[-0.70, 0.14]$	$[-0.55, -0.11]$	$[-0.75, 0.14]$
$C_{Qq}^{1,8}/\Lambda^2$	$[\ 0.03,\ 0.49]$	$[-0.20, 0.73]$	$[\ 0.04,\ 0.39]$	$[-0.25, 0.53]$
$C_{Qq}^{3,8}/\Lambda^2$	$[-0.61,\ 0.45]$	$[-1.13, 1.00]$	$[-1.06, -0.61]$	$[-1.23, 0.31]$
$C_{Qq}^{1,1}/\Lambda^2$	$[-0.06,\ 0.39]$	$[-0.28, 0.62]$	$[-0.45, -0.25]$	$[-0.52, 0.28]$
$C_{Qq}^{3,1}/\Lambda^2$	$[-0.15,\ 0.98]$	$[-0.69, 1.56]$	$[\ 0.15,\ 0.35]$	$[-0.34, 0.43]$
C_{tu}^{8}/Λ^2	$[\ 0.12,\ 0.96]$	$[-0.28, 1.38]$	$[\ 0.14,\ 0.63]$	$[-0.45, 0.82]$
C_{td}^{8}/Λ^2	$[\ 0.18,\ 1.47]$	$[-0.45, 2.13]$	$[\ 0.17,\ 0.92]$	$[-1.62, 1.21]$
C_{tq}^{8}/Λ^2	$[-0.36,\ 0.46]$	$[-0.76, 0.88]$	$[-0.25,\ 0.31]$	$[-0.51, 0.58]$
C_{Qu}^{8}/Λ^2	$[-0.71, -0.05]$	$[-1.03, 0.29]$	$[-1.03, -0.02]$	$[-1.78, 0.27]$
C_{Qd}^{8}/Λ^2	$[\ 0.25,\ 3.46]$	$[-1.28, 5.14]$	$[-0.33,\ 0.89]$	$[-0.96, 1.37]$
C_{tu}^{1}/Λ^2	$[-0.02,\ 0.40]$	$[-0.21, 0.61]$	$[-0.62, -0.39]$	$[-0.70, 0.31]$
C_{td}^{1}/Λ^2	$[-1.24,\ 0.22]$	$[-1.94, 1.00]$	$[\ 0.29,\ 0.70]$	$[-0.60, 0.84]$
C_{tq}^{1}/Λ^2	$[-0.10,\ 0.38]$	$[-0.35, 0.63]$	$[-0.08,\ 0.14]$	$[-0.20, 0.22]$
C_{Qu}^{1}/Λ^2	$[-0.47,\ 0.24]$	$[-0.85, 0.58]$	$[-0.18,\ 0.12]$	$[-0.31, 0.23]$
C_{Qd}^{1}/Λ^2	$[-0.27,\ 1.24]$	$[-1.13, 1.90]$	$[-0.19,\ 0.26]$	$[-0.39, 0.42]$

9 Conclusion

The charge asymmetry in top-quark pair production is measured in the single-lepton and dilepton decay channels using 139 fb^{-1} of $\sqrt{s}$ = 13 TeV proton–proton collision data collected by the ATLAS experiment at the LHC. A fully Bayesian unfolding method is used to correct for detector resolution and acceptance effects. The resolved and boosted topologies of the single-lepton channels are unfolded simultaneously with the same- and opposite-flavour dilepton channels.

Differential measurements are performed as a function of the invariant mass, transverse momentum and longitudinal boost of the $t\bar{t}$ system. In comparison with previous results obtained at 8 TeV, the differential variables benefit from a finer binning at larger values which are sensitive to possible enhancements of the charge asymmetry due to new-physics phenomena beyond the Standard Model. The leptonic charge asymmetry is measured inclusively and differentially as a function of invariant mass, transverse momentum and longitudinal boost of the dilepton pair. The results are compatible with the Standard Model predictions calculated at next-to-leading order in quantum chromodynamics and next-to-leading order in electroweak theory.

The asymmetry obtained in the inclusive measurement, combining the single-lepton and dilepton results, is $A_{\mathrm{C}} = 0.0068 \pm 0.0015$ (stat.+syst.). The result differs from zero by 4.7 standard deviations and thus provides strong evidence for charge asymmetry in $t\bar{t}$ production at the LHC. The precision of the combination is dominated by the lepton+jets channel, primarily due to a much smaller statistical uncertainty than in the dilepton channel. The inclusive and differential measurements are consistent with the Standard Model predictions calculated at next-to-next-to-leading order in quantum chromodynamics and next-to-leading order in electroweak theory.

The results are interpreted in the Standard Model Effective Field Theory. Individual limits on the Wilson coefficients related to two-light-quark–two-heavy-quark operators and to the operator that modifies the top–gluon interaction are derived from the inclusive charge asymmetry measurement and from the differential measurement versus $m_{t\bar{t}}$. The 95% CL bound on C_{tu}^{8}/Λ^2 from the inclusive $A_{\mathrm{C}}^{t\bar{t}}$ measurement improves considerably on the limits derived from the LHC 8 TeV combination and from the Tevatron A_{FB} combination. The combined bound on C_{tu}^{8}/Λ^2 from the $m_{t\bar{t}}$ differential measurement, $[-0.28, 1.38]$ using a linear fit, is more than a factor of two better than the bound derived from the inclusive measurement, due to the rapid increase in sensitivity with $m_{t\bar{t}}$. The charge asymmetry presented in this paper complements the energy asymmetry measured recently in $t\bar{t}j$ production by ATLAS, since the two observables probe different directions in chiral and colour space.

Appendix

A Ranking

A.1 $A_{\mathrm{C}}^{t\bar{t}}$ combination measurement

The ranking of the leading systematic uncertainties is summarised in Tables 11 and 12 for the $\beta_{z,t\bar{t}}$ and $p_{\mathrm{T},t\bar{t}}$ differential $A_{\mathrm{C}}^{t\bar{t}}$ combined measurements, respectively. Figures 10–16 show the ten highest-ranking nuisance parameters. Comparisons of pre-marginalisation and post-marginalisation ranking are presented together with the pulls and constraints of the ranked nuisance parameters obtained from data. In the figures, the γ_1, γ_2, γ_3 and γ_4 nuisance parameters correspond to $[-5,-x]$, $[-x,0]$, $[0,x]$ and $[x,5]$ $\Delta|y_{t\bar{t}}|$ bins, respectively, where x stands for $\Delta|y_{t\bar{t}}|$ bin edge.

Table 11: Impact of systematic uncertainties on the measurement of $A_{\mathrm{C}}^{t\bar{t}}$ vs $\beta_{z,t\bar{t}}$, grouped into categories. The impact of each category is obtained by summing the symmetrised ranking impact of the respective individual uncertainties in quadrature. The total uncertainty differs from the sum-in-quadrature of the groups due to post-marginalisation nuisance parameter correlations in the unfolding.

	Post-marg. (pre-marg.) impact ×100			
$\beta_{z,t\bar{t}}$ bin	0–0.3	0.3–0.6	0.6–0.8	0.8–1.0
$t\bar{t}$ modelling	0.18 (0.25)	0.12 (0.16)	0.11 (0.14)	0.23 (0.34)
$t\bar{t}$ normalisation (flat prior)	0.07	0.05	0.04	0.07
Background modelling	0.15 (0.18)	0.07 (0.08)	0.07 (0.07)	0.12 (0.13)
Monte Carlo statistics	0.19	0.15	0.12	0.12
Small-R JES	0.15 (0.18)	0.10 (0.11)	0.09 (0.10)	0.10 (0.14)
Small-R JER	0.10 (0.16)	0.06 (0.09)	0.07 (0.10)	0.12 (0.17)
Large-R JES, JER	0.05 (0.05)	0.02 (0.03)	0.01 (0.02)	0.02 (0.03)
Leptons, $E_{\mathrm{T}}^{\mathrm{miss}}$	0.03 (0.04)	0.03 (0.04)	0.05 (0.06)	0.06 (0.08)
b-tagging eff.	0.03 (0.03)	0.02 (0.02)	0.02 (0.02)	0.03 (0.03)
Pile-up, JVT, luminosity	0.01 (0.01)	0.01 (0.01)	0.02 (0.02)	0.01 (0.01)
Statistical uncertainty	0.39	0.29	0.27	0.24
Total uncertainty	0.52	0.37	0.34	0.39

Table 12: Impact of systematic uncertainties on the measurement of $A_C^{t\bar{t}}$ vs $p_{T,t\bar{t}}$, grouped into categories. The impact of each category is obtained by summing the symmetrised ranking impact of the respective individual uncertainties in quadrature. The total uncertainty differs from the sum-in-quadrature of the groups due to post-marginalisation nuisance parameter correlations in the unfolding.

	Post-marg. (pre-marg.) impact ×100		
$p_{T,t\bar{t}}$ bin [GeV]	0–30	30–120	> 120
$t\bar{t}$ modelling	0.13 (0.19)	0.11 (0.16)	0.40 (0.57)
$t\bar{t}$ normalisation (flat prior)	0.03	0.05	0.12
Background modelling	0.11 (0.12)	0.12 (0.13)	0.14 (0.16)
Monte Carlo statistics	0.15	0.13	0.19
Small-R JES	0.09 (0.10)	0.08 (0.09)	0.16 (0.18)
Small-R JER	0.08 (0.12)	0.08 (0.11)	0.13 (0.20)
Large-R JES, JER	0.02 (0.03)	0.02 (0.03)	0.05 (0.07)
Leptons, E_T^{miss}	0.12 (0.14)	0.05 (0.07)	0.08 (0.08)
b-tagging eff.	0.03 (0.03)	0.03 (0.03)	0.04 (0.04)
Pile-up, JVT, luminosity	0.01 (0.01)	0.02 (0.02)	0.03 (0.03)
Statistical uncertainty	0.32	0.26	0.44
Total uncertainty	0.41	0.37	0.65

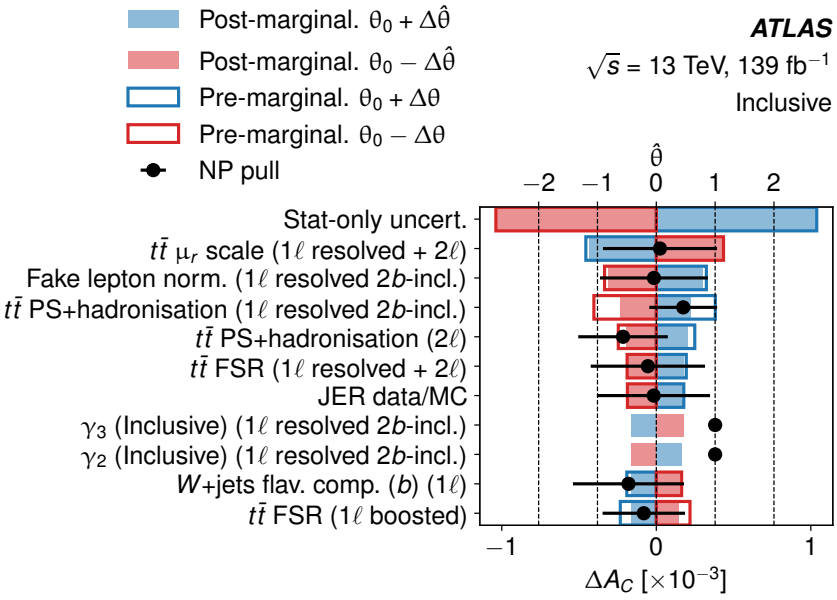

(a) Inclusive

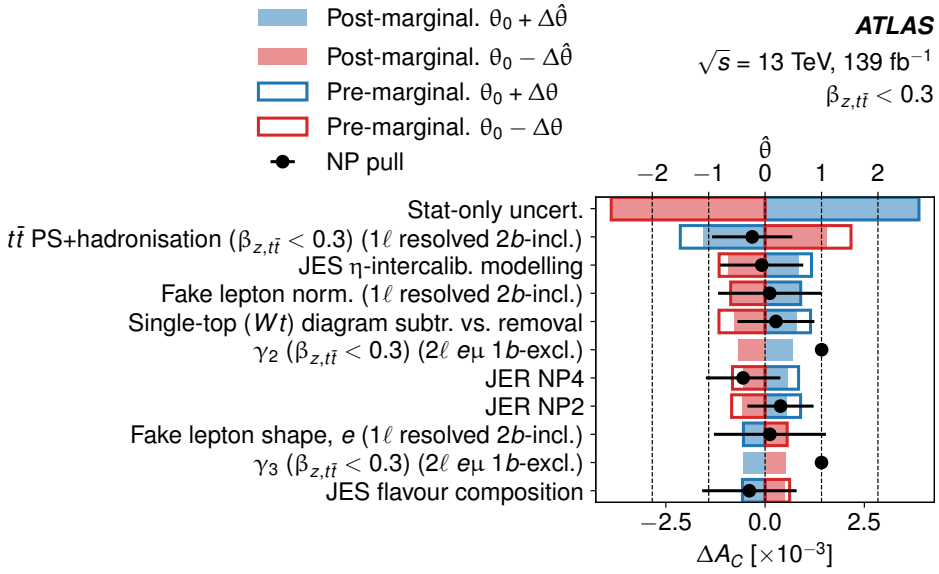

(b) $0.0 < \beta_{z,t\bar{t}} < 0.3$

Figure 10: Ranking of the systematic uncertainties with marginalisation (a) for the inclusive A_C measurement and (b) for $\beta_{z,t\bar{t}} \in [0.0, 0.3]$. Only the ten highest-ranking uncertainties are shown, ordered according to their post-marginalisation ranking, which considers the constraining power of the marginalisation for the data. The red and blue bars show the effect on unfolded A_C of downward and upward variation of the systematic uncertainty, respectively. The points show the pulls and constraints of the ranked NPs obtained from data.

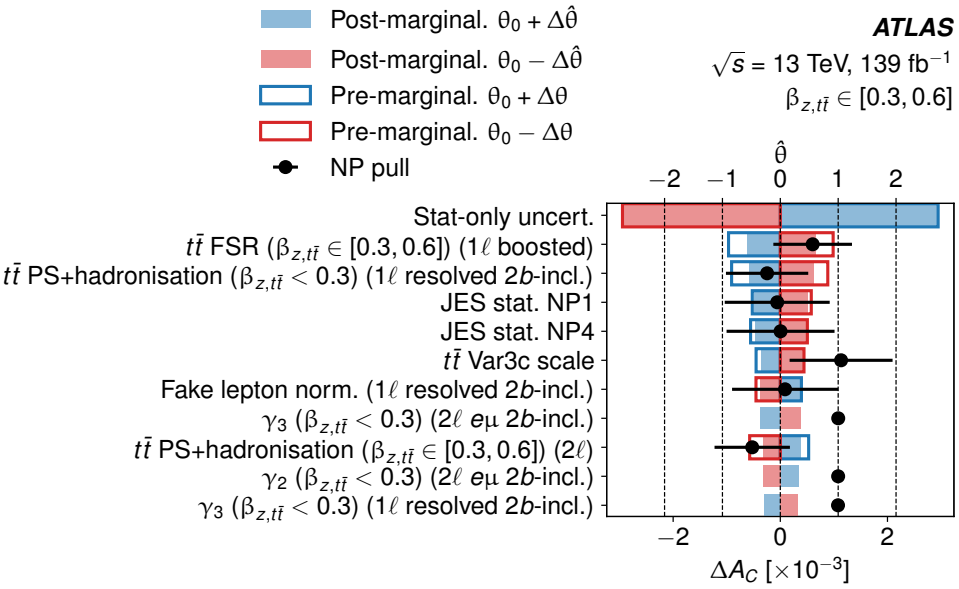

(a) $0.3 < \beta_{z,t\bar{t}} < 0.6$

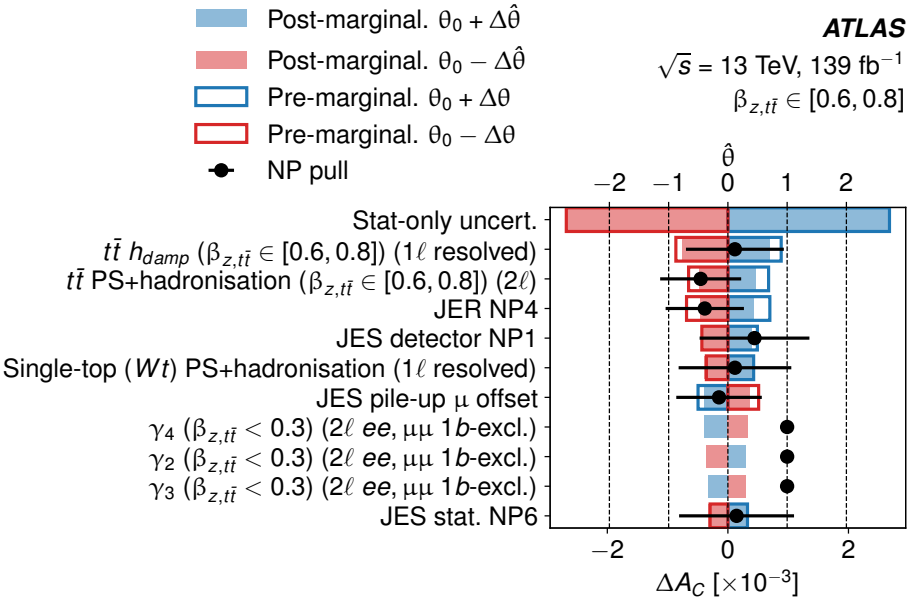

(b) $0.6 < \beta_{z,t\bar{t}} < 0.8$

Figure 11: Ranking of the systematic uncertainties with marginalisation (a) for $\beta_{z,t\bar{t}} \in [0.3, 0.6]$ and (b) for $\beta_{z,t\bar{t}} \in [0.6, 0.8]$. Only the ten highest-ranking uncertainties are shown, ordered according to their post-marginalisation ranking, which considers the constraining power of the marginalisation for the data. The red and blue bars show the effect on unfolded A_C of downward and upward variation of the systematic uncertainty, respectively. The points show the pulls and constraints of the ranked NPs obtained from data.

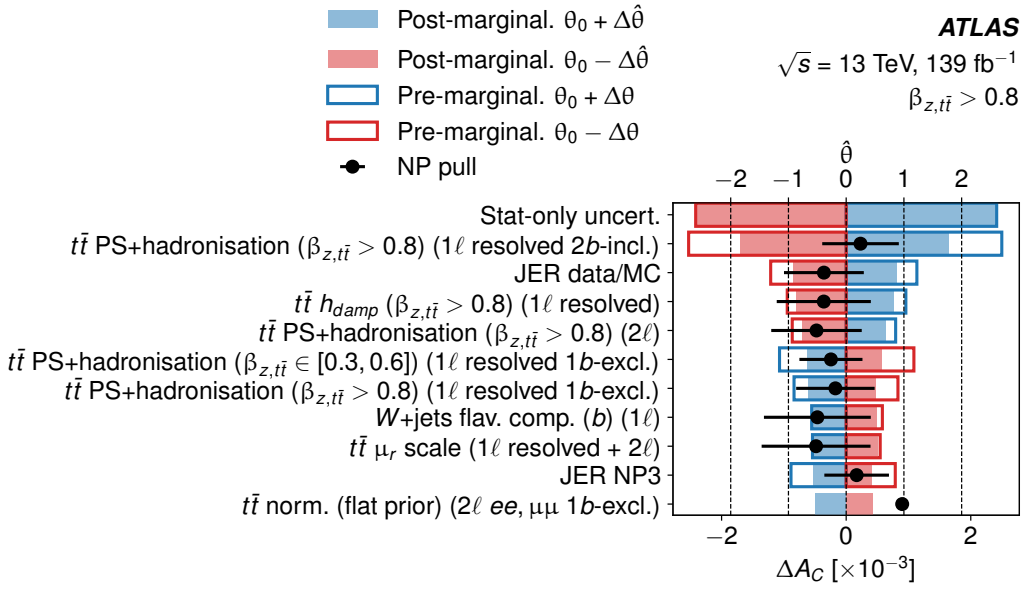

(a) $0.8 < \beta_{z,t\bar{t}} < 1.0$

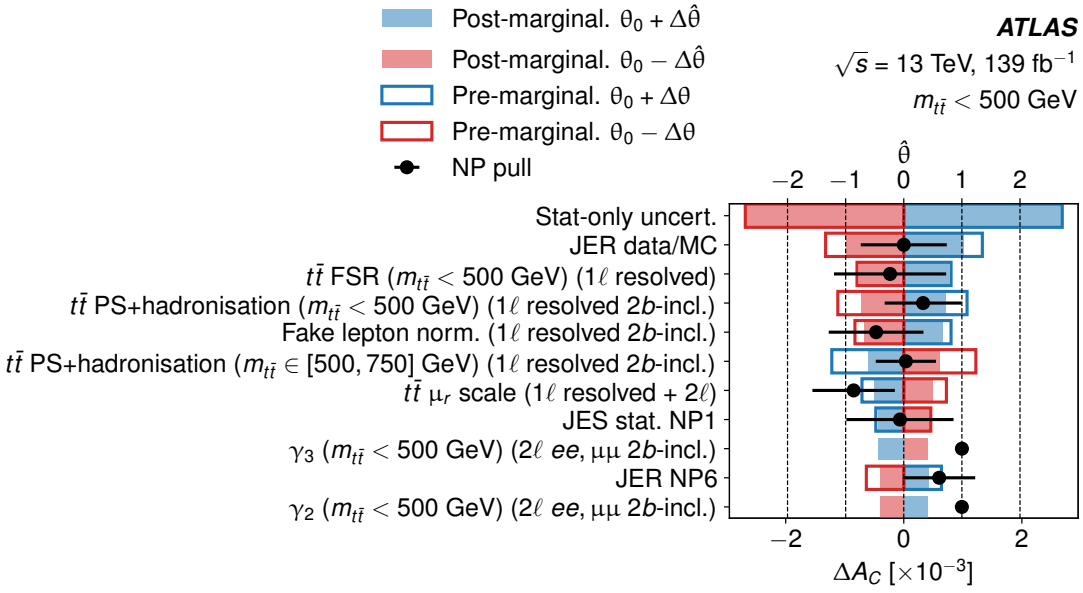

(b) $m_{t\bar{t}} < 500$ GeV

Figure 12: Ranking of the systematic uncertainties with marginalisation (a) for $\beta_{z,t\bar{t}} \in [0.8, 1.0]$ and (b) for $m_{t\bar{t}} \in [0, 500]$ GeV. Only the ten highest-ranking uncertainties are shown, ordered according to their post-marginalisation ranking, which considers the constraining power of the marginalisation for the data. The red and blue bars show the effect on unfolded A_C of downward and upward variation of the systematic uncertainty, respectively. The points show the pulls and constraints of the ranked NPs obtained from data.

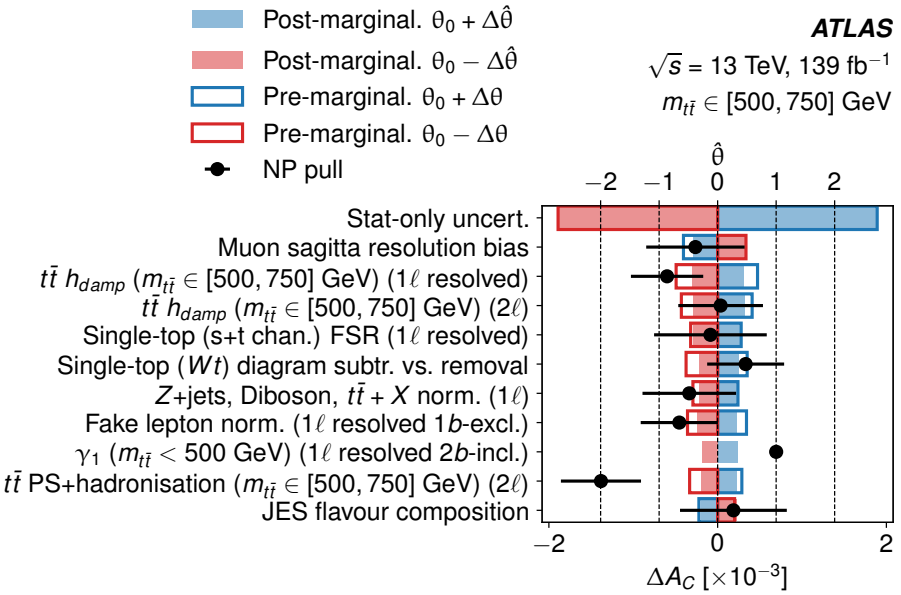

(a) $500 < m_{t\bar{t}} < 750$ GeV

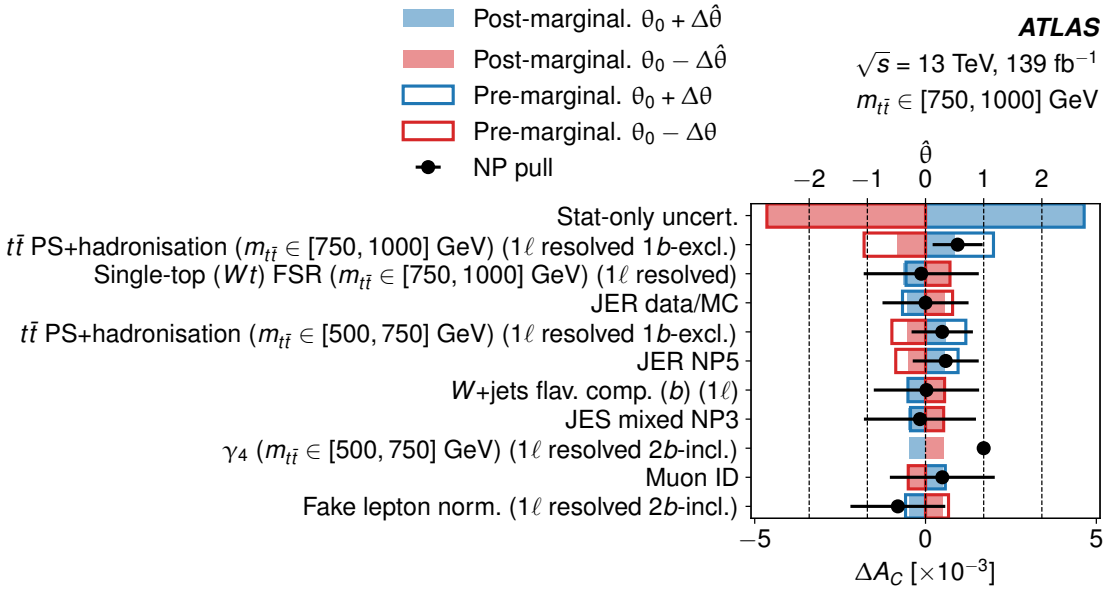

(b) $750 < m_{t\bar{t}} < 1000$ GeV

Figure 13: Ranking of the systematic uncertainties with marginalisation (a) for $m_{t\bar{t}} \in [500, 750]$ GeV and (b) for $m_{t\bar{t}} \in [750, 1000]$ GeV. Only the ten highest-ranking uncertainties are shown, ordered according to their post-marginalisation ranking, which considers the constraining power of the marginalisation for the data. The red and blue bars show the effect on unfolded A_C of downward and upward variation of the systematic uncertainty, respectively. The points show the pulls and constraints of the ranked NPs obtained from data.

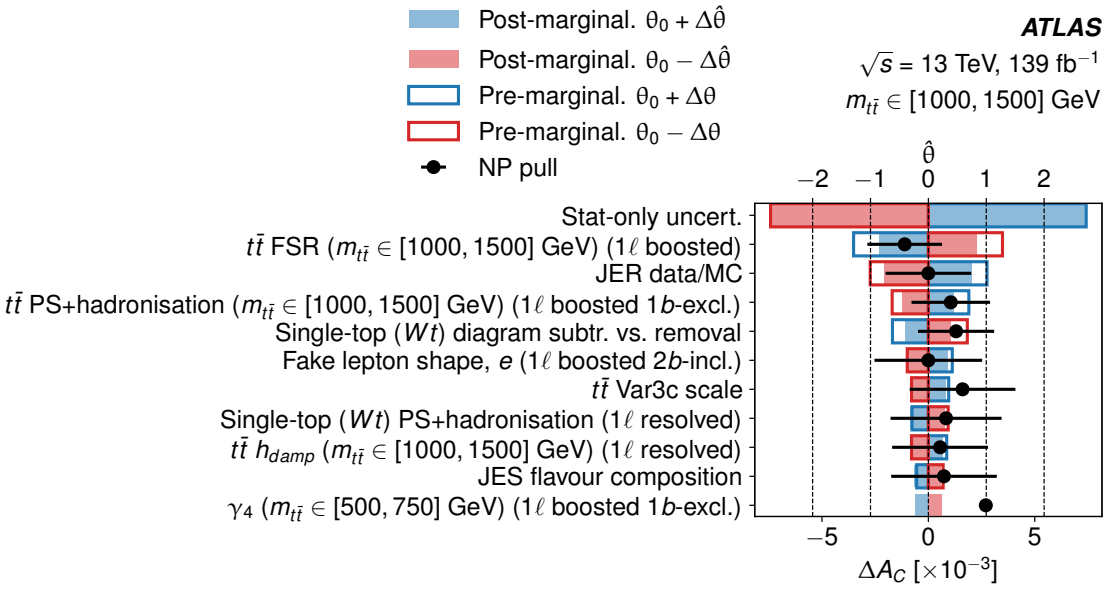

(a) $1000 < m_{t\bar{t}} < 1500$ GeV

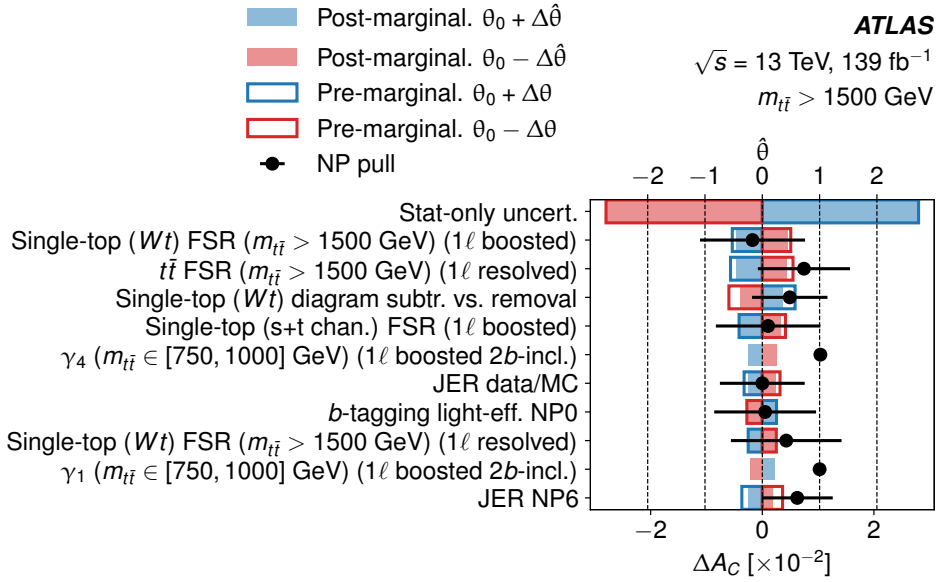

(b) $m_{t\bar{t}} > 1500$ GeV

Figure 14: Ranking of the systematic uncertainties with marginalisation (a) for $m_{t\bar{t}} \in [1000, 1500]$ GeV and (b) for $m_{t\bar{t}} > 1500$ GeV. Only the ten highest-ranking uncertainties are shown, ordered according to their post-marginalisation ranking, which considers the constraining power of the marginalisation for the data. The red and blue bars show the effect on unfolded A_C of downward and upward variation of the systematic uncertainty, respectively. The points show the pulls and constraints of the ranked NPs obtained from data.

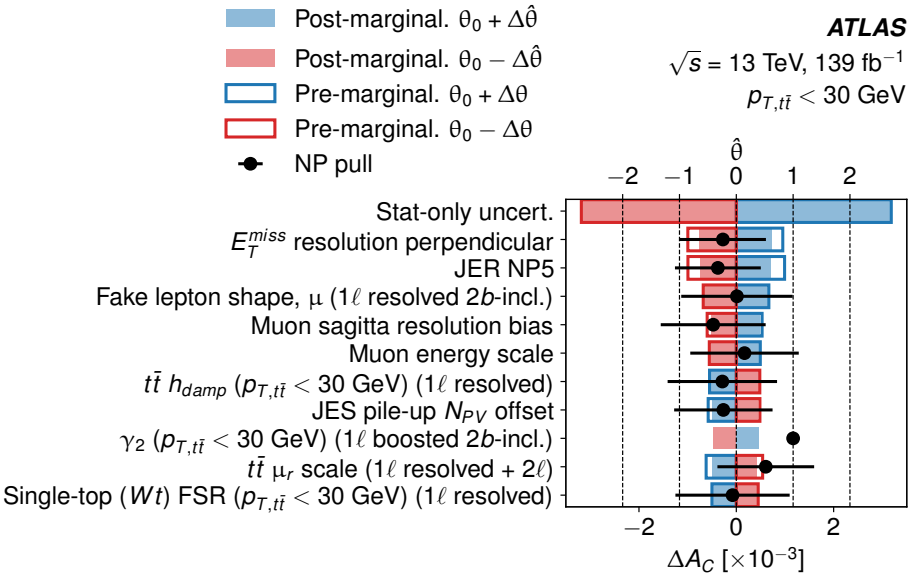

(a) $p_{\mathrm{T},t\bar{t}} < 30$ GeV

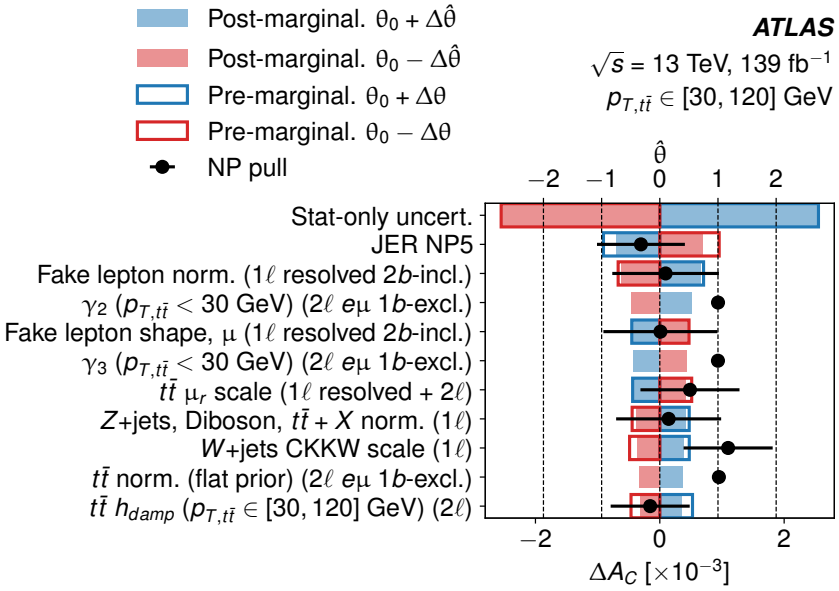

(b) $30 < p_{\mathrm{T},t\bar{t}} < 120$ GeV

Figure 15: Ranking of the systematic uncertainties with marginalisation (a) for $p_{\mathrm{T},t\bar{t}} \in [0, 30]$ GeV and (b) for $p_{\mathrm{T},t\bar{t}} \in [30, 120]$ GeV. Only the ten highest-ranking uncertainties are shown, ordered according to their post-marginalisation ranking, which considers the constraining power of the marginalisation for the data. The red and blue bars show the effect on unfolded A_{C} of downward and upward variation of the systematic uncertainty, respectively. The points show the pulls and constraints of the ranked NPs obtained from data.

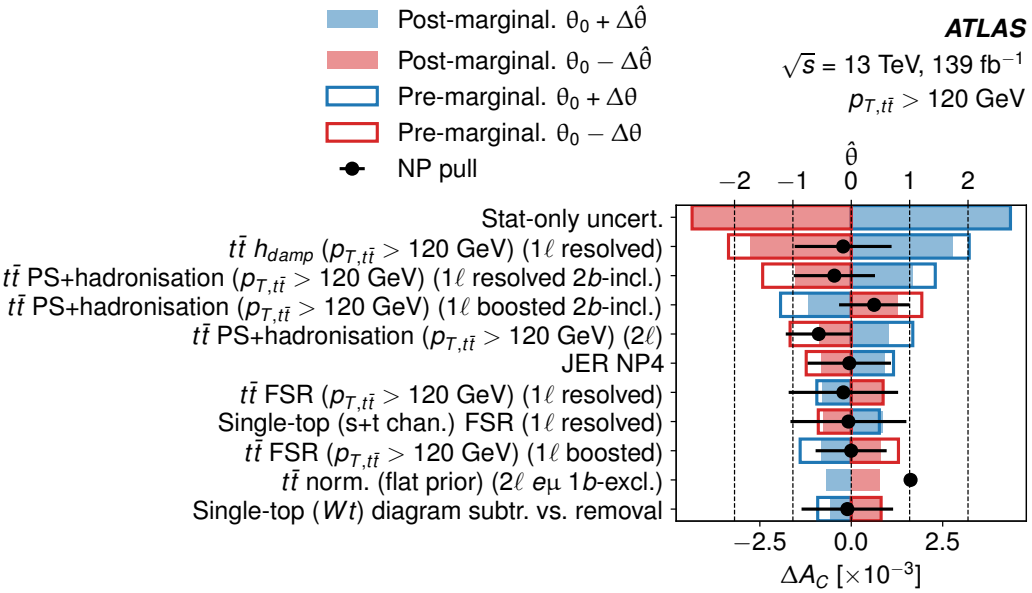

(a) $p_{T,t\bar{t}} > 120$ GeV

Figure 16: Ranking of the systematic uncertainties with marginalisation for $p_{T,t\bar{t}} > 120$ GeV. Only the ten highest-ranking uncertainties are shown, ordered according to their post-marginalisation ranking, which considers the constraining power of the marginalisation for the data. The red and blue bars show the effect on unfolded A_C of downward and upward variation of the systematic uncertainty, respectively. The points show the pulls and constraints of the ranked NPs obtained from data.

A.2 $A_C^{t\bar{t}}$ measurement

The ranking of the leading systematic uncertainties is summarised in Tables 13 and 14 for the $\beta_{z,t\bar{t}}$ and $p_{T,t\bar{t}}$ differential $A_C^{t\bar{t}}$ combined measurements, respectively. Figures 17–22 show the ten highest-ranking nuisance parameters. Comparisons of pre-marginalisation and post-marginalisation ranking are presented together with the pulls and constraints of the ranked nuisance parameters obtained from data. In the figures, the γ_1, γ_2, γ_3 and γ_4 nuisance parameters correspond to $[-2.5, -x]$, $[-x, 0]$, $[0, x]$ and $[x, 2.5]$ $\Delta|\eta_{t\bar{t}}|$ bins, respectively, where x stands for $\Delta|\eta_{t\bar{t}}|$ bin edge.

Table 13: Impact of systematic uncertainties on the measurement of $A_C^{\ell\bar{\ell}}$ vs $\beta_{z,\ell\bar{\ell}}$, grouped into categories. The impact of each category is obtained by summing the symmetrised ranking impact of the respective individual uncertainties in quadrature. The total uncertainty differs from the sum-in-quadrature of the groups due to post-marginalisation nuisance parameter correlations in the unfolding.

	Post-marg. (pre-marg.) impact ×100				
$\beta_{z,\ell\bar{\ell}}$ bin	0–0.3		0.3–0.6	0.6–0.8	0.8–1.0
$t\bar{t}$ modelling	0.04	(0.04)	0.37 (0.41)	0.27 (0.32)	0.09 (0.10)
$t\bar{t}$ normalisation (flat prior)	0.03		0.05	0.02	0.05
Background modelling	0.04	(0.05)	0.05 (0.06)	0.06 (0.07)	0.02 (0.03)
Monte Carlo statistics	0.06		0.07	0.11	0.07
Small-R JES	0.01	(0.01)	0.02 (0.02)	0.06 (0.07)	0.02 (0.02)
Small-R JER	0.03	(0.03)	0.07 (0.08)	0.04 (0.05)	0.05 (0.06)
Leptons, E_T^{miss}	0.02	(0.02)	0.02 (0.01)	0.02 (0.02)	0.01 (0.01)
b-tagging eff.	0.01	(0.01)	0.01 (0.01)	0.01 (0.01)	0.01 (0.01)
Pile-up, JVT, luminosity	<0.01	(<0.01)	0.01 (0.01)	0.02 (0.02)	0.01 (0.01)
Statistical uncertainty	0.28		0.24	0.26	0.28
Total uncertainty	0.29		0.49	0.45	0.31

Table 14: Impact of systematic uncertainties on the measurement of $A_C^{\ell\bar{\ell}}$ vs $p_{T,\ell\bar{\ell}}$, grouped into categories. The impact of each category is obtained by summing the symmetrised ranking impact of the respective individual uncertainties in quadrature. The total uncertainty differs from the sum-in-quadrature of the groups due to post-marginalisation nuisance parameter correlations in the unfolding.

	Post-marg. (pre-marg.) impact ×100		
$p_{T,\ell\bar{\ell}}$ bin [GeV]	0–20	20–70	> 70
$t\bar{t}$ modelling	0.19 (0.23)	0.24 (0.26)	0.16 (0.18)
$t\bar{t}$ normalisation (flat prior)	0.05	0.03	0.05
Background modelling	0.06 (0.07)	0.03 (0.04)	0.02 (0.03)
Monte Carlo statistics	0.18	0.06	0.05
Small-R JES	0.03 (0.03)	0.02 (0.03)	0.02 (0.02)
Small-R JER	0.05 (0.06)	0.06 (0.06)	0.03 (0.04)
Leptons, E_T^{miss}	0.04 (0.04)	0.03 (0.03)	0.01 (0.01)
b-tagging eff.	0.05 (0.05)	0.01 (0.01)	<0.01 (0.01)
Pile-up, JVT, luminosity	0.04 (0.04)	0.01 (0.01)	0.01 (0.01)
Statistical uncertainty	0.63	0.20	0.18
Total uncertainty	0.70	0.34	0.27

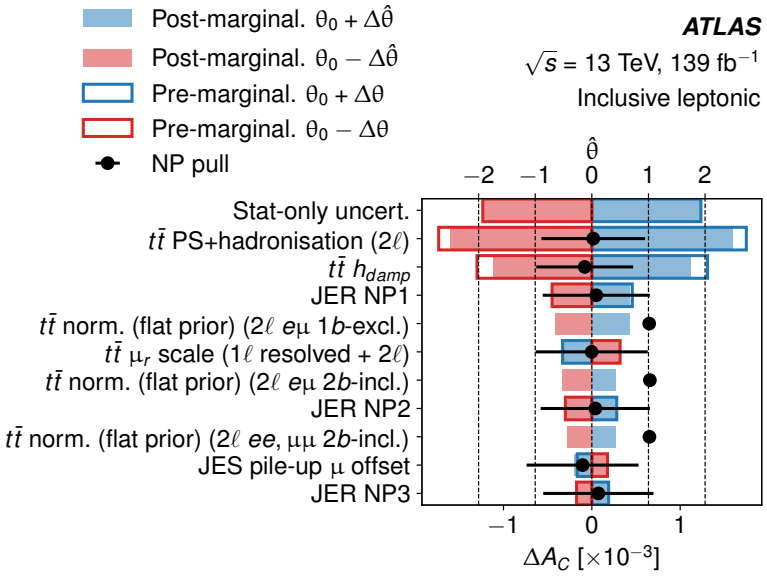

(a) Inclusive

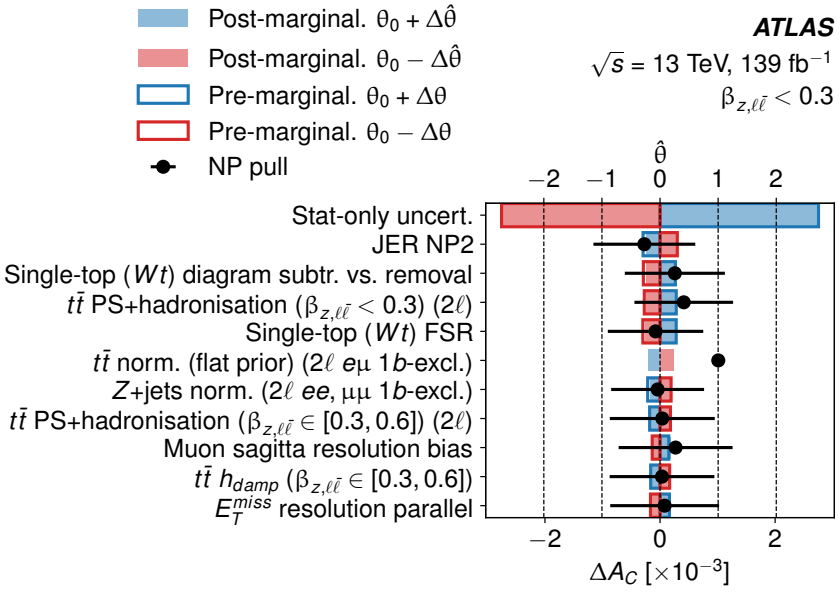

(b) $0.0 < \beta_{z,\ell\bar{\ell}} < 0.3$

Figure 17: Ranking of the systematic uncertainties with marginalisation (a) for the inclusive A_C measurement and (b) for $\beta_{z,\ell\bar{\ell}} \in [0.0, 0.3]$. Only the ten highest-ranking uncertainties are shown, ordered according to their post-marginalisation ranking, which considers the constraining power of the marginalisation for the data. The red and blue bars show the effect on unfolded A_C of downward and upward variation of the systematic uncertainty, respectively. The points show the pulls and constraints of the ranked NPs obtained from data.

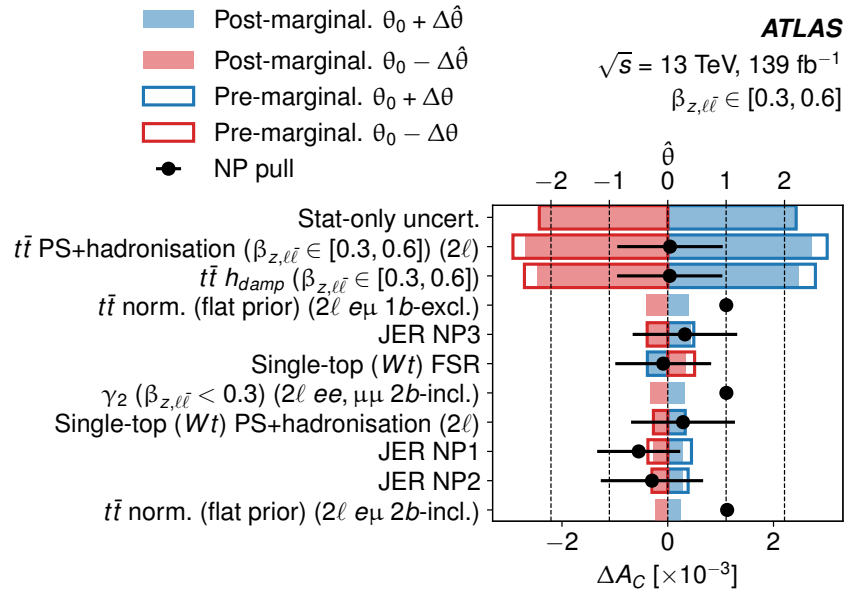

(a) $0.3 < \beta_{z,\ell\bar{\ell}} < 0.6$

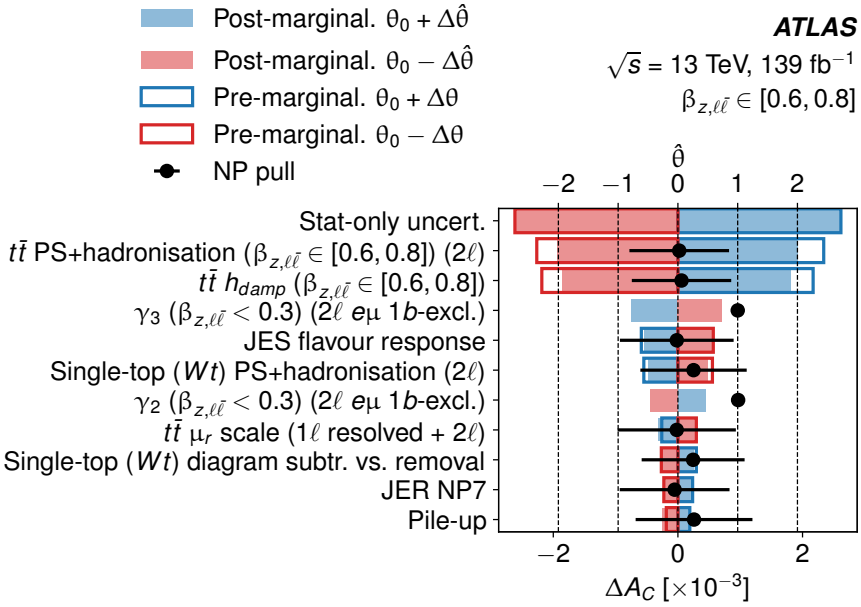

(b) $0.6 < \beta_{z,\ell\bar{\ell}} < 0.8$

Figure 18: Ranking of the systematic uncertainties with marginalisation (a) for $\beta_{z,\ell\bar{\ell}} \in [0.3, 0.6]$ and (b) for $\beta_{z,\ell\bar{\ell}} \in [0.6, 0.8]$. Only the ten highest-ranking uncertainties are shown, ordered according to their post-marginalisation ranking, which considers the constraining power of the marginalisation for the data. The red and blue bars show the effect on unfolded A_C of downward and upward variation of the systematic uncertainty, respectively. The points show the pulls and constraints of the ranked NPs obtained from data.

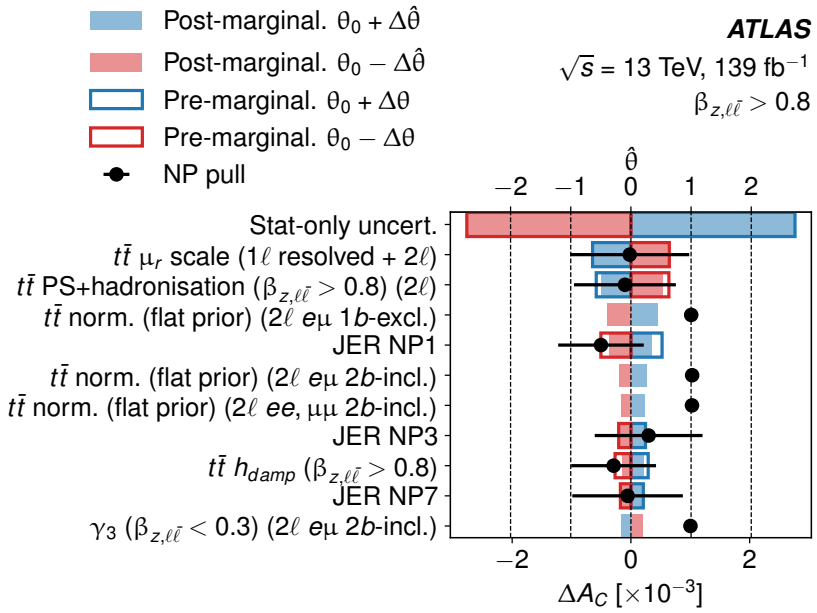

(a) $\beta_{z,\ell\bar{\ell}} > 0.8$

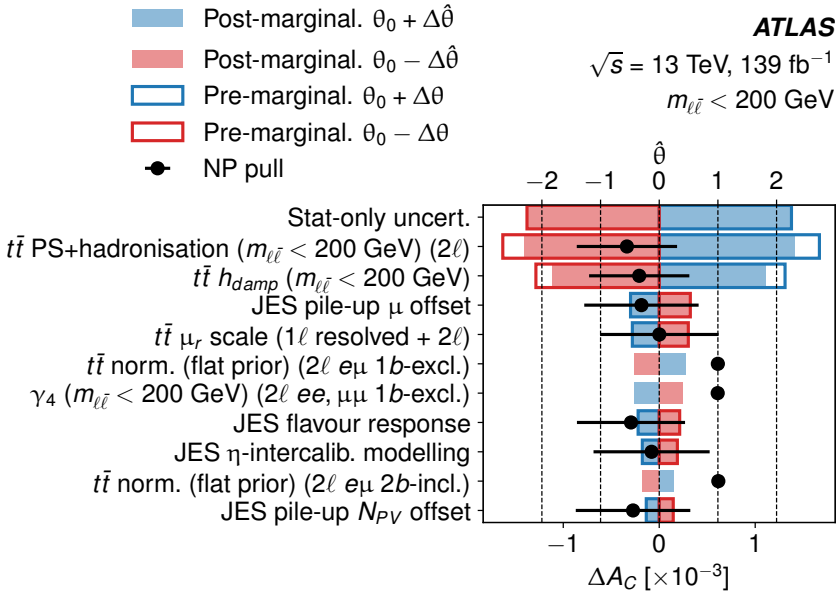

(b) $m_{\ell\bar{\ell}} < 200$ GeV

Figure 19: Ranking of the systematic uncertainties with marginalisation (a) for $\beta_{z,\ell\bar{\ell}} > 0.8$ and (b) for $m_{\ell\bar{\ell}} \in [0, 200]$ GeV. Only the ten highest-ranking uncertainties are shown, ordered according to their post-marginalisation ranking, which considers the constraining power of the marginalisation for the data. The red and blue bars show the effect on unfolded A_C of downward and upward variation of the systematic uncertainty, respectively. The points show the pulls and constraints of the ranked NPs obtained from data.

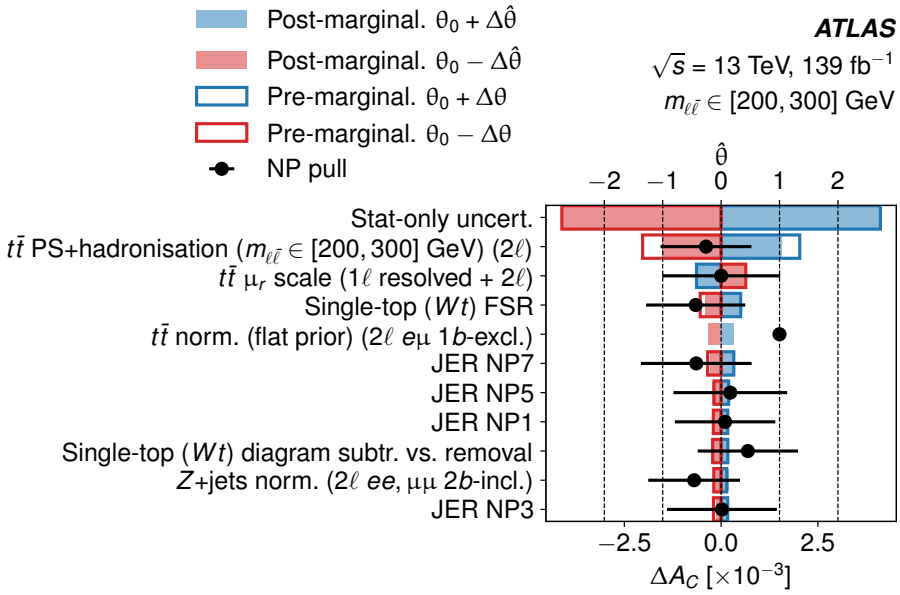

(a) $200 < m_{\ell\bar{\ell}} < 300$ GeV

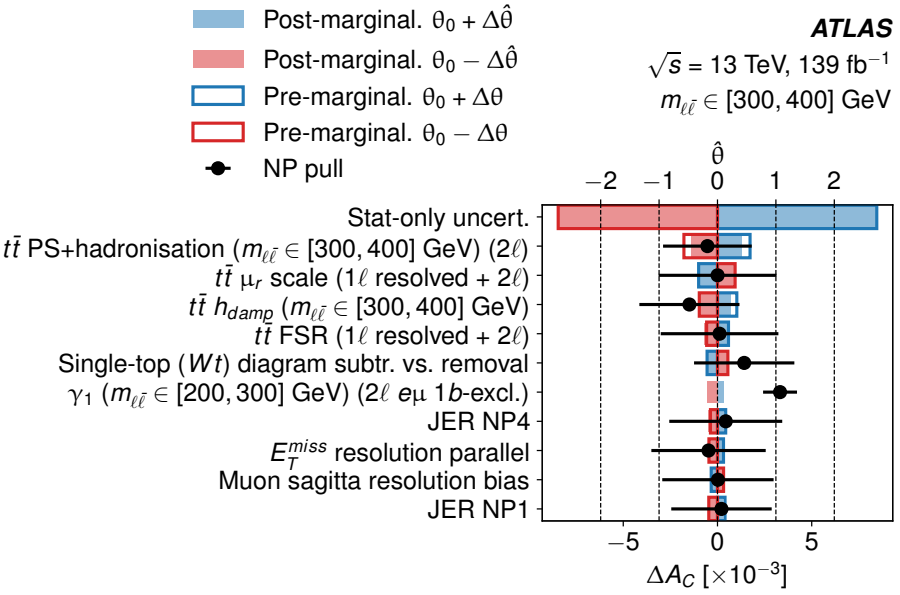

(b) $300 < m_{\ell\bar{\ell}} < 400$ GeV

Figure 20: Ranking of the systematic uncertainties with marginalisation (a) for $m_{\ell\bar{\ell}} \in [200, 300]$ GeV and (b) for $m_{\ell\bar{\ell}} \in [300, 400]$ GeV. Only the ten highest-ranking uncertainties are shown, ordered according to their post-marginalisation ranking, which considers the constraining power of the marginalisation for the data. The red and blue bars show the effect on unfolded A_C of downward and upward variation of the systematic uncertainty, respectively. The points show the pulls and constraints of the ranked NPs obtained from data.

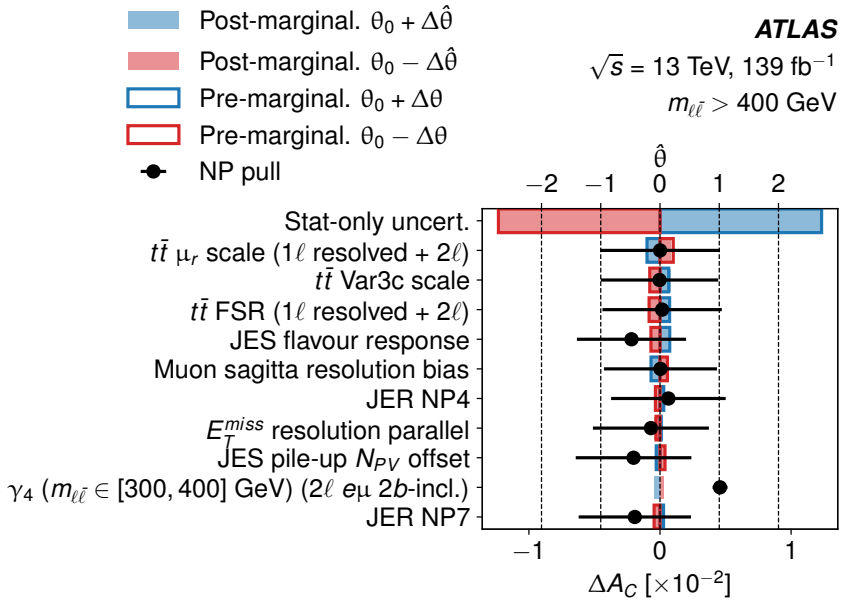

(a) $m_{\ell\bar{\ell}} > 400$ GeV

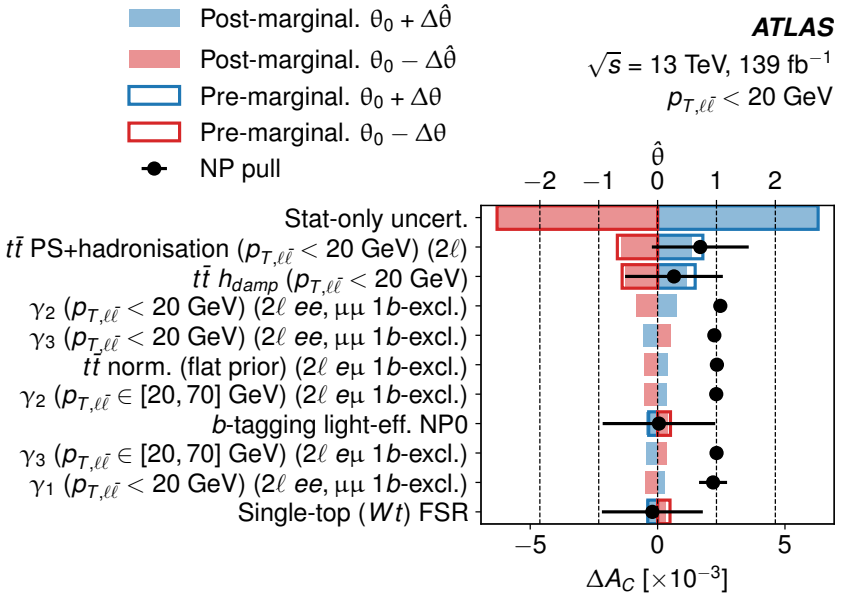

(b) $p_{T,\ell\bar{\ell}} < 20$ GeV

Figure 21: Ranking of the systematic uncertainties with marginalisation (a) for $m_{\ell\bar{\ell}} > 400$ GeV and (b) for $p_{T,\ell\bar{\ell}} < 20$ GeV. Only the ten highest-ranking uncertainties are shown, ordered according to their post-marginalisation ranking, which considers the constraining power of the marginalisation for the data. The red and blue bars show the effect on unfolded A_C of downward and upward variation of the systematic uncertainty, respectively. The points show the pulls and constraints of the ranked NPs obtained from data.

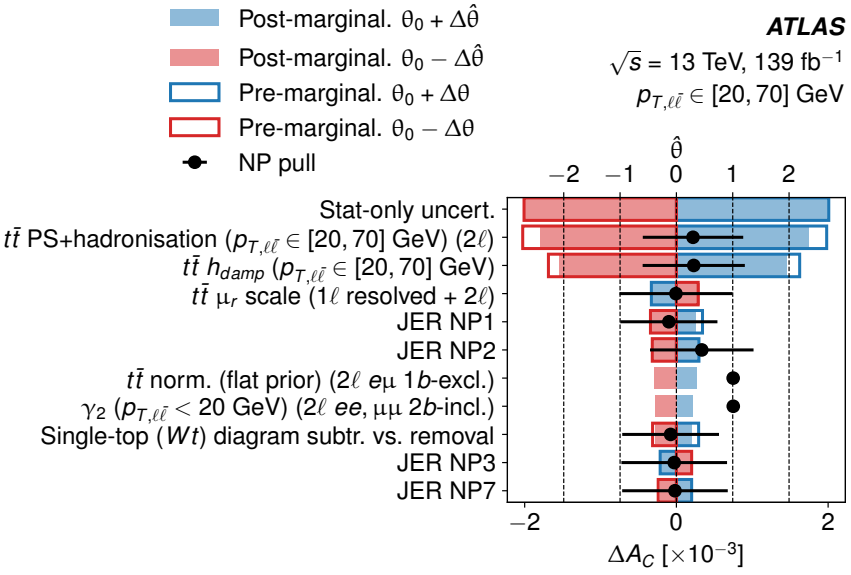

(a) $20 < p_{\mathrm{T},\ell\bar{\ell}} < 70$ GeV

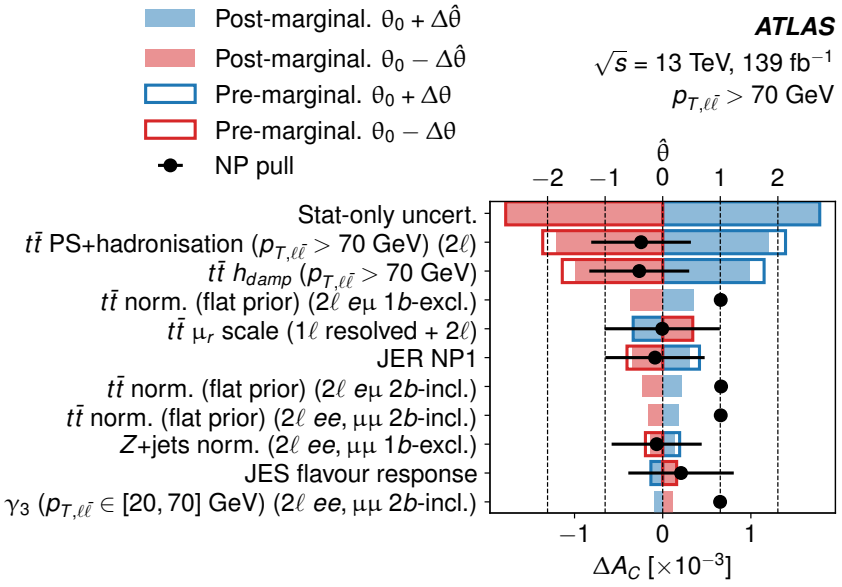

(b) $p_{\mathrm{T},\ell\bar{\ell}} > 70$ GeV

Figure 22: Ranking of the systematic uncertainties with marginalisation (a) for $p_{\mathrm{T},\ell\bar{\ell}} \in [20, 70]$ GeV and (b) for $p_{\mathrm{T},\ell\bar{\ell}} > 70$ GeV. Only the ten highest-ranking uncertainties are shown, ordered according to their post-marginalisation ranking, which considers the constraining power of the marginalisation for the data. The red and blue bars show the effect on unfolded A_{C} of downward and upward variation of the systematic uncertainty, respectively. The points show the pulls and constraints of the ranked NPs obtained from data.

References

[1] ATLAS Collaboration, *Measurement of the $t\bar{t}$ production cross-section and lepton differential distributions in $e\mu$ dilepton events from pp collisions at $\sqrt{s} = 13$ TeV with the ATLAS detector*, Eur. Phys. J. C **80** (2020) 528, arXiv: 1910.08819 [hep-ex].

[2] CMS Collaboration, *Measurement of differential $t\bar{t}$ production cross sections in the full kinematic range using lepton+jets events from proton–proton collisions at $\sqrt{s} = 13$ TeV*, Phys. Rev. D **104** (2021) 092013, arXiv: 2108.02803 [hep-ex].

[3] Particle Data Group, *Review of Particle Physics*, PTEP **2020** (2020) 083C01.

[4] O. Antuñano, J. H. Kühn and G. Rodrigo, *Top quarks, axigluons, and charge asymmetries at hadron colliders*, Phys. Rev. D **77** (2008) 014003, arXiv: 0709.1652 [hep-ph].

[5] J. L. Rosner, *Prominent decay modes of a leptophobic Z'*, Phys. Lett. B **387** (1996) 113, arXiv: hep-ph/9607207 [hep-ph].

[6] P. Ferrario and G. Rodrigo, *Massive color-octet bosons and the charge asymmetries of top quarks at hadron colliders*, Phys. Rev. D **78** (2008) 094018, arXiv: 0809.3354 [hep-ph].

[7] J. H. Kühn and G. Rodrigo, *Charge asymmetry of heavy quarks at hadron colliders*, Phys. Rev. D **59** (1999) 054017, arXiv: hep-ph/9807420.

[8] J. H. Kühn and G. Rodrigo, *Charge asymmetries of top quarks at hadron colliders revisited*, JHEP **01** (2012) 063, arXiv: 1109.6830 [hep-ph].

[9] J. A. Aguilar-Saavedra, D. Amidei, A. Juste and M. Pérez-Victoria, *Asymmetries in top quark pair production at hadron colliders*, Rev. Mod. Phys. **87** (2015) 421, arXiv: 1406.1798 [hep-ph].

[10] M. Czakon, P. Fiedler and A. Mitov, *Resolving the Tevatron Top Quark Forward-Backward Asymmetry Puzzle: Fully Differential Next-to-Next-to-Leading-Order Calculation*, Phys. Rev. Lett. **115** (2015) 052001, arXiv: 1411.3007 [hep-ph].

[11] CDF Collaboration, *Forward-Backward Asymmetry in Top Quark Production in $p\bar{p}$ Collisions at $\sqrt{s} = 1.96$ TeV*, Phys. Rev. Lett. **101** (2008) 202001, arXiv: 0806.2472 [hep-ex].

[12] D0 Collaboration, *Measurement of the Forward-Backward Charge Asymmetry in Top-Quark Pair Production*, Phys. Rev. Lett. **100** (2008) 142002, arXiv: 0712.0851 [hep-ex].

[13] CDF Collaboration, *Evidence for a mass dependent forward-backward asymmetry in top quark pair production*, Phys. Rev. D **83** (2011) 112003, arXiv: 1101.0034 [hep-ex].

[14] D0 Collaboration, *Simultaneous measurement of forward-backward asymmetry and top polarization in dilepton final states from $t\bar{t}$ production at the Tevatron*, Phys. Rev. D **92** (2015) 052007, arXiv: 1507.05666 [hep-ex].

[15] CDF Collaboration, *Measurement of the top quark forward-backward production asymmetry and its dependence on event kinematic properties*, Phys. Rev. D **87** (2013) 092002, arXiv: 1211.1003 [hep-ex].

[16] D0 Collaboration, *Measurement of the forward-backward asymmetry in top quark-antiquark production in $p\bar{p}$ collisions using the lepton+jets channel*, Phys. Rev. D **90** (2014) 072011, arXiv: 1405.0421 [hep-ex].

[17] S. Jung, A. Pierce and J. D. Wells, *Top quark asymmetry from a non-Abelian horizontal symmetry*, Phys. Rev. D **83** (2011) 114039, arXiv: 1103.4835 [hep-ph].

[18] R. Diener, S. Godfrey and T. A. W. Martin, *Using final state pseudorapidities to improve s-channel resonance observables at the LHC*, Phys. Rev. D **80** (2009) 075014, arXiv: 0909.2022 [hep-ph].

[19] M. Czakon et al., *Top-quark charge asymmetry at the LHC and Tevatron through NNLO QCD and NLO EW*, Phys. Rev. D **98** (2018) 014003, arXiv: 1711.03945 [hep-ph], We thank A. Mitov and R. Poncelet for preparing numerical results for the inclusive and differential $A_{\mathrm{C}}^{t\bar{t}}$ measurements using our binning. The detailed results are publicly available on https://www.precision.hep.phy.cam.ac.uk/results/ttbar-nnloqcd-nloew/.

[20] W. Bernreuther and Z.-G. Si, *Top quark and leptonic charge asymmetries for the Tevatron and LHC*, Phys. Rev. D **86** (2012) 034026, arXiv: 1205.6580 [hep-ph], We thank W. Bernreuther and Z.-G. Si for providing the Standard Model prediction for the leptonic asymmetry for pp collisions at the LHC with $\sqrt{s} = 13$ TeV, using our reduced phase-space.

[21] A. Djouadi, G. Moreau, F. Richard and R. K. Singh, *Forward-backward asymmetry of top quark production at the Tevatron in warped extra dimensional models*, Phys. Rev. D **82** (2010) 071702, arXiv: 0906.0604 [hep-ph].

[22] S. Jung, H. Murayama, A. Pierce and J. D. Wells, *Top quark forward-backward asymmetry from new t-channel physics*, Phys. Rev. D **81** (2010) 015004, arXiv: 0907.4112 [hep-ph].

[23] P. H. Frampton, J. Shu and K. Wang, *Axigluon as possible explanation for $p\bar{p} \to t\bar{t}$ forward–backward asymmetry*, Phys. Lett. B **683** (2010) 294, arXiv: 0911.2955 [hep-ph].

[24] P. Ferrario and G. Rodrigo, *Constraining heavy colored resonances from top-antitop quark events*, Phys. Rev. D **80** (2009) 051701, arXiv: 0906.5541 [hep-ph].

[25] B. Grinstein, A. L. Kagan, M. Trott and J. Zupan, *Forward-Backward Asymmetry in $t\bar{t}$ Production from Flavor Symmetries*, Phys. Rev. Lett. **107** (2011) 012002, arXiv: 1102.3374 [hep-ph].

[26] J. A. Aguilar-Saavedra and M. Pérez-Victoria, *Asymmetries in $t\,\bar{t}$ production: LHC versus Tevatron*, Phys. Rev. D **84** (2011) 115013, arXiv: 1105.4606 [hep-ph].

[27] Z. Ligeti, G. Marques Tavares and M. Schmaltz, *Explaining the $t\bar{t}$ forward-backward asymmetry without dijet or flavor anomalies*, JHEP **06** (2011) 109, arXiv: 1103.2757 [hep-ph].

[28] J. A. Aguilar-Saavedra and M. Pérez-Victoria, *Probing the Tevatron $t\bar{t}$ asymmetry at LHC*, JHEP **05** (2011) 034, arXiv: 1103.2765 [hep-ph].

[29] J. A. Aguilar-Saavedra, A. Juste and F. Rubbo, *Boosting the $t\bar{t}$ charge asymmetry*, Phys. Lett. B **707** (2012) 92, arXiv: 1109.3710 [hep-ph].

[30] ATLAS Collaboration, *Measurement of the top quark pair production charge asymmetry in proton–proton collisions at $\sqrt{s}$ = 7 TeV using the ATLAS detector*, JHEP **02** (2014) 107, arXiv: 1311.6724 [hep-ex].

[31] ATLAS Collaboration, *Measurement of the charge asymmetry in top-quark pair production in the lepton-plus-jets final state in pp collision data at $\sqrt{s}$ = 8 TeV with the ATLAS detector*, Eur. Phys. J. C **76** (2016) 87, arXiv: 1509.02358 [hep-ex], Erratum: Eur. Phys. J. C **77** (2017) 564.

[32] CMS Collaboration, *Inclusive and differential measurements of the $t\bar{t}$ charge asymmetry in proton–proton collisions at $\sqrt{s}$ = 7 TeV*, Phys. Lett. B **717** (2012) 129, arXiv: 1207.0065 [hep-ex].

[33] CMS Collaboration, *Inclusive and differential measurements of the $t\bar{t}$ charge asymmetry in pp collisions at $\sqrt{s}$ = 8 TeV*, Phys. Lett. B **757** (2016) 154, arXiv: 1507.03119 [hep-ex].

[34] ATLAS Collaboration, *Measurement of the charge asymmetry in dileptonic decays of top quark pairs in pp collisions at $\sqrt{s}$ = 7 TeV using the ATLAS detector*, JHEP **05** (2015) 061, arXiv: 1501.07383 [hep-ex].

[35] ATLAS Collaboration, *Measurements of the charge asymmetry in top-quark pair production in the dilepton final state at $\sqrt{s}$ = 8 TeV with the ATLAS detector*, Phys. Rev. D **94** (2016) 032006, arXiv: 1604.05538 [hep-ex].

[36] CMS Collaboration, *Measurements of the $t\bar{t}$ charge asymmetry using the dilepton decay channel in pp collisions at $\sqrt{s}$ = 7 TeV*, JHEP **04** (2014) 191, arXiv: 1402.3803 [hep-ex].

[37] CMS Collaboration, *Measurements of $t\bar{t}$ charge asymmetry using dilepton final states in pp collisions at $\sqrt{s}$ = 8 TeV*, Phys. Lett. B **760** (2016) 365, arXiv: 1603.06221 [hep-ex].

[38] ATLAS Collaboration, *Measurement of the charge asymmetry in highly boosted top-quark pair production in $\sqrt{s}$ = 8 TeV pp collision data collected by the ATLAS experiment*, Phys. Lett. B **756** (2016) 52, arXiv: 1512.06092 [hep-ex].

[39] CMS Collaboration, *Measurement of the charge asymmetry in top quark pair production in pp collisions at $\sqrt{s}$ = 8 TeV using a template method*, Phys. Rev. D **93** (2016) 034014, arXiv: 1508.03862 [hep-ex].

[40] CMS Collaboration, *Measurements of $t\bar{t}$ differential cross sections in proton–proton collisions at $\sqrt{s}$ = 13 TeV using events containing two leptons*, JHEP **02** (2019) 149, arXiv: 1811.06625 [hep-ex].

[41] ATLAS and CMS Collaborations, *Combination of inclusive and differential $t\bar{t}$ charge asymmetry measurements using ATLAS and CMS data at $\sqrt{s}$ = 7 and 8 TeV*, JHEP **04** (2018) 033, arXiv: 1709.05327 [hep-ex].

[42] G.Choudalakis, *Fully Bayesian Unfolding*, (2012), arXiv: 1201.4612 [hep-ex].

[43] W. Buchmüller and D. Wyler, *Effective lagrangian analysis of new interactions and flavour conservation*, Nucl. Phys. B **268** (1986) 621.

[44] B. Grzadkowski, M. Iskrzyński, M. Misiak and J. Rosiek, *Dimension-six terms in the Standard Model Lagrangian*, JHEP **10** (2010) 085, arXiv: 1008.4884 [hep-ph].

[45] D. Barducci et al.,
Interpreting top-quark LHC measurements in the standard-model effective field theory,
(2018), ed. by J. A. Aguilar-Saavedra et al., arXiv: 1802.07237 [hep-ph].

[46] ATLAS Collaboration, *Measurement of the energy asymmetry in $t\bar{t}j$ production at 13 TeV with the ATLAS experiment and interpretation in the SMEFT framework*, Eur. Phys. J. C **82** (2022) 374, arXiv: 2110.05453 [hep-ex].

[47] ATLAS Collaboration, *The ATLAS Experiment at the CERN Large Hadron Collider*, JINST **3** (2008) S08003.

[48] ATLAS Collaboration, *ATLAS Insertable B-Layer: Technical Design Report*, ATLAS-TDR-19; CERN-LHCC-2010-013, 2010, URL: https://cds.cern.ch/record/1291633, Addendum: ATLAS-TDR-19-ADD-1; CERN-LHCC-2012-009, 2012, URL: https://cds.cern.ch/record/1451888.

[49] B. Abbott et al., *Production and integration of the ATLAS Insertable B-Layer*, JINST **13** (2018) T05008, arXiv: 1803.00844 [physics.ins-det].

[50] ATLAS Collaboration, *Performance of the ATLAS trigger system in 2015*, Eur. Phys. J. C **77** (2017) 317, arXiv: 1611.09661 [hep-ex].

[51] ATLAS Collaboration, *The ATLAS Collaboration Software and Firmware*, ATL-SOFT-PUB-2021-001, 2021, URL: https://cds.cern.ch/record/2767187.

[52] ATLAS Collaboration, *Vertex Reconstruction Performance of the ATLAS Detector at $\sqrt{s} = 13$ TeV*, ATL-PHYS-PUB-2015-026, 2015, URL: https://cds.cern.ch/record/2037717.

[53] ATLAS Collaboration, *Electron and photon performance measurements with the ATLAS detector using the 2015–2017 LHC proton–proton collision data*, JINST **14** (2019) P12006, arXiv: 1908.00005 [hep-ex].

[54] ATLAS Collaboration, *Electron reconstruction and identification in the ATLAS experiment using the 2015 and 2016 LHC proton–proton collision data at $\sqrt{s} = 13$ TeV*, Eur. Phys. J. C **79** (2019) 639, arXiv: 1902.04655 [hep-ex].

[55] ATLAS Collaboration, *Muon reconstruction and identification efficiency in ATLAS using the full Run 2 pp collision data set at $\sqrt{s} = 13$ TeV*, Eur. Phys. J. C **81** (2021) 578, arXiv: 2012.00578 [hep-ex].

[56] ATLAS Collaboration,
Topological cell clustering in the ATLAS calorimeters and its performance in LHC Run 1, Eur. Phys. J. C **77** (2017) 490, arXiv: 1603.02934 [hep-ex].

[57] M. Cacciari, G. P. Salam and G. Soyez, *The anti-k(t) jet clustering algorithm*, JHEP **04** (2008) 063, arXiv: 0802.1189 [hep-ph].

[58] M. Cacciari, G. P. Salam and G. Soyez, *FastJet user manual*, Eur. Phys. J. C **72** (2012) 1896, arXiv: 1111.6097 [hep-ph].

[59] M. Cacciari, G. P. Salam and G. Soyez, *The catchment area of jets*, JHEP **04** (2008) 005, arXiv: 0802.1188 [hep-ph].

[60] ATLAS Collaboration, *Jet energy scale measurements and their systematic uncertainties in proton–proton collisions at $\sqrt{s} = 13$ TeV with the ATLAS detector*, Phys. Rev. D **96** (2017) 072002, arXiv: 1703.09665 [hep-ex].

[61] ATLAS Collaboration, *Performance of pile-up mitigation techniques for jets in pp collisions at $\sqrt{s} = 8$ TeV using the ATLAS detector*, Eur. Phys. J. C **76** (2016) 581, arXiv: 1510.03823 [hep-ex].

[62] ATLAS Collaboration, *Measurements of b-jet tagging efficiency with the ATLAS detector using $t\bar{t}$ events at $\sqrt{s} = 13$ TeV*, JHEP **08** (2018) 089, arXiv: 1805.01845 [hep-ex].

[63] ATLAS Collaboration, *Jet energy measurement and its systematic uncertainty in proton–proton collisions at $\sqrt{s} = 7$ TeV with the ATLAS detector*, Eur. Phys. J. C **75** (2015) 17, arXiv: 1406.0076 [hep-ex].

[64] D. Krohn, J. Thaler and L.-T. Wang, *Jet trimming*, JHEP **02** (2010) 084, arXiv: 0912.1342 [hep-ph].

[65] S. D. Ellis and D. E. Soper, *Successive combination jet algorithm for hadron collisions*, Phys. Rev. D **48** (1993) 3160, arXiv: hep-ph/9305266 [hep-ph].

[66] ATLAS Collaboration, *Identification of boosted, hadronically decaying W bosons and comparisons with ATLAS data taken at $\sqrt{s} = 8$ TeV*, Eur. Phys. J. C **76** (2016) 154, arXiv: 1510.05821 [hep-ex].

[67] J. Thaler and K. Van Tilburg, *Identifying boosted objects with N-subjettiness*, JHEP **03** (2011) 015, arXiv: 1011.2268 [hep-ph].

[68] ATLAS Collaboration, *Performance of missing transverse momentum reconstruction with the ATLAS detector using proton–proton collisions at $\sqrt{s} = 13$ TeV*, Eur. Phys. J. C **78** (2018) 903, arXiv: 1802.08168 [hep-ex].

[69] D. J. Lange, *The EvtGen particle decay simulation package*, Nucl. Instrum. Meth. A **462** (2001) 152.

[70] E. Bothmann et al., *Event generation with Sherpa 2.2*, SciPost Phys. **7** (2019) 34, arXiv: 1905.09127 [hep-ph].

[71] ATLAS Collaboration, *The ATLAS Simulation Infrastructure*, Eur. Phys. J. C **70** (2010) 823, arXiv: 1005.4568 [physics.ins-det].

[72] S. Agostinelli et al., *GEANT4 – a simulation toolkit*, Nucl. Instrum. Meth. A **506** (2003) 250.

[73] T. Sjöstrand et al., *An introduction to PYTHIA 8.2*, Comput. Phys. Commun. **191** (2015) 159, arXiv: 1410.3012 [hep-ph].

[74] A. D. Martin, W. J. Stirling, R. S. Thorne and G. Watt, *Parton distributions for the LHC*, Eur. Phys. J. C **63** (2009) 189, arXiv: 0901.0002 [hep-ph].

[75] ATLAS Collaboration, *The Pythia 8 A3 tune description of ATLAS minimum bias and inelastic measurements incorporating the Donnachie–Landshoff diffractive model*, ATL-PHYS-PUB-2016-017, 2016, URL: https://cds.cern.ch/record/2206965.

[76] M. Beneke, P. Falgari, S. Klein and C. Schwinn, *Hadronic top-quark pair production with NNLL threshold resummation*, Nucl. Phys. B **855** (2012) 695, arXiv: 1109.1536 [hep-ph].

[77] M. Cacciari, M. Czakon, M. Mangano, A. Mitov and P. Nason, *Top-pair production at hadron colliders with next-to-next-to-leading logarithmic soft-gluon resummation*, Phys. Lett. B **710** (2012) 612, arXiv: 1111.5869 [hep-ph].

[78] P. Bärnreuther, M. Czakon and A. Mitov, *Percent-Level-Precision Physics at the Tevatron: Next-to-Next-to-Leading Order QCD Corrections to $q\bar{q} \to t\bar{t} + X$*, Phys. Rev. Lett. **109** (2012) 132001, arXiv: 1204.5201 [hep-ph].

[79] M. Czakon and A. Mitov, *NNLO corrections to top-pair production at hadron colliders: the all-fermionic scattering channels*, JHEP **12** (2012) 054, arXiv: 1207.0236 [hep-ph].

[80] M. Czakon and A. Mitov, *NNLO corrections to top pair production at hadron colliders: the quark-gluon reaction*, JHEP **01** (2013) 080, arXiv: 1210.6832 [hep-ph].

[81] M. Czakon, P. Fiedler and A. Mitov, *Total Top-Quark Pair-Production Cross Section at Hadron Colliders Through $O(\alpha_S^4)$*, Phys. Rev. Lett. **110** (2013) 252004, arXiv: 1303.6254 [hep-ph].

[82] M. Czakon and A. Mitov, *Top++: A program for the calculation of the top-pair cross-section at hadron colliders*, Comput. Phys. Commun. **185** (2014) 2930, arXiv: 1112.5675 [hep-ph].

[83] M. Botje et al., *The PDF4LHC Working Group Interim Recommendations*, (2011), arXiv: 1101.0538 [hep-ph].

[84] A. D. Martin, W. J. Stirling, R. S. Thorne and G. Watt, *Uncertainties on α_S in global PDF analyses and implications for predicted hadronic cross sections*, Eur. Phys. J. C **64** (2009) 653, arXiv: 0905.3531 [hep-ph].

[85] H.-L. Lai et al., *New parton distributions for collider physics*, Phys. Rev. D **82** (2010) 074024, arXiv: 1007.2241 [hep-ph].

[86] J. Gao et al., *CT10 next-to-next-to-leading order global analysis of QCD*, Phys. Rev. D **89** (2014) 033009, arXiv: 1302.6246 [hep-ph].

[87] R. D. Ball et al., *Parton distributions with LHC data*, Nucl. Phys. B **867** (2013) 244, arXiv: 1207.1303 [hep-ph].

[88] S. Frixione, G. Ridolfi and P. Nason, *A positive-weight next-to-leading-order Monte Carlo for heavy flavour hadroproduction*, JHEP **09** (2007) 126, arXiv: 0707.3088 [hep-ph].

[89] P. Nason, *A new method for combining NLO QCD with shower Monte Carlo algorithms*, JHEP **11** (2004) 040, arXiv: hep-ph/0409146.

[90] S. Frixione, P. Nason and C. Oleari, *Matching NLO QCD computations with parton shower simulations: the POWHEG method*, JHEP **11** (2007) 070, arXiv: 0709.2092 [hep-ph].

[91] S. Alioli, P. Nason, C. Oleari and E. Re, *A general framework for implementing NLO calculations in shower Monte Carlo programs: the POWHEG BOX*, JHEP **06** (2010) 043, arXiv: 1002.2581 [hep-ph].

[92] E. Re, *Single-top Wt-channel production matched with parton showers using the POWHEG method*, Eur. Phys. J. C **71** (2011) 1547, arXiv: 1009.2450 [hep-ph].

[93] R. Frederix, E. Re and P. Torrielli, *Single-top t-channel hadroproduction in the four-flavour scheme with POWHEG and aMC@NLO*, JHEP **09** (2012) 130, arXiv: 1207.5391 [hep-ph].

[94] S. Alioli, P. Nason, C. Oleari and E. Re,
NLO single-top production matched with shower in POWHEG: s- and t-channel contributions,
JHEP **09** (2009) 111, arXiv: 0907.4076 [hep-ph], Erratum: JHEP **02** (2010) 011.

[95] R. D. Ball et al., *Parton distributions for the LHC run II*, JHEP **04** (2015) 040,
arXiv: 1410.8849 [hep-ph].

[96] ATLAS Collaboration, *Studies on top-quark Monte Carlo modelling for Top2016*,
ATL-PHYS-PUB-2016-020, 2016, URL: https://cds.cern.ch/record/2216168.

[97] ATLAS Collaboration, *ATLAS Pythia 8 tunes to 7 TeV data*, ATL-PHYS-PUB-2014-021, 2014,
URL: https://cds.cern.ch/record/1966419.

[98] M. Bähr et al., *Herwig++ physics and manual*, Eur. Phys. J. C **58** (2008) 639,
arXiv: 0803.0883 [hep-ph].

[99] J. Bellm et al., *Herwig 7.0/Herwig++ 3.0 release note*, Eur. Phys. J. C **76** (2016) 196,
arXiv: 1512.01178 [hep-ph].

[100] J. Bellm et al., *Herwig 7.1 Release Note*, (2017), arXiv: 1705.06919 [hep-ph].

[101] L. A. Harland-Lang, A. D. Martin, P. Motylinski and R. S. Thorne,
Parton distributions in the LHC era: MMHT 2014 PDFs, Eur. Phys. J. C **75** (2015) 204,
arXiv: 1412.3989 [hep-ph].

[102] J. A. Aguilar-Saavedra, *Single top quark production at LHC with anomalous Wtb couplings*,
Nucl. Phys. B **804** (2008) 160, arXiv: 0803.3810 [hep-ph].

[103] J. Pumplin et al.,
New generation of parton distributions with uncertainties from global QCD analysis,
JHEP **07** (2002) 012, arXiv: hep-ph/0201195.

[104] S. Frixione, E. Laenen, P. Motylinski, C. White and B. R. Webber,
Single-top hadroproduction in association with a W boson, JHEP **07** (2008) 029,
arXiv: 0805.3067 [hep-ph].

[105] J. M. Campbell, R. Frederix, F. Maltoni and F. Tramontano,
Next-to-Leading-Order Predictions for t-Channel Single-Top Production at Hadron Colliders,
Phys. Rev. Lett. **102** (2009) 182003, arXiv: 0903.0005 [hep-ph].

[106] T. Gleisberg and S. Höche, *Comix, a new matrix element generator*, JHEP **12** (2008) 039,
arXiv: 0808.3674 [hep-ph].

[107] F. Cascioli, P. Maierhofer and S. Pozzorini, *Scattering Amplitudes with Open Loops*,
Phys. Rev. Lett. **108** (2012) 111601, arXiv: 1111.5206 [hep-ph].

[108] A. Denner, S. Dittmaier and L. Hofer,
COLLIER: A fortran-based complex one-loop library in extended regularizations,
Comput. Phys. Commun. **212** (2017) 220, arXiv: 1604.06792 [hep-ph].

[109] S. Schumann and F. Krauss,
A Parton shower algorithm based on Catani-Seymour dipole factorisation, JHEP **03** (2008) 038,
arXiv: 0709.1027 [hep-ph].

[110] J.-C. Winter, F. Krauss and G. Soff, *A modified cluster-hadronisation model*,
Eur. Phys. J. C **36** (2004) 381, arXiv: hep-ph/0311085 [hep-ph].

[111] C. Anastasiou, L. Dixon, K. Melnikov and F. Petriello, *High-precision QCD at hadron colliders: Electroweak gauge boson rapidity distributions at next-to-next-to leading order*, Phys. Rev. D **69** (2004) 094008, arXiv: hep-ph/0312266.

[112] ATLAS Collaboration, *Estimation of non-prompt and fake lepton backgrounds in final states with top quarks produced in proton–proton collisions at* $\sqrt{s} = 8$ *TeV with the ATLAS Detector*, ATLAS-CONF-2014-058, 2014, URL: https://cds.cern.ch/record/1951336.

[113] S. Höche, F. Krauss, M. Schönherr and F. Siegert, *A critical appraisal of NLO+PS matching methods*, JHEP **09** (2012) 049, arXiv: 1111.1220 [hep-ph].

[114] S. Catani, F. Krauss, B. R. Webber and R. Kuhn, *QCD Matrix Elements + Parton Showers*, JHEP **11** (2001) 063, arXiv: hep-ph/0109231.

[115] S. Höche, F. Krauss, S. Schumann and F. Siegert, *QCD matrix elements and truncated showers*, JHEP **05** (2009) 053, arXiv: 0903.1219 [hep-ph].

[116] S. Höche, F. Krauss, M. Schönherr and F. Siegert, *QCD matrix elements + parton showers: The NLO case*, JHEP **04** (2013) 027, arXiv: 1207.5030 [hep-ph].

[117] J. Alwall et al., *The automated computation of tree-level and next-to-leading order differential cross sections, and their matching to parton shower simulations*, JHEP **07** (2014) 079, arXiv: 1405.0301 [hep-ph].

[118] ATLAS Collaboration, *ATLAS data quality operations and performance for 2015–2018 data-taking*, JINST **15** (2020) P04003, arXiv: 1911.04632 [physics.ins-det].

[119] ATLAS Collaboration, *Performance of electron and photon triggers in ATLAS during LHC Run 2*, Eur. Phys. J. C **80** (2020) 47, arXiv: 1909.00761 [hep-ex].

[120] ATLAS Collaboration, *Performance of the ATLAS muon triggers in Run 2*, JINST **15** (2020) P09015, arXiv: 2004.13447 [hep-ex].

[121] A. Hoecker et al., *TMVA - Toolkit for Multivariate Data Analysis*, (2007), URL: https://arxiv.org/abs/physics/0703039.

[122] J. Erdmann et al., *A likelihood-based reconstruction algorithm for top-quark pairs and the KLFitter framework*, Nucl. Instrum. Meth. A **748** (2014) 18, arXiv: 1312.5595 [hep-ex].

[123] ATLAS Collaboration, *Performance of Top Quark and W Boson Tagging in Run 2 with ATLAS*, ATLAS-CONF-2017-064, 2017, URL: https://cds.cern.ch/record/2281054.

[124] ATLAS Collaboration, *Measurements of differential cross-sections in top-quark pair events with a high transverse momentum top quark and limits on beyond the Standard Model contributions to top-quark pair production with the ATLAS detector at* $\sqrt{s} = 13$ *TeV*, JHEP **06** (2022) 063, arXiv: 2202.12134 [hep-ex].

[125] ATLAS Collaboration, *Differential* $t\bar{t}$ *cross-section measurements using boosted top quarks in the all-hadronic final state with* $139\,fb^{-1}$ *of ATLAS data*, (2022), arXiv: 2205.02817 [hep-ex].

[126] D0 Collaboration, *Precise measurement of the top quark mass in dilepton decays using optimized neutrino weighting*, Phys. Lett. B **752** (2016) 18, arXiv: 1508.03322 [hep-ex].

[127] M. D. Hoffman and A. Gelman,
The No-U-Turn Sampler: Adaptively Setting Path Lengths in Hamiltonian Monte Carlo,
Journal of Machine Learning Research **15** (2014) 1593,
URL: http://jmlr.org/papers/v15/hoffman14a.html.

[128] G. Bohm and G. Zech, *Introduction to Statistics and Data Analysis for Physicists; 2nd rev. ed.*
Hamburg: Verlag Deutsches Elektronen-Synchrotron, 2014, ISBN: 978-3-935702-88-1,
URL: http://bib-pubdb1.desy.de/record/169869.

[129] ATLAS Collaboration,
Luminosity determination in pp collisions at $\sqrt{s} = 13$ TeV using the ATLAS detector at the LHC,
ATLAS-CONF-2019-021, 2019, URL: https://cds.cern.ch/record/2677054.

[130] G. Avoni et al., *The new LUCID-2 detector for luminosity measurement and monitoring in ATLAS*,
JINST **13** (2018) P07017.

[131] ATLAS Collaboration, *Electron and photon energy calibration with the ATLAS detector using 2015–2016 LHC proton–proton collision data*, JINST **14** (2019) P03017,
arXiv: 1812.03848 [hep-ex].

[132] ATLAS Collaboration, *Jet energy scale and resolution measured in proton–proton collisions at $\sqrt{s} = 13$ TeV with the ATLAS detector*, Eur. Phys. J. C **81** (2020) 689,
arXiv: 2007.02645 [hep-ex].

[133] ATLAS Collaboration,
In-situ measurements of the ATLAS large-radius jet response in 13 TeV pp collisions,
ATLAS-CONF-2017-063, 2017, URL: https://cds.cern.ch/record/2275655.

[134] ATLAS Collaboration,
Study of top-quark pair modelling and uncertainties using ATLAS measurements at $\sqrt{s} = 13$ TeV,
ATL-PHYS-PUB-2020-023, 2020, URL: https://cds.cern.ch/record/2730443.

[135] J. Rojo, *PDF4LHC recommendations for Run II*, PoS **DIS2016** (2016) 018,
arXiv: 1606.08243 [hep-ph].

[136] ATLAS Collaboration, *Measurement of $W^{\pm}$ and Z-boson production cross sections in pp collisions at $\sqrt{s} = 13$ TeV with the ATLAS detector*, Phys. Lett. B **759** (2016) 601,
arXiv: 1603.09222 [hep-ex].

[137] ATLAS Collaboration, *ATLAS simulation of boson plus jets processes in Run 2*,
ATL-PHYS-PUB-2017-006, 2017, URL: https://cds.cern.ch/record/2261937.

[138] F. Krauss, *Matrix Elements and Parton Showers in Hadronic Interactions*, JHEP **08** (2002) 015,
arXiv: hep-ph/0205283.

[139] M. Aliev et al., *HATHOR: HAdronic Top and Heavy quarks crOss section calculatoR*,
Comput. Phys. Commun. **182** (2011) 1034, arXiv: 1007.1327 [hep-ph].

[140] P. Kant et al., *HatHor for single top-quark production: Updated predictions and uncertainty estimates for single top-quark production in hadronic collisions*,
Comput. Phys. Commun. **191** (2015) 74, arXiv: 1406.4403 [hep-ph].

[141] ATLAS Collaboration, *Multi-Boson Simulation for 13 TeV ATLAS Analyses*,
ATL-PHYS-PUB-2017-005, 2017, URL: https://cds.cern.ch/record/2261933.

[142] S. Frixione, V. Hirschi, D. Pagani, H.-S. Shao and M. Zaro,
Electroweak and QCD corrections to top-pair hadroproduction in association with heavy bosons,
JHEP **06** (2015) 184, arXiv: 1504.03446 [hep-ph].

[143] G. Cowan, K. Cranmer, E. Gross and O. Vitells,
Asymptotic formulae for likelihood-based tests of new physics, Eur. Phys. J. C **71** (2011) 1554, arXiv: 1007.1727 [physics.data-an], Erratum: Eur. Phys. J. C **73** (2013) 2501.

[144] R. J. Barlow and C. Beeston, *Fitting using finite Monte Carlo samples*, Comput. Phys. Commun. **77** (1993) 219.

[145] M. Czakon et al., *Top-pair production at the LHC through NNLO QCD and NLO EW*, JHEP **10** (2017) 186, arXiv: 1705.04105 [hep-ph].

[146] M. Czakon, D. Heymes and A. Mitov,
High-Precision Differential Predictions for Top-Quark Pairs at the LHC, Phys. Rev. Lett. **116** (2016) 082003, arXiv: 1511.00549 [hep-ph].

[147] M. Czakon, P. Fiedler, D. Heymes and A. Mitov,
NNLO QCD predictions for fully-differential top-quark pair production at the Tevatron, JHEP **05** (2016) 034, arXiv: 1601.05375 [hep-ph].

[148] A. V. Manohar, P. Nason, G. P. Salam and G. Zanderighi, *The photon content of the proton*, JHEP **12** (2017) 046, arXiv: 1708.01256 [hep-ph].

[149] A. Manohar, P. Nason, G. P. Salam and G. Zanderighi,
How Bright is the Proton? A Precise Determination of the Photon Parton Distribution Function, Phys. Rev. Lett. **117** (2016) 242002, arXiv: 1607.04266 [hep-ph].

[150] M. Czakon, D. Heymes and A. Mitov,
Dynamical scales for multi-TeV top-pair production at the LHC, JHEP **04** (2017) 071, arXiv: 1606.03350 [hep-ph].

[151] I. Brivio et al., *O new physics, where art thou? A global search in the top sector*, JHEP **02** (2020) 131, arXiv: 1910.03606 [hep-ph].

[152] M. Perelló Roselló and M. Vos,
Constraints on four-fermion interactions from the $t\bar{t}$ charge asymmetry at hadron colliders, Eur. Phys. J. C **76** (2016) 200, arXiv: 1512.07542 [hep-ex].

[153] C. Zhang and S. Willenbrock, *Effective-field-theory approach to top-quark production and decay*, Phys. Rev. D **83** (2011) 034006, arXiv: 1008.3869 [hep-ph].

[154] C. Degrande et al., *Automated one-loop computations in the standard model effective field theory*, Phys. Rev. D **103** (2021) 096024, arXiv: 2008.11743 [hep-ph].

[155] J. J. Ethier et al.,
Combined SMEFT interpretation of Higgs, diboson, and top quark data from the LHC, (2021), arXiv: 2105.00006 [hep-ph],
We thank E. Vryonidou and C. Zhang for providing us the NLO predictions in the SMEFT, and for the parameterisation of the dependence of the differential charge asymmetry measurement on the Wilson coefficients of the SMEFT that form the basis of the EFT interpretation.

[156] CDF and D0 Collaborations, *Combined Forward-Backward Asymmetry Measurements in Top-Antitop Quark Production at the Tevatron*, Phys. Rev. Lett. **120** (2018) 042001, arXiv: 1709.04894 [hep-ex].

[157] N. P. Hartland et al.,
A Monte Carlo global analysis of the Standard Model Effective Field Theory: the top quark sector, JHEP **04** (2019) 100, arXiv: 1901.05965 [hep-ph].

[158] J. Ellis, M. Madigan, K. Mimasu, V. Sanz and T. You,
Top, Higgs, diboson and electroweak fit to the Standard Model effective field theory,
JHEP **04** (2021) 279, arXiv: 2012.02779 [hep-ph].

[159] A. Basan, P. Berta, L. Masetti, E. Vryonidou and S. Westhoff,
Measuring the top energy asymmetry at the LHC: QCD and SMEFT interpretations,
JHEP **03** (2020) 184, arXiv: 2001.07225 [hep-ph].